

STELLINGEN

behorende bij het proefschrift

A variable energy positron beam facility with applications in materials science

1. De door Nielsen et al. vermelde waarde voor de diffusielengte van positronen in silicium is niet in overeenstemming met de waarde die afgeleid kan worden uit de diffusiecoëfficiënt en de levensduur van positronen in silicium waarnaar door de auteurs verwezen wordt.
B. Nielsen et al., Phys. Rev. B 40, 1434, (1989).
B. Nielsen et al., Phys. Rev. B 32, 2296, (1985).
2. De door Huomo et al. gebruikte methode ter bepaling van de bijdrage van epithermische positronen in metingen van de positroniumfractie is incorrect.
H. Huomo et al., Phys. Rev. B 35, 8252, (1987).
3. Bij de toepassing van de positron-levensduurtechniek voor de karakterisering van polymeren dient men de bijdrage van ortho-positronium niet te beschrijven met één of twee levensduren, zoals tot nu toe gebruikelijk is, maar met een continu spectrum van levensduren.
P. Kindl et al., in Proc. of the 8th Int. Conf. on Positron Annihilation, (World Scientific, Singapore), p.806.
4. Rajainmäki et al. hebben waargenomen dat de levensduur van positronen in defekten in met protonen bestraald nikkel daalt bij uitgloeien tussen 500 K en 550 K. Door hen wordt dit toegeschreven aan de reductie van vakatureklusters door interacties met dislokatering. Dit effect kan evenwel worden verklaard door aan te nemen dat bij deze temperaturen middelgrote vakatureklusters instabiel worden en dissociëren.
H. Rajainmäki et al., J. Phys. F 18, 1109, (1988).
A. van Veen, in Proc. Int. Conf. on Vacancies and Interstitials in Metals and Alloys, Mat. Science Forum, 15, 3, (1987).

5. De aanwezigheid van waterstof in palladium doet de oplosbaarheid van helium in dit metaal sterk toenemen.
6. Een kernreaktor met een thermische neutronenflux in de orde van $10^{13} \text{ s}^{-1} \cdot \text{cm}^{-2}$, zoals aanwezig bij het Interfacultair Reaktor Instituut te Delft, is bij uitstek geschikt voor het genereren van intense positronenbundels.
7. Op grond van de resultaten van het onderzoek door DiFranza et al. dat rokers significant vaker betrokken zijn bij auto-ongelukken en meer verkeersovertredingen begaan dan niet-rokers, verdient het aanbeveling om op de verpakking van rookwaren het opschrift te plaatsen: "dit artikel kan de rijvaardigheid beïnvloeden".
J.R. DiFranza et al., NY State J. of Medicine, 86, 464, (1986).
8. Binnen een cilindervormige zeepbel in evenwicht met zijn omgeving heerst een overdruk ten opzichte van de omgevingsdruk gegeven door $\Delta P = 2S/r$ met S de oppervlaktespanning en r de straal van de cilinder. Bij een overdruk die Vermeer berekend heeft zou een dergelijke zeepbel uiteengespat zijn.
B. Vermeer, NTvN B55, 169, (1989).
9. Een oorlogsbodem vormt een goede grond voor ontwapeningsonderhandelingen.

27 maart 1990

H. Schut

4.90165

3179710

TR diss 10.5

1801

op 25-10-91 → a few opt ren

**TR diss
1805**

**A VARIABLE ENERGY POSITRON BEAM
FACILITY WITH APPLICATIONS IN
MATERIALS SCIENCE**

**A VARIABLE ENERGY POSITRON BEAM
FACILITY WITH APPLICATIONS IN
MATERIALS SCIENCE**

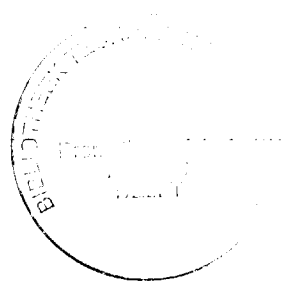
PROEFSCHRIFT

**TER VERKRIJGING VAN DE GRAAD VAN DOCTOR AAN DE
TECHNISCHE UNIVERSITEIT DELFT, OP GEZAG VAN DE
RECTOR MAGNIFICUS, PROF. DRS. P.A. SCHENCK,
IN HET OPENBAAR TE VERDEDIGEN TEN OVERSTAAN
VAN EEN COMMISSIE AANGEWEEZEN DOOR
HET COLLEGE VAN DEKANEN
OP 27 MAART 1990 TE 14.00 UUR**

door

HENDRIK SCHUT

geboren te Apeldoorn,
doctorandus in de natuurkunde



Dit proefschrift is goedgekeurd door de promotor
Prof. Dr. Ir. H. van Dam.

Dr. A. van Veen heeft als toegevoegd promotor in hoge mate
bijgedragen aan het totstandkomen van het proefschrift.

aan Carin
aan mijn ouders

Contents

1. INTRODUCTION.	9
1.1 General.	9
1.2 Positron annihilation in solids.	13
1.2.1 Annihilation of free positrons.	13
1.2.2 Positronium formation and annihilation.	17
2. DEPTH PROFILING WITH POSITRONS.	23
2.1 Introduction.	23
2.2 Interaction of positrons with solids and solid surfaces.	24
2.2.1 Introduction.	24
2.2.2 Epithermal positron effects.	28
2.2.3 Positron implantation profile.	29
2.2.4 Positron diffusion equation.	30
2.3 Modelling and fitting of positron beam experiments.	35
2.3.1 Introduction.	35
2.3.2 A fast method for numerical solution of the diffusion equation.	36
2.3.3 Application to F_{Ps} - and S-parameter measurements.	41
2.3.4 Fitting program.	44
2.3.5 Modelling and fitting results.	47
2.3.6 Discussion.	62
2.3.7 Conclusions.	63
3. THE VARIABLE ENERGY POSITRON BEAM FACILITY (VEP).	67
3.1 Introduction.	67
3.2 Description of the VEP.	69
3.2.1 General description.	69
3.2.2 Source storage and introduction.	73
3.2.3 Source and moderator area.	75
3.2.4 Beam transport and energy filter.	81
3.2.5 Accelerator stage.	83

3.2.6 Sample chamber.	83
3.2.7 Photon detection system.	87
3.2.8 Control and signal processing.	87
3.3 Beam performance.	90
3.3.1 Slow positron yield.	90
3.3.2 Energy resolution.	94
3.3.3 Beam oscillations.	96
4. POSITRON SURFACE BRANCHING.	103
4.1 Introduction.	103
4.2 Theoretical background.	104
4.3 Experimental.	108
4.4 Results and discussion.	109
4.5 Conclusion.	114
4.6 Appendix.	115
5. POSITRON BEAM STUDIES OF METALLIC LAYERED STRUCTURES AND SEMICONDUCTORS.	119
5.1 Introduction.	119
5.2 Ni-Ti-Ni layered structure.	121
5.3 Defect profiling of silicon MBE and SPE layers.	128
5.4 Helium implanted silicon.	136
5.5 Evaluation.	147
SUMMARY	152
SAMENVATTING	154
NAWOORD	156
CURRICULUM VITAE	157

Parts of this thesis have been published or will be submitted for publication.

- Chapter 2:

A. van Veen[†], J. de Vries[†], H. Schut[†], B. Nielsen[‡] and K.G. Lynn[‡],

Modelling and fitting of positron diffusion and trapping in positron beam experiments, to be published.

- Chapter 4:

H. Schut[†], A. van Veen[†], B. Nielsen[‡] and K.G. Lynn[‡],

Separation of bulk and surface effects in positron beam experiments on solids, to be published.

- Chapter 5, section 5.2:

H. Schut[†], A. van Veen[†], D.T. Britton[†], M.A. Hollanders[§] and B.J. Thyse[§],

Interdiffusion of Ti and Ni sputtered layers monitored by slow positron beam profiling techniques, in *Positron Annihilation*, Proc. of the 8th Int. Conf. on Positron Annihilation, eds. L. Dorikens-Vanpraet, M. Dorikens and D. Segers, (World Scientific, Singapore, 1989), p.428.

- Chapter 5, section 5.3:

H. Schut[†], A. van Veen[†], G.F.A. van de Walle[¶] and A.A. van Gorkum[¶], *Positron beam defect profiling of silicon epitaxial layers*, to be published.

[†]Interfaculty Reactor Institute, Delft University of Technology, Mekelweg 15, 2629 JB, Delft, the Netherlands.

[‡]Brookhaven National Laboratories, Upton, Long Island, NY, 11973, U.S.A.

[§]Laboratory of Metallurgy, Delft University of Technology, Rotterdamseweg 137, 2628 AL, Delft, the Netherlands.

[¶]Philips Research Laboratories, P.O. Box 80000, 5600 JA, Eindhoven, the Netherlands.

Chapter 1

Introduction

1.1 General

The field of solid state investigations with positrons started in the early fifties when it was recognized that information could be obtained about the properties of solids by studying the characteristics of the annihilation gamma rays arising from the mutual annihilation of a positron and an electron^{1,2,3}. In particular the discovery in the sixties of the interaction of positrons with defects⁴ in crystalline solids has given a strong impetus to a further elaboration of the positron annihilation technique. Today this technique has become established as a useful tool in materials science and is successfully applied for the investigation of defect structures present in metals, alloys and technologically relevant materials. Recently the positron annihilation technique has made its entry in the field of semiconductor technology.

The positron annihilation technique has its origin in conventional positron annihilation studies in which positrons emitted by a radioactive isotope are injected into a material. The energy of these positrons is distributed according to an energy distribution with end-point energies ranging from 0.5 MeV to several MeV depending on the isotope used. This broad energy distribution forms a drawback on the use of these positrons as probing particles because of the impossibility to obtain depth resolved information. Moreover, due to the relatively high energy of the positrons only the bulk of the material is probed. This was already realized in 1950 by Madanski and Rasetti⁵ who made the first

attempt to convert the initial positron energy distribution into a narrower one at lower energy. They irradiated various solids with positrons from a ^{64}Cu source, expecting to obtain a source of more or less monoenergetic positrons. Although their results turned out to be negative, all contemporary positron beams are based on the idea of moderating fast positrons to lower energies. Starting with the first successful positron beam built by Cherry⁶ in 1958, the conscious search for efficient moderator materials and methods to produce strong primary sources has led to a new branch in the positron annihilation technique: that of positron annihilation studies with variable energy positron beams.

In order to generate a beam of positrons one has to start with a primary positron source. Most often this is a positron emitting isotope, e.g. ^{22}Na , ^{58}Co or ^{64}Cu . The two first mentioned isotopes are the longer lived, with half-lives of 2.6 years and 71 days respectively, and can be purchased from commercial vendors. ^{64}Cu has a half-life of 12.8 hours and is therefore only applicable in combination with a nuclear reactor in which ^{64}Cu is produced by neutron irradiation of ^{63}Cu ⁷. A ^{64}Cu source embedded in ^{63}Cu has revealed to act as its own moderator. This enables the creation of intense continuous positron beams based on the 'on line' production of ^{64}Cu . Another method to generate strong primary positron sources is by pair production. In this case a pulsed electron beam emerging from a linear electron accelerator^{8,9} (LINAC) is stopped in a high-Z absorber, and from the resulting Bremsstrahlung electron-positron pairs are created. The pulsed electron beam automatically results in a pulsed positron beam. Pulsed positron beams can be applied to positron timing experiments, e.g. positron lifetime and Time of Flight (TOF) experiments¹⁰.

All sources mentioned above emit positrons with a continuous energy distribution and therefore moderation is required. At present most positron beams rely on the use of negative positron work function metallic moderators. Negative work function moderators re-emit positrons with energies of the order of a few eV and with small energy spread, basically caused by the thermal energy of the positrons in the moderator. Commonly used negative work function moderators are W(110)¹¹ and Ni(100)¹² single crystals or W(100)¹³ and Ni(100)¹⁴ thin moderator foils. The efficiencies quoted for these moderators range from 10^{-4} to 10^{-3} , depending on the source-moderator configuration used. Recent

research has led to the development of the so-called solid rare-gas moderators. These are based on the inability of positrons to slow down further to thermal energies in rare-gas solids when their energy has become less than the band-gap energy, thereby reducing the effect of positron trapping. The highest efficiency so far obtained is 5×10^{-3} using solid neon deposited on a ^{22}Na source¹⁵.

The concept of increasing the moderation efficiency by electrically drifting positrons across an insulating or semiconducting material has regained new interest with the development of field assisted moderators¹⁶. Calculations show that efficiencies up to 10% might be achieved. Field assisted moderators look very promising, particularly when applied to produce remoderated brightness enhanced positron beams. However, as yet no practical moderator has been realized.

The development of intense positron beams with variable energy has resulted in various new applications. Whereas conventional positron annihilation studies only yield information concerning the bulk of the material¹⁷, variable energy positron beams offer the possibility to study the properties of the surface and the near surface region up to a depth of several microns. The fastest growing area of research with positron beams is that of defect profiling in the sub-surface region of materials. The capability of variable energy positrons to probe the spatial distribution of defects underneath the surface was demonstrated by Triftshäuser and Kögel¹⁸ who studied the damage created in Ni single crystals irradiated with energetic He-ions. The investigation of defects associated with layered structures, e.g. overlayers, multilayers and interfaces, is the most recent application in this field.

Examples of recently developed positron surface techniques are Low Energy Positron Diffraction¹⁹ (LEPD), Positron induced Auger Electron Spectroscopy²⁰ (PAES) and 2-Dimensional Angular Correlation Angular Resolved²¹ (2D-ACAR) applied to surfaces. The successful realization of positron microbeams²² has been of major importance for this field of interest. Moreover, in the future microbeams will enable the investigation of the surface region by positron re-emission- and scanning microscopy²³. A review on experimentation with variable energy positron beams is given by Schultz and Lynn²⁴.

In this thesis we present the design and the performance of the Delft Variable Energy Positron beam (VEP), built at the Interfaculty

Reactor Institute. The VEP project was initiated in 1983 by the Radiation Damage Group of the Reactor Physics department. At that time the main activities of the group were focussed on the study of defects in metals and semiconductors, utilizing experimental techniques such as Thermal Helium Desorption Spectrometry (THDS), Scanning- and Transmission Electron Microscopy (SEM, TEM) and conventional positron annihilation (PA).

The contents of this thesis is organized as follows. In the present chapter the principles of the positron annihilation technique will be given. In chapter 2 the theory describing the interaction of positrons with condensed matter is presented. It deals with the implantation, slowing down, diffusion and trapping of positrons in solids. In addition some remarks will be made about the interaction of positrons with surfaces. In chapter 3 a detailed description of the design and the performance of the VEP equipment is presented. The experiments concerning the determination of the positron surface branching ratio are described in chapter 4. These experiments have been performed using the variable energy positron beam at the Brookhaven National Laboratories (USA), in cooperation with the Brookhaven positron beam group. In chapter 5 an example of a measurement on a layered structure is presented. It concerns a structure consisting of alternately stacked Ni and Ti layers deposited on a Si substrate. Also in this chapter the positron beam experiments performed on semiconducting materials are presented. Samples of interest in semiconductor technology are obtained from the Philips Research Laboratories. Measurements are carried out on Si epitaxial layers grown by Molecular Beam Epitaxy (MBE) and Solid Phase Epitaxy (SPE) techniques. Finally, an example of positron beam defect profiling on silicon irradiated with 30 keV helium ions will be discussed.

1.2 Positron annihilation in solids

1.2.1 Annihilation of free positrons

The transformation of a positron and its antiparticle the electron into photons is called annihilation. There are several ways in which a positron and an electron may annihilate. They are referred to by the number of photons involved, viz. non-photon, one-photon, two-photon and three-photon annihilation. The two first annihilation modes are very rare, and are of little interest with respect to positron annihilation studies.

In dense materials the annihilation of a positron and an electron predominantly takes place via the emission of two photons

$$e^+ + e^- \longrightarrow 2\gamma. \quad (1.1)$$

At low positron and electron energies the cross-section for two-photon annihilation is given by

$$\sigma_{2\gamma} = \frac{\pi r_0^2 c}{v}, \quad (1.2)$$

where r_0 is the classical electron radius, v the velocity of the positron, and c the velocity of light. The cross-section for three-photon annihilation is reduced by a factor of the order of the fine-structure constant α ($= 1/137$). Neglecting electron-electron interactions one obtains from eq. (1.2) the positron annihilation rate²⁵, λ ,

$$\lambda = \sigma_{2\gamma} n_e v \gamma(n) = \pi r_0^2 c n_e \gamma(n), \quad (1.3)$$

where n_e is the electron density and $\gamma(n)$ a so-called enhancement factor which accounts for electron-positron correlations.

In case of a positron-electron pair at rest at the moment of annihilation conservation of energy and momentum requires that the two photons are emitted in exact opposite directions and with an energy of $m_0 c^2 = 511$ keV each, where m_0 is the electron rest mass. If the annihilation pair has a momentum \vec{p} relative to the laboratory frame, the two photons are emitted at an angle slightly deviating from exact collinearity and with energies shifted from 511 keV. As illustrated in Fig. 1.1, to first order the deviation, Θ , from 180° is given by

$$\Theta = \frac{p_\perp}{m_0 c} \quad (1.4)$$

with p_t the momentum component in the plane perpendicular to the direction of photon emission. The energy shift, ΔE , from 511 keV is expressed by

$$\Delta E = \frac{cp_l}{2} \quad (1.5)$$

with p_l the longitudinal component of the momentum of the positron-electron pair.

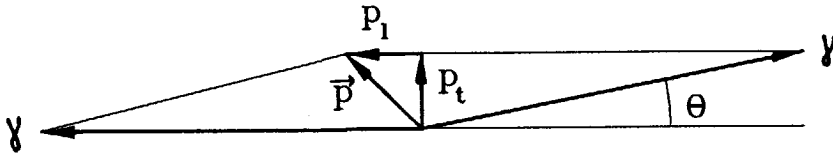


Fig. 1.1. The vector diagram of the momentum conservation in the two-photon annihilation process. The momentum of the positron-electron pair is denoted by \vec{p} . The subscripts l and t refer to the longitudinal and the transverse components, respectively. Θ is the deviation from exact collinearity.

A typical value of the momentum of electrons in metals calculated on basis of the free electron model is $1.5 \times 10^{-24} \text{ kg.m.s}^{-1}$. This corresponds to a maximum energy shift of 1.4 keV which can be detected with a high resolution solid state detector. The corresponding maximum angular deviation is 5.6 mrad and can easily be detected with modern angular correlation systems with resolutions better than 0.3 mrad²⁶. In angular correlation experiments the deviation from exact collinearity is measured. In Doppler broadening experiments the energy shift of the emitted annihilation radiation is measured. Usually, the positrons are thermalized before annihilation and therefore the contribution of the positron to the total momentum of the positron-electron pair can be neglected. Hence, these two techniques yield complementary information about the electron momentum distribution in solids. The annihilation rate is proportional to the electron density and is the inverse of the positron lifetime. Therefore, by measuring the positron lifetime information is obtained about the local electron density.

The Doppler broadening and the lifetime techniques, and to a lesser extent the angular correlation techniques, have proven to form a useful set of tools in defect spectroscopy. This is a direct consequence of the positron's affinity to open-volume defects, which create an attractive positron potential in the lattice of the host material. Being trapped in a defect, the positron experiences an electron density and an electron momentum distribution which differ from those seen by a free or delocalized Bloch-like positron.

The effect of positron trapping on the observables described above can be understood in terms of the overlap of the positron wave function with the conduction and core electrons in the solid. In vacancy type defects the average electron density is lower than in the bulk of the material, due to the relative absence of core electrons. As a consequence, a positron trapped in a defect has a higher probability to annihilate with a less energetic conduction electron. This results in a narrowing of the annihilation peak and a narrowing of the distribution describing the angular correlation curve. In addition, the lower electron density gives rise to a measurable increase of the positron lifetime, the latter being dependent on the size of the defect. Calculations of the positron lifetime as a function of the size of vacancy clusters in Mo and Al show that for large voids the positron lifetime increases from 200 to 500 ps²⁷.

The angular correlation technique is widely used to investigate the electron momentum distribution of metals and alloys. It can provide two-dimensional information (2D-ACAR), whereas Doppler broadening yields only the electron momentum in one dimension. In conventional positron annihilation the lifetime technique is successfully applied in defect spectroscopy because of its ability to detect the different positron trapping sites.

A commonly used parameter describing the width of the Doppler broadened 511 keV annihilation peak is the S-parameter, introduced by McKenzie²⁸. This parameter is defined as the ratio of the area, A , of a fixed central part of the peak and the total area, B , of the peak, as illustrated in Fig. 1.2. The positions of the boundaries defining the two integration intervals are chosen in such a way that the S-parameter becomes as sensitive as possible. The absolute value of this parameter carries no direct physical information. It depends for instance on the resolution of the photon detection system. However, it

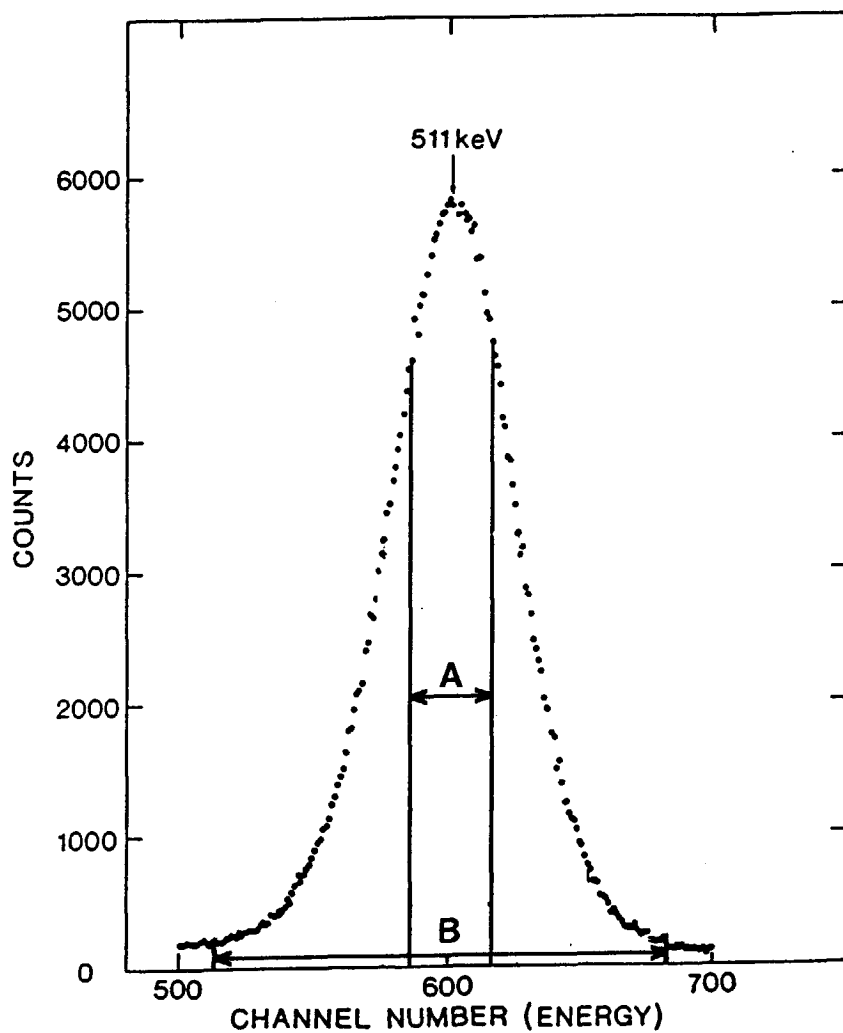


Fig. 1.2. Energy spectrum of the 511 keV annihilation radiation for the two-photon decay of a positron-electron pair. The broadening of the line is described by the lineshape parameter $S = A/B$, where A is the area of the central part of the peak and B is the total area of the peak.

is a useful parameter for monitoring the presence of defects. Compared to angular correlation, the Doppler broadening technique has a lower resolution, basically limited by the resolution of the detector. A typical energy resolution of 1.5 keV corresponds to an angular resolution of 6 mrad, which is an order of magnitude worse than the resolution of angular correlation systems. On the other hand, the efficiency of a Doppler broadening system is roughly two orders of magnitude larger, which makes the technique considerably faster and therewith useful for positron beam studies.

1.2.2 Positronium formation and annihilation

Besides taking part in one of the annihilation processes mentioned above, the interaction between a positron and an electron can also result in the formation of a hydrogen like bound state. This state is called positronium (Ps) and is known to exist in two ground states; para-positronium (p-Ps), a singlet 1S_0 state, and orthopositronium (o-Ps), a triplet 3S_1 state. In vacuum p-Ps has a lifetime of 125 ps, comparable with the lifetime of free positrons in metals. It decays predominantly via the emission of two 511 keV photons. The vacuum lifetime of o-Ps is 142 ns and it decays mainly into three photons with a continuous energy distribution ranging from 0 to 511 keV. In most materials with a high electron density, e.g. metals and semiconductors, the formation of Ps is not possible because of the size of the positronium atom which is twice that of the hydrogen atom. In molecular and ionic solids a quasi-positronium state exists. The lifetime of o-Ps in these materials is reduced to a few nanoseconds because of 'pick off' reactions, in which the parallel spin electron is exchanged by an electron with anti-parallel spin. In the angular correlation curve and the Doppler broadened annihilation peak the annihilation of p-Ps is observed as an additional narrow component, because of the low intrinsic momentum of the Ps atom.

With respect to positron beam studies, the formation of Ps at surfaces offers the possibility to study the diffusion process by which positrons can reach the surface of entrance after implantation into the material. In particular, by measuring the Ps-fraction (i.e. the relative amount of positronium formed) as a function of the positron incident

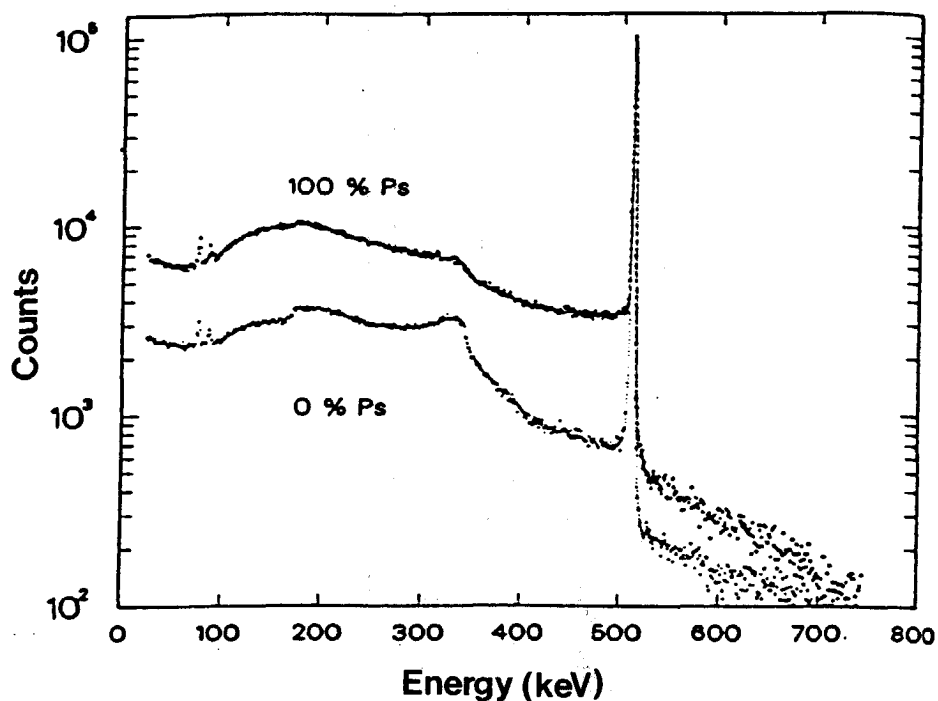


Fig. 1.3. Energy spectra of the annihilation radiation observed with a Ge solid state detector. The upper spectrum corresponds to a situation of 100% positronium formation. The lower spectrum corresponds to a situation of 0% positronium formation. The spectra are normalized to equal heights at the 511 keV photo-peak.¹¹

energy, and by applying a model describing the trapping of positrons in defects, information can be obtained about the spatial distribution of defects in the depth interval covered by the implanted positrons. Passing the sample-vacuum surface a positron may pick up an electron and leave the surface as a Ps atom. In the absence of o-Ps to p-Ps conversion reactions 1/4 of the Ps atoms is formed as p-Ps and 3/4 is formed as o-Ps. The continuous energy distribution of the o-Ps three-photon decay results in the enhancement of the photon energy spectrum in the energy region below 511 keV. This is illustrated in Fig. 1.3 where annihilation spectra representing 0% and 100% Ps formation are shown. In order to derive the Ps-fraction, f_{Ps} , from the annihilation spectrum an expression is used^{29,30} which relates the Ps-fraction to the ratio, R , of counts accumulated in different regions of such a spectrum:

$$f_{Ps} = \left[1 + \frac{P_1}{P_0} \frac{R_1 - R}{R - R_0} \right]^{-1}. \quad (1.6)$$

Here R is defined as $(T - P)/P$ where T is the number of counts accumulated in the photon energy region below 511 keV (sensitive to three-photon annihilation events) and P is the number of counts accumulated in a region centered around the 511 keV annihilation line (two-photon events). The value of R varies continuously between R_0 (0% Ps) and R_1 (100% Ps). The factor P_1/P_0 accounts for the probability of three-photon contributions to the number of counts in the peak region. Uncertainties in f_{Ps} introduced by systematical errors and calibration problems have been discussed by Schultz³¹.

The positron beam experiments presented in this thesis are based on the measurement of the Doppler broadening of the 511 keV annihilation peak and the formation of positronium at surfaces.

References chapter 1

1. R. Beringer and C.G. Montgomery, Phys. Rev. **61**, 222, (1942).
2. J.W.M. Dumond, D.A. Lind and B.B. Watson, Phys. Rev. **75**, 1226, (1949).
3. S. de Benedetti and H.J. Richings, Phys. Rev. **85**, 377, (1952).
4. I.K. McKenzie, T.L. Khoo, A.B. McDonald and B.T.A. McKee, Phys. Rev. Lett. **19**, 946, (1967).
5. L. Madanski and I. Rasetti, Phys. Rev. **79**, 397, (1950).
6. W. Cherry, PhD. dissertation, Princeton University (1958).
7. K.G. Lynn, M. Weber, L.O. Roellig, A.P. Mills jr. and A.R. Moodenbaugh, in *Atomic Physics with Positrons*, eds. J.W. Hummerston and E.G.A. Armour (Plenum, New York, 1987), p.161.
8. R.H. Howell, M.J. Fluss, I.J. Rosenberg and P. Mayer, Nucl. Instr. Meth. B **10**, 373, (1985).
9. G. Gräff, R. Ley, A. Osipowicz and G. Werth, Appl. Phys. A **33**, 59, (1984).
10. R. H. Howell, I.J. Rosenberg and M.J. Fluss, Phys. Rev. B **34**, 3069, (1986).
11. J. Lathinen, A. Vehanen, H. Huomo, J. Mäkinen, P. Huttunen, K. Rytsölä, M. Bentzon and P. Hautojärvi, Nucl. Instr. Meth. B **17**, 73, (1986).
12. E.M. Gullikson, A.P. Mills jr, W.S. Crane and B.L. Brown, Phys. Rev. B **32**, 5484, (1985).
13. D.M. Chen, K.G. Lynn, R. Pareja and B. Nielsen, Phys. Rev. B **31**, 4123, (1985).
14. P.J. Schultz, E.M. Gullikson and A.P. Mills jr., Phys. Rev. B **34**, 442, (1986).
15. A.P. Mills jr. and E.M. Gullikson, Appl. Phys. Lett. **49**, 1121, (1986).

16. C.D. Beling, R.I. Simpson, M. Charlton, F.M. Jacobsen and T.C. Griffith, *Appl. Phys. A* **42**, 111, (1987).
17. R.N. West, in *Positrons in Solids*, ed. P. Hautojärvi, (Springer, Berlin, 1979), p.89.
18. W. Triftshäuser and G. Kögel, *Phys. Rev. Lett* **48**, 1741, (1982).
19. R. Mayer and K.G. Lynn, *Phys. Rev. B* **33**, 2507, (1986).
20. A. Weiss, R. Mayer, M. Jibaly, C. Lei, D. Mehl and K.G. Lynn, *Phys. Rev. Lett* **61**, 2245, (1988).
21. D.M. Chen, S. Berko, K.F. Canter, K.G. Lynn, A.P. Mills jr., L.O. Roellig, P. Sferlazzo, M. Weinert and R.N. West, *Phys. Rev. B* **39**, 3966. (1989).
22. G.R. Brandes, K.F. Canter, T.N. Horsky P.H. Lippel and A.P. Mills jr., *Rev. Sci. Instr.* **59**, 288, (1988).
23. J. Van House and A. Rich, *Phys. Rev. B.* **61**, 488, (1988).
24. P.J. Schultz and K.G. Lynn, *Rev. Mod. Phys.* **60**, 701, (1988).
25. R.N. West, in *Positron Studies in Condensed Matter*, Monographs in Physics, eds. B.R. Coles and N. Mott, (Taylor & Francis, London, 1974).
26. K. Hansen, PhD. dissertation, University of Amsterdam, (1988).
27. P. Hautojärvi, J. Heiniö, M. Manninen and R. Nieminen, *Phyl. Mag.* **35**, 973, (1977).
28. I.K. McKenzie, J.A. Cadly and R.R. Gingerich, *Phys. Lett. A* **33**, 279, (1970).
29. M. Deutsch and E. Dulet, *Phys. Rev.* **84**, 601, (1951).
30. M. Leventhal, *Atrophys. J.* **183**, L147, (1973).
31. P.J. Schultz, K.G. Lynn and H.H. Jorch, in *Proc. Int. Workshop on Slow Positrons in Surf. Science, Pajulahti, Finland*, ed. A. Vehanen, (Helsinki Univ. of Technology, Helsinki, 1984).

Chapter 2

Depth profiling with positron beams

2.1 Introduction

The ability of positrons to be effectively used for depth profiling studies is intimately connected with a detailed knowledge of the interaction of positrons with solids and solid surfaces. For this reason a great deal of experimental as well as theoretical work sofar performed has been directed towards the understanding of the fundamental processes occurring when a beam of mono-energetic positrons collides with a solid. In particular attention has been paid to the implantation, thermalization and transport of positrons. Until recently, positrons have always been considered to be thermalized immediately after their implantation and therefore the transport of positrons has been described by a single-velocity diffusion equation. Though this picture has yielded valuable information on the behaviour of positrons in solids, the emission of fast positrons and positronium and the recent observation of non-thermal positron trapping have urged a more accurate description of this problem.

In the first part of this chapter a summary will be given of the present understanding of the interaction of positrons with solids and solid surfaces. In the second part a description will follow of a modelling and fitting program called VEPFIT developed for the analysis of a wide range of problems in positron beam depth profiling experiments.

2.2 Interaction of positrons with solids and solid surfaces

2.2.1 Introduction

A survey of the various interactions that can occur when a beam of mono-energetic positrons collides with a solid is depicted in Fig. 2.1.¹ A short description of the most important processes will follow.

Some of the incident positrons impinging on the surface will be scattered elastically and will form diffracted beams if the surface is crystalline. The not reflected positrons enter the solid and rapidly slow

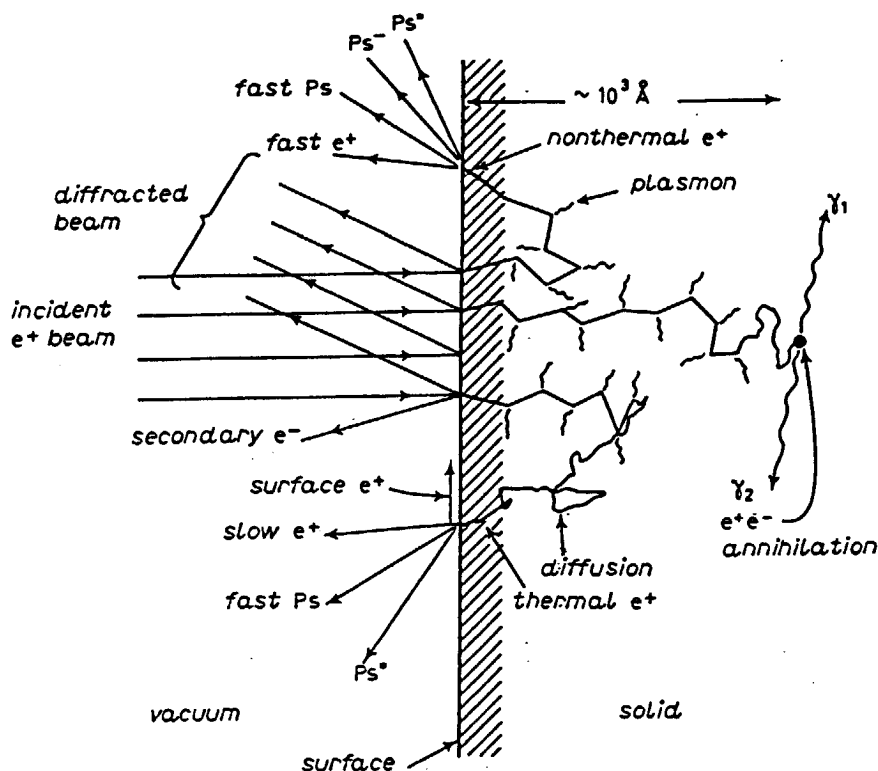


Fig. 2.1. Positron beam interactions with solids and solid surfaces¹.

down to near thermal energies by transferring their energy to the lattice of the material. The main stopping mechanisms in metals by which positrons can transfer their energy are inelastic electron scattering and phonon production.

From initial energy to about 100 eV positron stopping is dominated by electron interactions and the energy loss rate, dE/dt , is proportional to $E^{-1/2}$, where E is the energy of the positron inside the material.² Below 100 eV to a few tens of an eV electronic stopping is still dominant, but in this energy range dE/dt varies with energy as $E^{5/2}$. The time it takes for a positron to slow down to an arbitrary near thermal energy E_c is of the order of a picosecond.

From E_c to thermal energy the positron thermalization is governed by phonon excitations. Phonon excitations have a much lower energy transfer and therefore phonon stopping times are longer than the electronic stopping times. Typical phonon stopping times are of the order of 10 ps.

In semiconductors and ionic solids positron stopping is also governed by these two mechanisms. However, in these materials positron-electron interactions are not longer possible when the energy of the positron becomes less than the band gap of the material. In insulators the final stage in the slowing down process is more complicated because of the formation of quasi-Ps states.

Positrons implanted close to the surface may be scattered back to the surface prior to thermalization. This results in the emission of non-thermal or epithermal positrons^{3,4} and energetic ('hot') positronium⁵. Thermalized positrons can diffuse deeper into the material where they eventually annihilate, either in a free state or in a defect localized state.

Thermal positrons approaching the surface from the inside of the material can undergo one of the following elastic and inelastic surface processes:

- i direct emission as a free positron,
- ii direct emission as Ps,
- iii trapping into a two-dimensional or defect localized positron surface state, and
- iv reflection by the positron surface potential.

The direct emission of a free positron is only possible if the positron

work function ϕ_+ is negative. As illustrated in Fig. 2.2, the positron work function, defined as the minimum energy required to remove a positron from a position inside to a position just outside the surface, can be expressed as:

$$\phi_+ = -E_0 - E_{corr} - D, \quad (2.1)$$

where E_0 is the positron zero-point energy representing the repulsive interaction of the positrons with the ion cores and D is the surface dipole barrier caused by the penetration of electrons into the vacuum. The (negative) correlation energy, E_{corr} , accounts for the interaction between the positron and the cloud of electrons. For low electron densities the value of E_{corr} approaches the positronium binding energy, $E_{Ps} = -6.8 \text{ eV} = \frac{1}{2}R_\infty$ ⁷.

Ps emission by the pick up of a near surface electron is possible if the sum of the positron work function ϕ_+ and the electron work function ϕ_- is less than the binding energy of the Ps atom. Also depicted in Fig. 2.2 is an attractive surface potential well for positrons near the surface. This well is due to image forces at large distances and the correlation energy with the low density electron gas at short distances. Positron trapping at the surface can be followed either by annihilation in this state or by thermal desorption from this state. In the latter case positronium is formed which occurs for most materials only at elevated temperatures. The formation of excited (Ps^*) and negatively charged (Ps^-) positronium states has been observed⁶, but is of little importance in depth profiling experiments.

The quantum mechanical reflection of thermal positrons by the surface potential has for long been a subject of debate, mainly due to a discrepancy between theoretical predictions² and experimental observations^{8,9}. Quantum mechanical calculations predict complete positron reflection for temperatures close to 0 K and therewith vanishing direct positron and positronium emission (the first two elastical surface processes mentioned above). However, experimental observations indicate only a weak temperature dependence so they do not support these predictions. To account for this difference several explanations have been proposed, e.g. inelastic surface processes¹⁰ and multiple approaches of reflected positrons to the surface¹¹. Recently, it has been suggested that this discrepancy might be ascribed to the inap-

appropriate separation of thermal and epithermal positron contributions to the earlier measured Ps-fraction data¹².

Though there is still some discussion whether the discrepancy noticed here can be fully ascribed to epithermal positrons, it has become clear that epithermal positron effects should be understood in more detail in order to come to a reliable interpretation of all experimental data. Epithermal positron effects will be the subject of the next section.

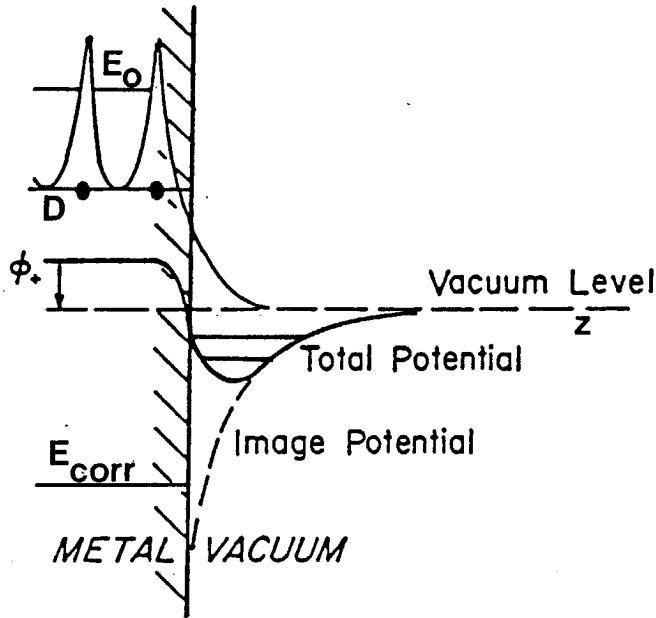


Fig. 2.2. Potential energy diagram for a thermalized positron at a metallic surface. The work function, ϕ_+ , is a combination of the bulk chemical potential and the surface dipole barrier D . The positron chemical potential includes terms due to correlation with the electron cloud (E_{corr}) and a repulsive interaction of positrons with the ion cores (E_0). The attractive potential outside the metal is due to image forces and is for large distances proportional to z^{-1} where z is the distance from the surface. Indicated are energy levels of positrons trapped in the surface state.

2.2.2 Epithermal positron effects

Since in dense materials the positron thermalization times are short compared to the positron lifetime, positrons have always been assumed to be completely thermalized immediately after their implantation. For this reason, the transport of positrons has been described by the single-velocity diffusion equation instead of the appropriate multi-velocity diffusion equation. In the diffusion model the annihilation and trapping of positrons are considered for thermal positrons only. Though this picture yields valuable information on the behaviour of positrons in solids, it has a limited validity in that the final stage of the thermalization process is not treated correctly. The emission of epithermal positrons and the formation of energetic positronium are two examples indicative of this shortcoming. Moreover, recently a strongly enhanced trapping probability was found for epithermal positrons with an energy of about 1 eV for defects in Al and Cu³. This observation is supported by model calculations¹³ which indicate the existence of a resonance in the positron trapping process for positrons slowing down from near thermal to thermal energies.

Besides taking part in a resonant trapping process, epithermal positrons implanted in the very near surface region (typically within a few nm) may reach the surface prior to thermalization. The subsequent formation of Ps thus contributes to the Ps-fraction signal and therefore the direct employment of the diffusion model for the analysis of Ps-fraction measurements is likely to yield erroneous results. For example, in several metals the temperature dependence⁴ of the positron diffusion coefficient, D_+ , was found to be stronger than the predicted $T^{-1/2}$ behaviour¹⁵. This inconsistency has been associated with epithermal positrons and could be solved if the Ps-fraction data obtained at positron energies below 4 keV were excluded from the analysis¹⁶.

Another aspect which cannot be accounted for by the one-level diffusion model is the (de)acceleration or reflection of (thermal) positrons passing an interfacial region separating two materials with different chemical potentials¹⁷. Positrons passing the interface may gain kinetic energy corresponding to the drop in the chemical potential, whereafter they are liable to epithermal positron trapping or epithermal positron emission. Epithermal positron emission may also be enhanced by the

application of an external electric field in combination with insulating or semiconducting materials. This aspect is relevant to the recently proposed field assisted positron moderators¹⁸.

Several models have been suggested in order to separate contributions of epithermal positrons from those due to thermal positrons^{16,19,20}. One of these²⁰ is based on a two-level diffusion model in which positrons are assumed to be in either an epithermal or a thermal state. The thermalization process is represented by the transition from the high energy state to the low energy state. The epithermal state further exhibits the resonant trapping process, represented by an epithermal positron trapping rate. Positrons in the thermal state are assumed to be fully thermalized and therefore obey the diffusion equation for thermal positrons. First results indicate that this model gives a more complete description of the transport of positrons implanted with variable energies.

A logical next step of sophistication is the development of a multi-level diffusion model. Current work by Kong²⁰ is being done in this direction. In section 2.3 it will be shown how this model can be included in the modelling and fitting program presented in this thesis.

2.2.3 Positron implantation profile

The feasibility of depth profiling measurements with variable energy positrons is critically dependent on a proper knowledge of the spatial distribution of the positrons after implantation. This distribution is represented by the positron implantation profile, $P(z, E)$, where $P(z, E)dz$ is defined as the fraction of positrons entering the solid with initial energy E that will be stopped at a depth between z and $z + dz$.

Information on the positron stopping profile has been obtained in several ways. Mills and Wilson²¹ have studied the implantation of positrons by measuring the transmission probability of 1 to 6 keV positrons through thin, wedge shaped Al, Cu and Si foils. They derived the implantation profiles by differentiating the transmission curves measured *vs.* foil thickness for different positron incident energies. Furthermore, they showed that the positron mean penetration depth varied with energy according to a power law dependence,

$$R = AE^n. \quad (2.2)$$

In this expression, which was originally developed for electron stopping, R is the positron mean penetration depth, E is the positron incident energy and A is a material dependent proportionality constant.

Nieminen, Oliva² and Valkealahti²² simulated the implantation of keV electrons and positrons by Monte Carlo calculations. In these simulations the slowing down of the particles was followed from 10 keV initial energy down to an end-point energy of 20 eV. Their calculated mean penetration depths were in agreement with those obtained from the transmission experiments. The positron implantation profiles, however, were found to agree less well. The authors attributed this discrepancy to positron backscattering effects which were not accounted for in the analysis of the transmission measurements. In addition, they showed that the simulated implantation profiles could be parameterized fairly well by a so-called Makhov distribution;

$$P(z, E) = \frac{mz^{m-1}}{z_0^m} \exp[-(z/z_0)^m] \quad (2.3)$$

with m being a shape parameter. The energy dependent parameter z_0 is related to the mean implantation depth, \bar{z} , by:

$$\bar{z} = z_0 \Gamma\left(\frac{m+1}{m}\right) \quad (2.4)$$

with \bar{z} defined as (see also eq. (2.2))

$$\bar{z} = \frac{\alpha}{\rho} E^n. \quad (2.5)$$

In this expression ρ is the density of the material and α a constant which is considered to be material independent.

Recently, Vehanen²³ has given accurate values for the parameters describing the generally accepted Makhov distribution. The values reported for m , n and α are 2.0 ± 0.1 , 1.62 ± 0.05 and $(4.0 \pm 0.3) \mu\text{g cm}^{-2} \cdot \text{keV}^{-1.62}$, respectively, consistent with values derived from Monte Carlo calculations.

2.2.4 Positron diffusion equation

The diffusion of thermalized positrons in solids is mainly governed by the Coulomb interactions between the positron and the electrons and

the ion cores. In a periodic lattice the repulsive ion cores produce a periodic potential which has its minima located between the lattice positions of the ion cores. As a result, the positron wavefunction can be described by a Bloch-like wave with a half-wavelength equal to the lattice spacing. This quantum picture of a positron in a solid implies that the positron carries a zero-point energy E_0 , the value of which depends on the lattice structure, the lattice spacing and the size and the valence of the repelling ion cores. Removal of one or more ion cores from the lattice will lead to an excess of negative charges due to the presence of conduction electrons. The subsequent redistribution of the electronic charges will result in a much deeper potential well at the location of the missing cores. If the energy level of a positron inside this well lies below the energy of a free positron, trapping may occur.

Thus far, the transport of thermal positrons in combination with trapping at defects has been described by the one-dimensional steady-state diffusion equation

$$D_+ \frac{d^2 c(z)}{dz^2} - \frac{d(v_d(z)c(z))}{dz} - (\nu_t n_t(z) + \lambda_b)c(z) + I(z) = 0 \quad (2.6)$$

where

- D_+ = the positron diffusion coefficient ($\text{cm}^2.\text{s}^{-1}$),
- $c(z)$ = the steady state positron distribution (at.fr.),
- $v_d(z) = \mu E(z)$ = the positron drift velocity ($\text{cm}.\text{s}^{-1}$), with
- $E(z)$ = the electric field strength ($\text{V}.\text{cm}^{-1}$),
- μ = $eD_+/k_B T$ = the positron mobility ($\text{cm}^2.\text{V}^{-1}.\text{s}^{-1}$),
- ν_t = specific positron trapping rate for defects (s^{-1}),
- $n_t(z)$ = defect concentration (at.fr.),
- λ_b = bulk annihilation rate (s^{-1}), and
- $I(z)$ = the energy dependent positron implantation rate (at.fr. s^{-1}).

This equation can be generalized and normalized to describe the averaged fate per implanted positron. In doing so we introduce a normalized positron implantation profile

$$p(z^*) = \frac{I(z^*)}{\int_0^\infty I(z^*) dz^*} \quad (2.7)$$

and a generalized positron distribution

$$c^*(z^*) = \frac{D_+ c(z^*)}{a^2 \int_0^\infty I(z^*) dz^*}. \quad (2.8)$$

Here $z^* = z/a$ is a dimensionless depth parameter where a can be chosen freely (e.g. a = the lattice parameter). Accordingly, the generalized drift velocity is rewritten as

$$v_d^*(z^*) = \frac{a}{D_+} v_d(z^*) = \frac{a e E(z^*)}{k_B T} \quad (2.9)$$

where k_B is the Boltzmann constant. This finally yields

$$\frac{d^2 c^*}{dz^{*2}} - \frac{d(v_d^* c^*)}{dz^*} - \frac{a^2}{D_+} (\nu_l n_l + \lambda_b) c^* + p = 0. \quad (2.10)$$

Depth integration of eq. (2.10) gives

$$\left(\frac{dc^*}{dz^*} \right)_{z^*=0} - v_d^*(0) c^*(0) - \frac{a^2}{D_+} \int_0^\infty (k_l n_l + \lambda_b) c^* dz^* + 1 = 0 \quad (2.11)$$

or

$$-F_s - F_t - F_b + 1 = 0 \quad (2.12)$$

with F_s , F_t and F_b the fractions of the implanted positrons back-diffused to the surface, trapped at defects and annihilated in the bulk, respectively. Note that in eq. (2.11) the boundary conditions for z approaching infinity are set to zero

$$\left(\frac{dc^*}{dz^*} \right)_{z^*=\infty} = 0; \quad c^*(\infty) = 0. \quad (2.13)$$

These conditions are fulfilled if the concentration of positrons at large depths becomes negligible. This is true for most beam experiments as the thickness of the samples (> 1 mm) is much larger than the maximum attainable positron implantation depth ($\sim 1 \mu\text{m}$).

The boundary condition at the surface ($z = 0$) is given by

$$\left(\frac{dc}{dz} \right)_{z=0} = \frac{c(0)}{L_a} \quad (2.14)$$

with L_a an apparent surface absorption length. In literature this condition is often presented as the *radiative* boundary condition

$$c(0) = \frac{D_+}{\nu} \left(\frac{dc}{dz} \right)_{z=0} \quad (2.15)$$

with ν being the "velocity" of all surface processes capable of removing positrons from the surface into the vacuum. Hence, L_a and ν are related by $L_a = D_+/\nu$.

The surface absorption length L_a has no direct physical meaning, other than that it indicates how to extrapolate the solution of eq. (2.6) at the surface boundary. L_a is considered to account for the following surface related effects:

1. Solving the positron transport problem using a diffusion approximation with the condition of a perfectly absorbing surface boundary causes inaccuracies in the positron density at distances smaller than or comparable with the positron mean free path, \bar{L} , which is of the order of 10 Å. A better approximation is obtained when $c(-L_a) = 0$, with $L_a = 0.71 \bar{L}$, is taken as boundary condition. This condition, commonly imposed on outer surfaces in neutron transport problems²⁴, is equivalent to the condition given by eq. (2.14).

2. Partial reflection of positrons arriving at the surface will also lead to changes in the absorbing properties of the surface. Defining the reflection coefficient, r , as the ratio between the outward directed positron flux and the inward directed flux, it follows that

$$\left(\frac{dc}{dz} \right)_{z=0} = \frac{(1-r)}{(1+r)} \frac{c(0)}{0.71 \bar{L}} \quad (2.16)$$

and thus

$$L_a = 0.71 \bar{L} \frac{(1+r)}{(1-r)} \quad (2.17)$$

Accordingly ν is rewritten as

$$\nu = \frac{D_+}{0.71 \bar{L}} \frac{(1-r)}{(1+r)} = \nu_o \frac{(1-r)}{(1+r)}. \quad (2.18)$$

3. In realistic cases positrons arriving at the surface interact with the surface in different ways (see section 2.2.1) Apart from elastic interactions (positron and Ps emission) inelastic interactions may occur

(e.g. surface trapping). If we denote the transmission probability representing the elastic processes by t_{el} and the surface trapping probability by t_{inel} , then the reflection coefficient is given by $r = 1 - t_{el} - t_{inel}$. The parameter ν then will be given by

$$\nu = \nu_o \frac{t_{el} + t_{inel}}{2 - t_{el} - t_{inel}}. \quad (2.19)$$

Recently, Britton et al.¹² suggested a more simple expression for ν

$$\nu = \nu_o' t_{el} + \nu_s \quad (2.20)$$

Compared with eq. (2.19) this expression assumes no dependence of t_{el} on the denominator. At present it is not known how their fitted values for ν_o' and ν_s would be affected by including this dependence. It is interesting to note that their value for ν_o' corresponds well with the calculated value of $\nu = 5 \times 10^6 \text{ cm.s}^{-1}$ at 300 K, where we have taken values for D_+ ²⁵ and L_a of $1 \text{ cm}^2.\text{s}^{-1}$ and 20 \AA , respectively.

In homogeneous defect free media the fraction of positrons back-diffusing to the surface, F_s , can be calculated analytically by

$$F_s(E) = \int_0^\infty P(z, E) \exp\left[-\left(\frac{z}{L_+}\right)\right] dz \quad (2.21)$$

with the L_+ the diffusion length. L_+ is related to the positron diffusion coefficient by

$$L_+ = \sqrt{D_+ \tau_b} = \sqrt{\frac{D_+}{\lambda_b}} \quad (2.22)$$

with $\tau_b = \lambda_b^{-1}$ being the positron bulk (free) lifetime. In materials with a uniform defect distribution L_+ is reduced to an effective diffusion length, $L_{+,eff}$, given by

$$L_{+,eff} = \sqrt{\frac{D_+}{\lambda_b + \kappa_t}} \quad (2.23)$$

where $\kappa_t = \nu_t n_t$ is the positron trapping rate into defects.

The value of $L_{+,eff}$ can be obtained directly by fitting the backdiffusion probability to Ps-fraction measurements and with the knowledge of the positron specific trapping rate yields the defect concentration. In

cases where the formation of Ps is suppressed, e.g. due to contamination of the surface, the defect density can be derived from S-parameter measurements. These measurements then are compared with calculated $S(E)$ values, which in case of a uniformly defected material are given by

$$S(E) = F_s S_s + (1 - F_s) S'. \quad (2.24)$$

Here S' represents an averaged S value for positrons annihilating inside the material

$$S' = \frac{\lambda_b S_b + \kappa_t S_t}{\lambda_b + \kappa_t} \quad (2.25)$$

The subscripts s , b and t denote surface, bulk and defect S values, respectively.

In realistic cases however, defects will be distributed according to some unknown profile and therefore the diffusion equation can only be solved iteratively. In the next section a modelling and fitting program will be presented which has been developed for this purpose.

2.3 Modelling and fitting of positron beam experiments

2.3.1 Introduction

The advent of positron beams with energies that can be varied from 0 to tens of keV has given an impetus to the development of depth resolved positron analysis methods. Reviews on positron beam analysis on a variety of problems have been given by Schultz and Lynn²⁵, and Vehanen²⁶.

The introduction of the depth as a variable makes it necessary to have modelling and fitting programs available which describe the depth dependent trapping of positrons. An outline of the positron trapping problem has been given by Lynn²⁷. Modelling and fitting procedures based on analytical solutions of the diffusion equation in the case of a simple defect profile have been given by several authors^{28,29,30}. Recently, Schultz³¹ reported on a numerical method which included the presence of electric fields (in silicon).

In this section will be reported on the development of a method applicable for a wide range of depth profiling problems in positron beam analysis. In the following section (2.3.2) an outline will be given of a fast numerical method for solving the diffusion equation presented in the previous section. The fitting program named VEPFIT is introduced in section (2.3.3). The results of fitting of simulated and experimental data will be presented in section (2.3.4). The performance of the fitting method will be discussed in section (2.3.5). In section (2.3.6) a general discussion follows. Finally, in section (2.3.7) the conclusions will be given.

2.3.2 A fast method for numerical solution of the diffusion equation

In positron beam experiments the mean range and the variance of the range (range straggling) of the implanted positrons are strongly correlated. For the Makhov implantation profile given by eq. (2.3) with $m = 2$ the range straggling is exactly proportional to the mean range. Furthermore, for all positron incident energies the absolute value of the derivative of the implantation profile with respect to the depth, $dP(z, E)/dz$, has its maximum for $z = 0$. Therefore the depth intervals, Δz , to be chosen for the discretization of the problem can be taken to increase proportionally with the depth z .

When the defect distribution $n_t(z)$ or the electric field $E(z)$ are varying faster with z than the positron implantation profile the discretization should be adapted accordingly. In the following method we assume that $P(z, E)$, $n_t(z)$ and $E(z)$ are slowly varying functions over a given depth interval between z and $z + \Delta z$ and therefore can be taken constant over that interval.

First we will describe the solution method in case electric fields are not present, i.e. $E(z) = 0$. The general solution of eq. (2.10) in each interval is given by

$$c(z) = A \exp(\gamma z) + B \exp(-\gamma z) + \frac{p}{\alpha} \quad (2.26)$$

where $\alpha = a^2 (\kappa_t + \lambda_b)/D_+$ and $\gamma = \sqrt{\alpha}$. Indexing the constants A , B , α and γ with the numbers assigned to the depth intervals as indicated

in Fig. 2.3. and imposing continuity of c and $c' = dc/dz$ at the interval boundaries we get for each interval the following relations

$$c_i(z_i) = c_{i+1}(z_i) \quad i = 1, \dots, N-1 \quad (2.27)$$

and

$$c'_i(z_i) = c'_{i+1}(z_i) \quad i = 1, \dots, N-1 \quad (2.28)$$

The $2N$ constants A_i and B_i for the N intervals can be calculated from the $2(N-1)$ relations together with the two boundary conditions at z_0 and z_N . The first mentioned boundary condition has been given by eq. (2.14). The latter is chosen to be

$$\left(\frac{dc}{dz} \right)_{z=z_N} = -\frac{c(z_N)}{L_+} \quad (2.29)$$

and is valid for depths beyond which no positrons are stopped and no defects are present. In cases where beyond z_N a constant defect density is present, L_+ is replaced by $L_{+,eff}$.

Solving this set of equations requires the inversion of a $2N \times 2N$ matrix. Another approach, which in a straightforward manner gives the values

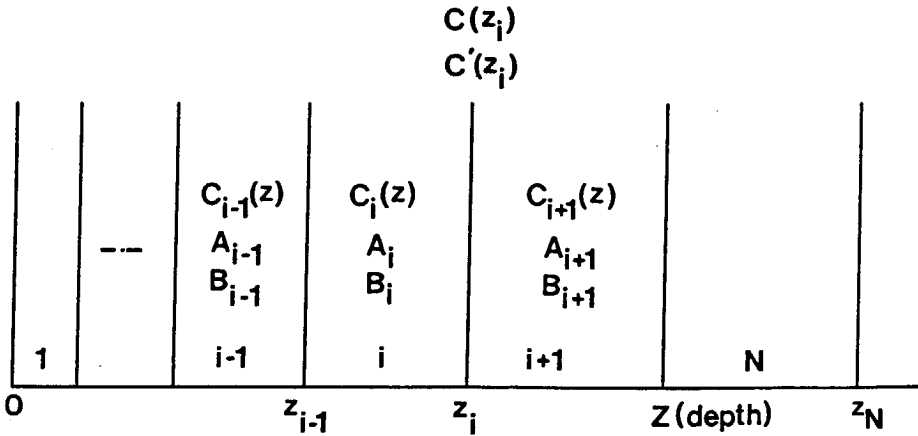


Fig. 2.3. Definition of depth discretization intervals and corresponding positron densities, derivatives and integration constants.

of $c'_i (i = 1, \dots, N)$ necessary for the calculation of F_s , F_b and F_l is as follows.

Elimination of A_i and B_i from eq. (2.26) yields $2N$ linear equations in c_i and c'_i . The equations can be rearranged so that, when written in matrix form, two matrix equations remain

$$\mathbf{A} \vec{c} = \vec{b} \quad (2.30)$$

and

$$\mathbf{A}' \vec{c}' = \vec{b}' \quad (2.31)$$

where \mathbf{A} and \mathbf{A}' are $(N+1) \times (N+1)$ tridiagonal matrices, \vec{c} and \vec{c}' the vectors (c_0, \dots, c_N) and (c'_0, \dots, c'_N) , respectively. The vectors \vec{b} and \vec{b}' contain values related to the implantation profile.

Since we are interested in the solution of the matrix given in eq. (2.31) we give only matrix and vector elements for this case (see Table 2.1.) Additional information on the derivation of this equation is given by De Vries and Van Veen³².

When electric fields are included a slightly different approach is followed. The general solution in an interval in this case is written as

Table 2.1. Matrix coefficients and vectors of $\mathbf{A}' \vec{c}' = \vec{b}'$. (The dummy variable i ranges from 1 to $N-1$.)

$a_{0,0}$	$= 2L_a + f_1/\gamma_1 + 1/\gamma_1 f_1$	b_0	$= 2p_1/\gamma_1^2$
$a_{0,1}$	$= -f_1/\gamma_1 + 1/\gamma_1 f_1$		
$a_{i,i-1}$	$= -f_i/\gamma_i + 1/\gamma_i f_i$		
$a_{i,i}$	$= f_i/\gamma_i + 1/\gamma_i f_i +$ $f_{i+1}/\gamma_{i+1} + 1/f_{i+1} \gamma_{i+1}$	b_i	$= -2(p_i/\gamma_i^2 + p_{i+1}/\gamma_{i+1}^2)$
$a_{i,i+1}$	$= -f_{i+1}/\gamma_{i+1} - 1/\gamma_{i+1} f_{i+1}$		
$a_{N,N-1}$	$= -f_N/\gamma_N + 1/\gamma_N f_N$		
$a_{N,N}$	$= 2L_D + f_N/\gamma_N + 1/\gamma_N f_N$	b_N	$= -2p_N/\gamma_N^2$
f_i	$= (e^{\gamma_i z_i} + e^{\gamma_i z_{i-1}})/(e^{\gamma_i z_i} - e^{\gamma_i z_{i-1}})$		

(with $v_d = \mu E$)

$$c(z) = A \exp(\gamma^+ z) + B \exp(\gamma^- z) + \frac{p}{\alpha} \quad (2.32)$$

where

$$\gamma^{+,-} = \frac{1}{2} (-v_d \pm \sqrt{v_d^2 + 4\gamma^2}) \quad (2.33)$$

At the interval boundaries continuity is required for the positron concentration and the positron current density so that in this case for $i = 1, \dots, N-1$

$$c'_i(z_i) - v_{d,i} c_i(z_i) = c'_{i+1}(z_i) - v_{d,i+1} c_{i+1}(z_i) \quad (2.34)$$

It is assumed that no electric fields are present at the boundary $z = z_N$. At the surface the boundary condition with an electric field is given by

$$c'_1(0) = (v_{d,1} + \frac{1}{L_a}) c_1(0) \quad (2.35)$$

Also in this case \vec{c} and \vec{c}' can be obtained from two matrix equations. It should be noted that the vector \vec{c}' can be defined in two ways: either for z approaching the boundary from the left ($z < z_i$) or for z approaching the boundary from the right ($z > z_i$). We have chosen for the latter definition, thus $c'(z_i) = c'_{i+1}(z_i)$. In case of electric fields both vectors \vec{c} and \vec{c}' have to be calculated in order to obtain the different fractions. The matrix and the vector elements for this case are given in Table 2.2.

The method of solution is based on the usual elimination procedure for tridiagonal matrices³³. The matrices originating from the diffusion problem described here are never ill-conditioned. A high accuracy is always obtained and therefore there is no need using time consuming iterative procedures³².

Table 2.2. Elements of the matrix equations for the case of electric fields.

	$\mathbf{A} \vec{c} = \vec{b}$	$\mathbf{A}' \vec{c}' = \vec{b}'$
$a_{0,0}$	$-(s_0\delta_1^+ + \delta_1^-)/L_a + s_0\alpha_1^+ + \alpha_1^-$	$(s_0\alpha_1^+ + \alpha_1^-)/L_a - s_0\delta_1^+ - \delta_1^-$
$a_{i,i-1}^*$	$u_i\alpha_i^+ + q_i\alpha_i^-$	$-u_i\delta_i^+ - q_i\delta_i^-$
$a_{i,i}^\dagger$	$-u_i\eta_i^+ - q_i\eta_i^- + s_i\alpha_{i+1}^+ + \alpha_{i+1}^-$	$u_i\epsilon_i^+ + q_i\epsilon_i^- - s_i\delta_{i+1}^+ - \delta_{i+1}^-$
$a_{i,i+1}^\ddagger$	$-s_i\eta_{i+1}^+ - \eta_{i+1}^-$	$s_i\epsilon_{i+1}^+ + \epsilon_{i+1}^-$
$a_{N,N}$	$-u_N\beta_N^+ - \beta_N^- - (u_N\epsilon_N^+ + \epsilon_N^-) L_{eff}$	$u_N\epsilon_N^+ + \epsilon_N^- + (u_N\beta_N^+ + \beta_N^-) L_{eff}$
b_0	$2s_0p_1/\gamma_1^2$	
b_i^\dagger	$2u_i p_i/\gamma_i^2 + 2s_i p_{i+1}/\gamma_{i+1}^2$	
b_N	$2u_N p_N/\gamma_N^2$	
u_i	$\frac{\delta_i^- \alpha_{i+1}^- \gamma_i^2}{\epsilon_{i+1}^+ \alpha_i^- \gamma_{i+1}^2}$	$\frac{\alpha_i^- (\alpha_{i+1}^- \eta_{i+1}^+ - \alpha_{i+1}^+ \eta_{i+1}^-)}{\eta_{i+1}^+ (\alpha_i^- \eta_i^+ - \alpha_i^+ \eta_i^-)}$
u_N	$-\delta_N^-/\delta_N^+$	$-\alpha_N^-/\alpha_N^+$
q_i	$-(\delta_i^+/\delta_i^-) u_i$	$-(\alpha_i^+/\alpha_i^-) u_i$
s_i	$-\epsilon_{i+1}^-/\epsilon_{i+1}^+$	$-\eta_{i+1}^-/\eta_{i+1}^+$
$\alpha_i^{+,-} = r_i/(r_i - 1) \pm t_i/(t_i - 1)$	$\beta_i^{+,-} = 1/(r_i - 1) \pm 1/(t_i - 1)$	
$\gamma_i^{+,-} = -\frac{1}{2} v_{d_i} \pm \frac{1}{2} \sqrt{v_{d_i}^2 + 4\gamma_i^2}$	$\delta_i^{+,-} = r_i/\gamma_i^- (r_i - 1) \pm t_i/\gamma_i^+ (t_i - 1)$	
$\epsilon_i^{+,-} = 1/\gamma_i^- (r_i - 1) \pm 1/\gamma_i^+ (t_i - 1)$	$\eta_i^{+,-} = \beta_i^{+,-} - \epsilon_i^{+,-} (v_{d_i} - v_{d_{i+1}})$	
$r_i = \exp(\gamma_i^+ (z_i - z_{i-1}))$	$t_i = \exp(\gamma_i^- (z_i - z_{i-1}))$	

* $i = 1, \dots, N$

† $i = 1, \dots, N - 1$

‡ $i = 0, \dots, N - 1$

2.3.3 Application to F_{Ps} and S-parameter measurements

The solutions of \vec{c} and \vec{c}' are used to calculate the fractions $t_{i,j}$ of positrons implanted in interval j that are trapped in interval i

$$t_{i,j} = c'_{i+1}(z_i) - c'_i(z_{i-1}) - v_{d,i+1} c_{i+1}(z_i) + v_{d,i} c_i(z_{i-1}) + (z_j - z_{j-1}) p_j \quad (2.36)$$

where $p_j = 1/(z_j - z_{j-1})$ if $j = i$ and $p_j = 0$ if $j \neq i$. In total, this matrix contains N^2 matrix elements. The matrix depends only on the depth distribution of the defects and therefore can be used to calculate positron trapping and surface transmission for any positron implantation profile. This is in particular useful when the positron incident energy and therewith the implantation profile is varied.

The total fraction of positrons, $T_i(E)$, entering the solid with energy E that will annihilate in depth interval i is given by

$$T_i(E) = \sum_{j=1}^N P_j(E) t_{i,j} \quad (2.37)$$

with $P_j(E)$ the probability for implantation in interval j . For the Makhov profile the probability is given by

$$P_j(E) = \exp[-(z_{j-1}/z_0)^m] - \exp[-(z_j/z_0)^m] \quad (2.38)$$

The fraction of positrons diffusing back to the surface, $F_s(E)$, can be derived from

$$F_s(E) = 1 - \sum_{i=1}^N T_i(E) \quad (2.39)$$

Assuming that positronium is only formed at the surface of the sample the experimentally obtained Ps-fraction, f_{Ps} , can be written as

$$f_{Ps}(E) = f_0 F_s(E) \quad (2.40)$$

with f_0 a proportionality constant.

Defining separate S-values, S_i , for each interval and an S-value, S_s , for positrons annihilating at the surface, the S-parameter as a function of the positron incident energy can be expressed as

$$S(E) = F_s S_s + \sum_{i=1}^N S_i T_i \quad (2.41)$$

To be able to fit f_{Ps} and S-parameter curves for low positron energy, it is necessary to implement some treatment of epithermal positrons. A complete treatment of this effect requires the solution of a multi-group diffusion equation. At this stage, however, we use a simple method suggested by Britton¹⁹, in which a fraction of the implanted positrons is diffusing back to the surface. This fraction, $F_{epi}(E)$, is determined by a scattering length, l_{epi} , and shows

$$F_{epi}(E) = \int_0^\infty P(z, E) \exp[-(z/l_{epi})] dz \quad (2.42)$$

This treatment implies that $S(E)$ and $f_{Ps}(E)$ should be rewritten as

$$S'(E) = S(E)(1 - F_{epi}(E)) + S_{epi} F_{epi}(E) \quad (2.43)$$

$$f'_{Ps}(E) = f_{Ps}(E)(1 - F_{epi}(E)) + f_{0,epi} F_{epi}(E) \quad (2.44)$$

Following the calculation method outlined here, any experiment dealing with a positron beam interacting with a solid can be modelled, as long as diffusion theory applies. The input parameters that may be required are summarized in Table 2.3. In the program VEPFIT a choice can be made from 5 models which cover most of the positron beam experiments currently being carried out. In Table 2.3 the characteristics of the different models are given. Model #1 is a general model in that it allows a free choice of all parameters. Model #5 is capable of modelling a layered structure composed of materials with densities different from that of the substrate. The differences in density of the layers are accounted for by a modified positron implantation profile introduced by Vehanen²³.

In the other models certain restrictions are superimposed and are therefore mainly used for fitting of experimental data.

Table 2.3. Models and model parameters in VEPFIT.

bulk or substrate	L_+, S_b	
surface	L_a, S_s, f_0	
epithermals	$L_{epi}, S_{epi}, f_{0,epi}$	
defects and electric fields	$L_{+,eff,i}, S_i$ $v_{d,i}, \rho_i$	model #1 general
	$L_{+,eff,i}, S_t$ $v_{d,i}, \rho$	model #2 single type defects
	A_L, σ_L, z_L, S_t A_v, σ_v, z_v, ρ	model #3 gaussian distribution of defects or electric fields
	$L_{+,eff,l}, l_{max}, z_l, S_t$ $v_{d,l}, \rho$	model #4 layered structure of defects or electric fields
	$L_{+,eff,l}, l_{max}, z_l, S_l$ $v_{d,l}, \rho_l$	model #5 layered structure of different materials
positron stopping	P_j, m, n, α	Makhov profile

Meaning of the indices: *b* - bulk; *s* - surface; *t* - trapping in defects; *epi* - epithermals; *i* - interval number; *l* - layer number; *d* - drift; *L* - parameters needed for the calculation of a diffusion length (*L*); *v* - parameters needed for the calculation of a drift velocity (*v_d*).

2.3.4 Fitting program

The opposite of modelling, i.e. the retrieval of model parameters from measured S-parameter and Ps-fraction data is a far more complicated task than the modelling itself. Fitting requires repeatedly modelling with a restricted set of parameters. Therefore the developed method for accurate and fast modelling has formed a crucial element in the VEPFIT program.

Experimental data will only contain information sufficient to fit a part of the parameters describing the model. Therefore, apart from the possibility of fixing any parameter in model #1, we can use the other models to effectuate a relation between S-parameters, the effective diffusion lengths and/or electric field strengths. The coupling between the different parameters in these models will be discussed in the following.

model #2.

In this model $S(E)$ is described in terms of bulk and defect S-values, S_b and S_t respectively, instead of an S-value for each interval. This means that the S-values are coupled to the diffusion lengths under the assumption that only one type of defect exists:

$$S(E) = S_b \sum_{i=1}^N T_i L_{+,eff,i}^2 / L_+^2 + S_t \sum_{i=1}^N T_i (1 - L_{+,eff,i}^2 / L_+^2) + S_s (1 - \sum_{i=1}^N T_i). \quad (2.45)$$

The effective diffusion length is related to the defect trapping rate by

$$\left(\frac{L_{+,eff,i}}{L_+} \right)^2 = \frac{\lambda_b}{\lambda_b + n_i \nu_t}. \quad (2.46)$$

In this expression the positron specific trapping rate, ν_t , is assumed to be independent of the depth so that information is obtained on the depth profile of the defects.

model #3.

In this model the defect concentration and/or the electric field strengths are described by a gaussian distribution. During the fitting procedure the effective diffusion lengths are calculated as follows

$$1/L_{+,eff,i}^2 = 1/L_+^2 + A_L \exp[-((z'_i - z_L)/\sigma_L)^2 / 2] \quad (2.47)$$

and positron drift velocities

$$v_{d,i} = A_v \exp[-((z'_i - z_v)/\sigma_v)^2 / 2] \quad (2.48)$$

where $z'_i = (z_{i+1} - z_i)/2$ are interval centers. The values of the extrema A_L and A_v , the positions of the extrema z_L and z_v , and the standard deviations σ_L and σ_v are the fitting parameters. The extremum A_L is always positive. The total number of defects (depth integrated), N_t , is related to A_L as follows

$$N_t = A_L \nu_t^{-1} \lambda_b L_+^2 (\pi/2)^{-1/2} \sigma_L^{-1} [1 + \operatorname{erf}(z_L/(\sigma_L \sqrt{2}))]^{-1} \quad (2.49)$$

A_v represents the extremum of the positron drift velocity; positive for inward directed electric fields (positive z -direction) and negative in the reversed case. The S-parameters are coupled to the diffusion lengths in the same way as given in model #2.

model #4.

This model is used to find a number of zones with distinct values of the diffusion lengths and/or electric fields. The defect concentration is assumed to have a block shaped distribution in an otherwise uniformly composed material. While fitting, the defect boundary positions, z_l , may become situated between two adjacent interval boundaries. In this case the defect boundaries are not inserted to split up the original interval but remain virtual boundaries. The presence of a defect boundary in the i^{th} interval is accounted for by adopting a weighted value of the diffusion length in that interval;

$$L_{+,eff,i} = (z_l - z_{i-1}) L_{+,eff,l} + (z_i - z_l) L_{+,eff,l+1} \quad (2.50)$$

S-parameter values are again coupled to the diffusion lengths as in the previous models.

model #5.

This model represents a layered structure which may be composed of different materials. To each layer an S-value S_l is assigned. This value is not related to the diffusion length of the layer. An implication is, that, to have linear S-fitting, the layer boundaries have to coincide with the interval boundaries. In the program, an extra interval is inserted for each layer boundary. When fitting the position of a layer boundary the interval distribution and the implantation profile have to be recalculated before every function evaluation. For a layered structure $S(E)$ is expressed as

$$S(E) = F_s S_s + \sum_{l=1}^{N_l} (S_l \sum_{i=i_1}^{i_2} T_i) \quad (2.51)$$

where N_l is the number of layers with the l^{th} layer covering the intervals i_1 to i_2 .

It can be shown that the results are correctly described by the diffusion model in eq. (2.10) if the positron diffusion coefficients are equal for all layers. If not, the continuity of the positron density and the positron flux at the boundaries between two different layers is not warranted. The diffusion problem can still be solved but with the modified matrices and vectors given in Table 2.2.

Note that the positions of the layer boundaries as calculated with model #4 and model #5 can be slightly different due to the different definitions. The only way to reduce this difference is by decreasing the width of the integration intervals.

The program allows the user to fit any model parameter (except the lattice constant, the sample density and the bulk annihilation rate) with a maximum of 5 for the non-linear parameters. Fitting of the positron implantation parameters, however, is only feasible in special cases.

The estimation of the model parameters is accomplished by the use of the least-squares technique. Since the S-parameters and the

parameters describing the probability of Ps formation (f_0 and $f_{0,epi}$) at the surface are linear in the models and the other parameters non-linear, a semi-linear fitting procedure is applied^{34,35}.

Taking into account the semi-linear character of the fitting model, the fitting parameters can be divided into three groups:

1. the linear S-parameters: S for each interval, S_b , S_t , S_s and S_{epi} ,
2. the linear F-parameters: f_0 and $f_{0,epi}$,
3. the non-linear parameters: (effective) diffusion lengths, drift velocities, gaussian profile parameters, layer boundary positions, and the stopping profile parameters.

It should be noted that the linear parameters in 1. and 2. must be treated separately because the linear relaxation extends to $S(E)$ or $F_s(E)$ but not to both simultaneously. The result is that three minimisation procedures are performed independently.

2.3.5 Modelling and fitting results

The VEPFIT program has been tested for artificially obtained data and for measured data. In most cases 15 to 20 intervals were sufficient to achieve the required accuracies in modelling and fitting. The CPU-time on a VAX-8350 amounted to less than 1 second for modelling and from 60 to 300 seconds for fitting. On a PC (personal computer) with a 386 processor and a 387 mathematical coprocessor the compiled program (Microsoft Fortran Compiler Version 4.1) required execution times varying from 10 seconds to 15 minutes depending whether the program was used for modelling or for fitting.

It is impossible to define a general strategy for fitting positron beam data. Usually much is known about the material that has been investigated, e.g. the basic material or the substrate, the type of defects to be expected, the number of deposited layers and the constituent materials, and whether electric fields might be present, all of which may help to set a limit to the number of parameters that have to be fitted. In the following a selection of problems will be presented on which VEPFIT has been tested.

Table 2.4. Fitted values of boundary positions for an embedded defect layer generated with 40 depth intervals.

Number of intervals	Lower boundary (nm)	Upper boundary (nm)
40	10.00 (0.04)	100.0 (0.5)
30	10.19 (0.04)	100.8 (0.5)
20	10.46 (0.04)	103.0 (0.6)
15	10.95 (0.04)	106.4 (0.7)
12	11.76 (0.04)	108.9 (0.7)
10	13.00 (0.05)	126.6 (1.4)
8	17.60 (0.05)	262.1 (8.1)

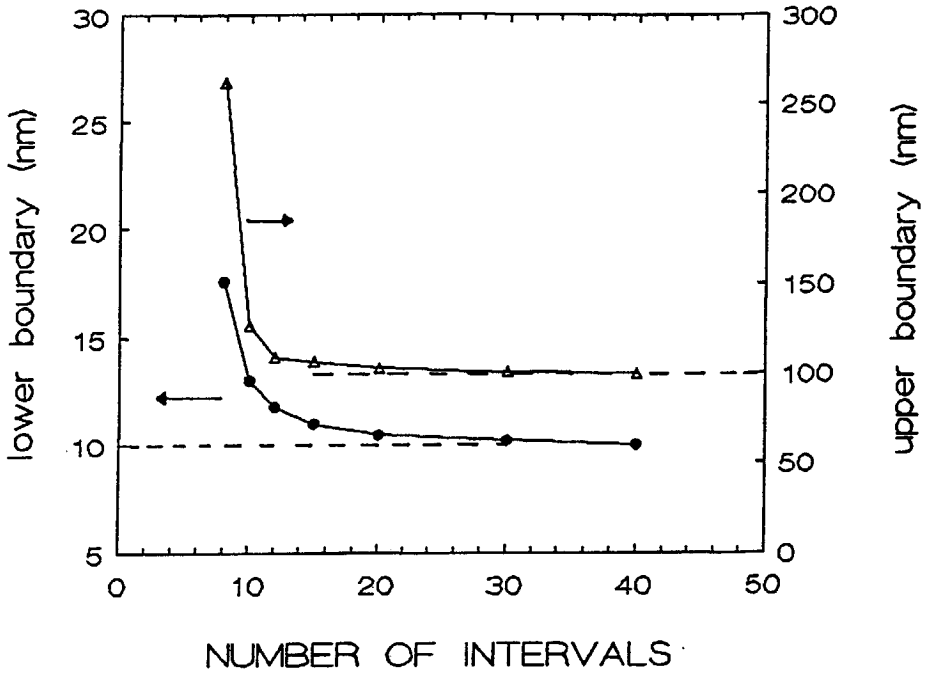


Fig. 2.4. Fitted upper and lower boundary positions *vs.* the number of discretization intervals. The original positions of the upper and lower boundaries were 100 nm and 10 nm, respectively. The artificial S-parameter and Ps-fraction curves have been calculated using model #5 and 40 discretization intervals.

ARTIFICIAL DATA.

Example 1.

As a first example of VEPFIT calculations we have fitted S-parameter and Ps-fraction curves for the case of a layer containing defects. The artificial data have been calculated with model #5 for a zone containing defects ranging from 10 to 100 nm below the surface in a material with $L_+ = 75$ nm and $S_b = 0.46$. In the zone containing the defects the values of $L_{+,eff}$ and S_t were taken 25 nm and 0.47 respectively. It was tested how the fitting of the boundary positions was affected when the number of intervals was reduced from the original number of 40 to 8. In Table 2.4 the fitting results are presented. Fig. 2.4 shows a plot of the fitted upper- and lower-boundary positions *vs.* the number of intervals used. It is demonstrated that the boundary positions in this case are correctly predicted when the number of intervals becomes larger than 15. Note that no statistical spread is introduced in the artificial data.

Example 2.

This example is dealing with a material in which defects are present in a zone stretching from 40 to 140 nm below the surface. The material constants are: $a = 3.14$ Å, $\lambda_b = 8.33$ ns⁻¹, $L_+ = 75$ nm and $L_a = 2$ nm. The effective diffusion length in the zone is taken to be 25 nm.

S- and f_{Ps} -data have been generated with values of the S- and F-parameters given in Table 2.5. The data have been analysed with VEPFIT using model #3 instead of the appropriate model #4, in order to demonstrate the effect of a "wrong" choice of fitting model. The artificial data as well as the fitted curves for the Ps-fraction and the S-parameter *vs.* depth are shown in Figs. 2.5 and 2.6. The results given in Table 2.5 are obtained by the following approaches.

1. Fitting of Ps-fraction data only (mode=3):

This approach gives a correct value for the F-parameter f_0 . The parameter $L_{1/2}$ represents the width of the gaussian profile at half maximum and is related to σ_L by $L_{1/2} = 2\sqrt{2 \ln(2)} \sigma_L$. In Fig. 2.7 the variation of the effective diffusion length with depth is depicted for both the original block profile and the fitted gaussian profile. The fitted minimum value of the diffusion length is

acceptable as compared to the original value. The position of the gaussian, however, is slightly shifted to a lower depth.

2. Fitting of S-data only (mode=2):

The values for the surface, bulk, and defect S-parameters agree almost exactly. The top of the gaussian is positioned not far from the center of the original profile. The minimum in the diffusion length is found to be lower (see Fig. 2.8).

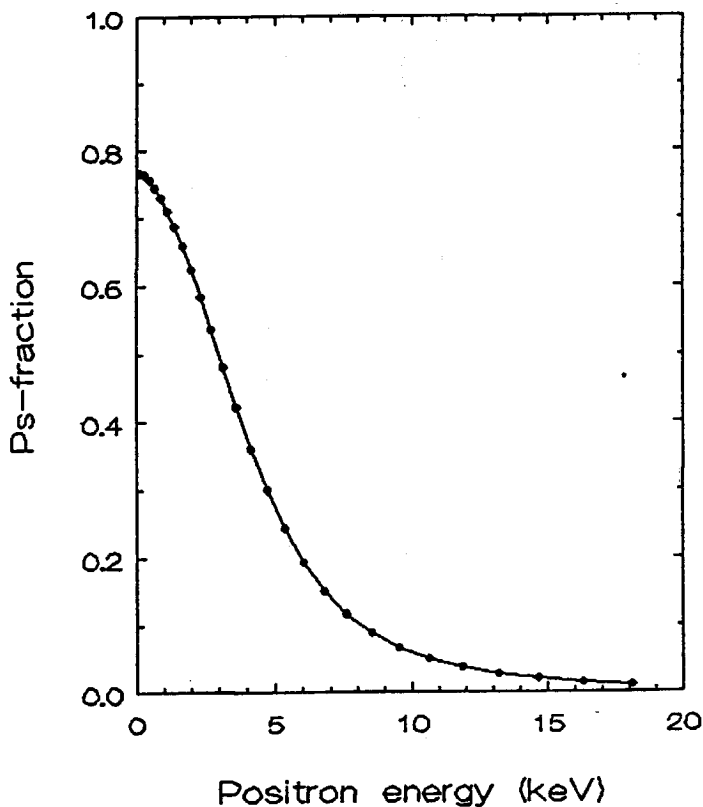


Fig. 2.5. Artificial (•) and fitted (—) Ps-fraction curves *vs.* positron energy. The artificial data are generated with model #4 (block profile) and are fitted with model #3 (gaussian profile).

3. Fitting of both S- and F-data (mode=1):

In this case the values found are almost identical to those obtained with mode 3 (see Fig. 2.9).

It can be concluded that, for the case studied here, still reliable information on the defect distribution can be obtained, in spite of the "wrong" choice of the fitting model.

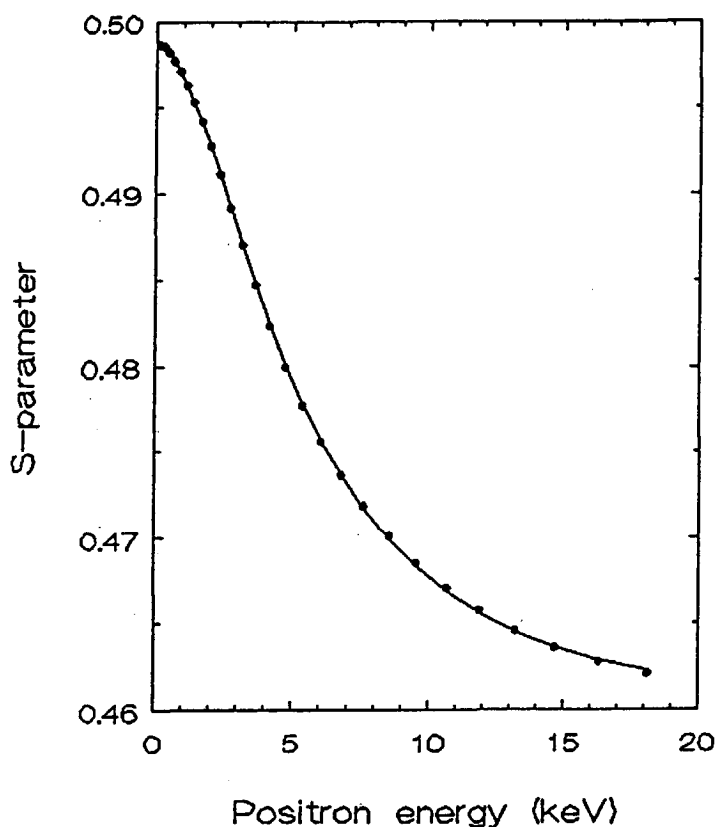


Fig. 2.6. Artificial (•) and fitted (—) S-parameter curves *vs.* positron energy. The artificial data are generated with model #4 (block profile) and are fitted with model #3 (gaussian profile).

Table 2.5. Values of fitted parameters of example 2.

	start value	F fit mode 3	S fit mode 2	F+S fit mode 1
S_b	0.46	—	0.4600 (0.0007)	0.4604 (0.0007)
S_d	0.47	—	0.4701 (0.0007)	0.4703 (0.0008)
S_s	0.50	—	0.5000 (0.0004)	0.4999 (0.0004)
f_0	0.80	0.8005 (0.0003)	—	0.8005 (0.0003)
gaussian:				
$L_{1/2}$	—	43.8 (2.3)	44.3 (42.4)	44.0 (2.3)
z_L	—	77.0 (1.4)	85.5 (7.7)	77.1 (1.4)
$L_{+,eff}$ (min)	—	19.6 (0.3)	13.5 (25.5)	19.6 (0.3)

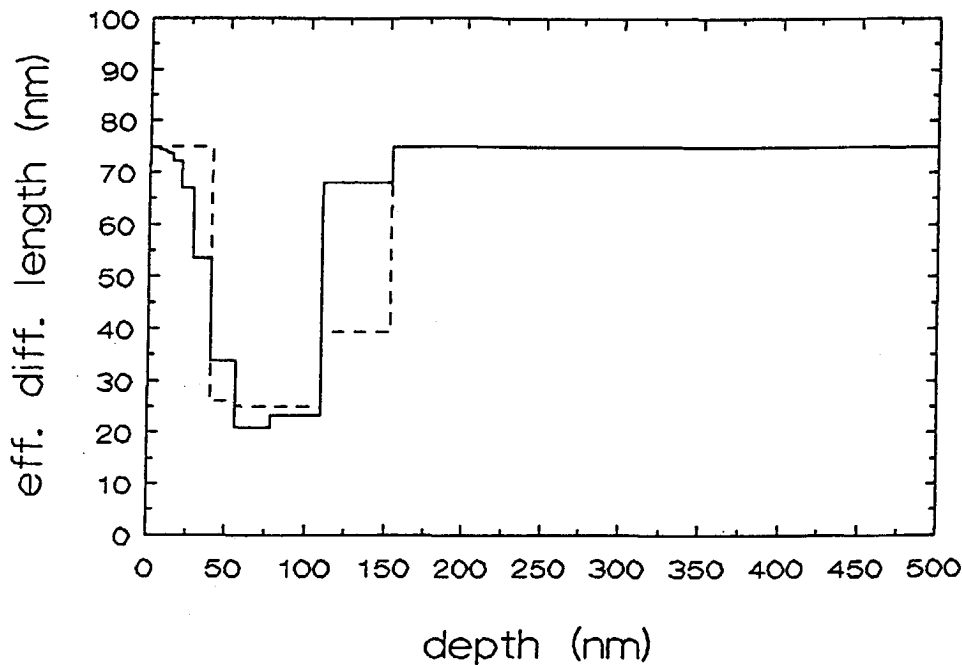


Fig. 2.7. Artificial (---) and fitted (—) effective diffusion lengths vs. depth. The artificial diffusion lengths are generated with model #4 (block profile). The fitted data are obtained by fitting Ps-fraction data only (see Fig. 2.5) using model #3 (gaussian profile).

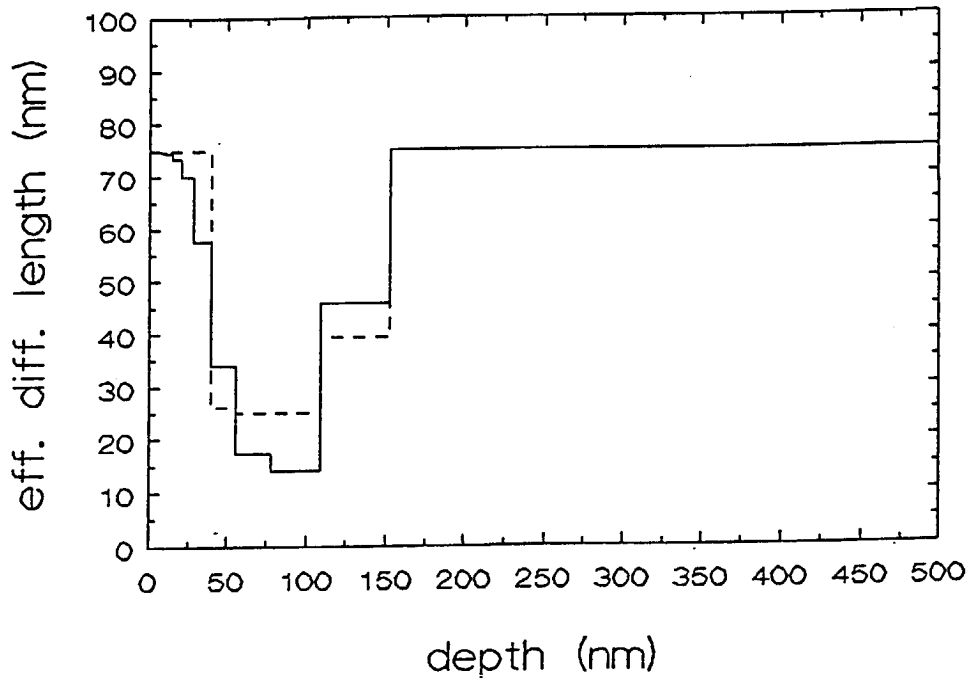


Fig. 2.8. Artificial (---) and fitted (—) effective diffusion lengths *vs.* depth. The artificial diffusion lengths are generated with model #4 (block profile). The fitted data are obtained by fitting S-parameter data only (see Fig. 2.6) using model #3 (gaussian profile).

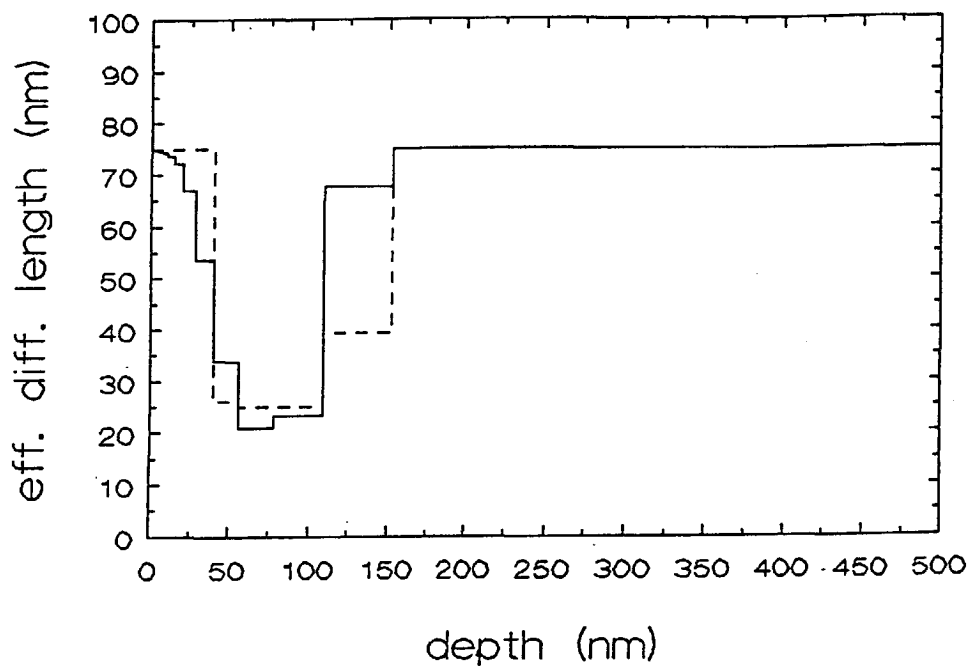


Fig. 2.9. Artificial (---) and fitted (—) effective diffusion lengths *vs* depth. The artificial diffusion lengths are generated with model #4 (block profile). The fitted data are obtained by fitting both S-parameter and Ps-fraction data (see Figs. 2.5 and 2.6) using model #3 (gaussian profile).

Example 3.

S-parameter and Ps-fraction curves have been generated for a semiconducting material in which an electric field is present in a 40 nm thick top layer. The strength of the field was chosen to be 10^7 V/m directed inward the sample. In realistic cases the field strengths may be two orders of magnitude lower. The artificial data and the fitted curves are shown in Figs. 2.10 and 2.11. The curves have been fitted by the following approach. No electric fields are assumed but defects are allowed to be present in a single layer (model #4). The result is

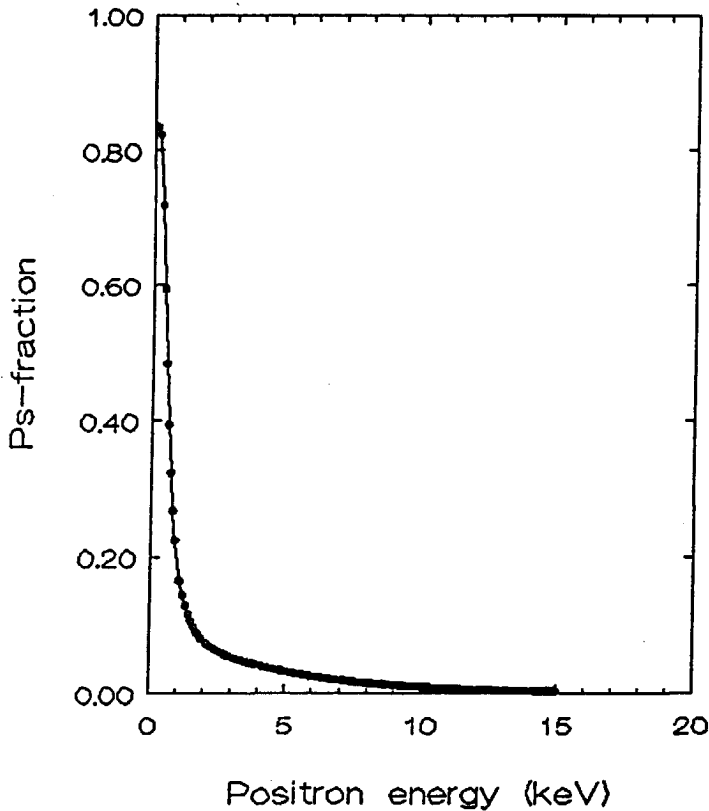


Fig. 2.10. Artificially generated Ps-fraction data (•) for a semiconducting material with an electric field (10^7 V/m) directed inward the sample in a top layer of 40 nm. The curve is the result of a fit to the data using model #4, when electric fields are excluded but a zone containing defects is allowed.

a zone with a strongly reduced diffusion length (from 250 to 10 nm) and with the upper layer boundary shifted towards the surface (see Fig. 2.12). Apparently, effects due to defect trapping can be similar to those due to an inward directed electric field. However, when the electric field is reversed (pointing in the direction of the surface) the effects can never be explained by the presence of defects, as in this case the diffusion length would become larger than the bulk diffusion length and a negative trapping rate would occur.

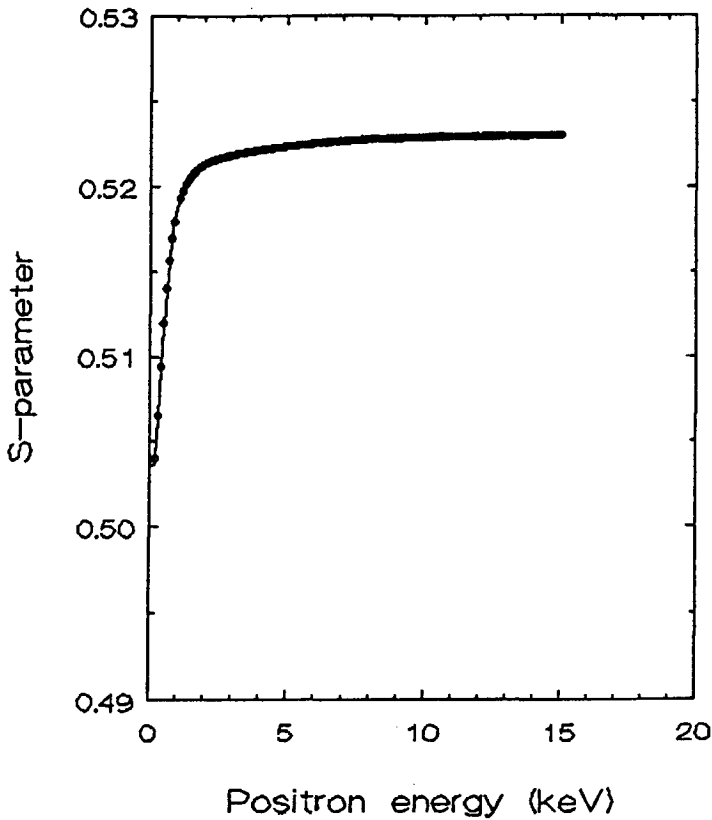


Fig. 2.11. Artificially generated (•) and fitted (—) S-parameter data as a function of the positron incident energy. The data are generated and fitted under the conditions given in Fig. 2.10.

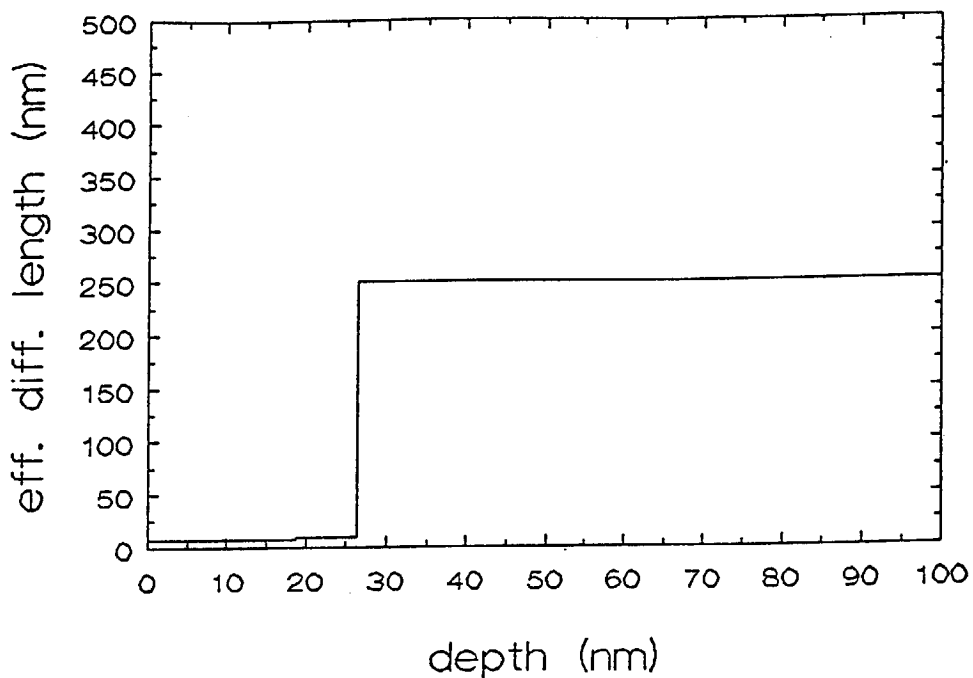


Fig. 2.12. The effective diffusion length *vs.* depth obtained by fitting the artificially generated Ps-fraction and S-parameter data shown in Figs. 2.10 and 2.11. It shows that an electric field pointing inward a material can be represented by a narrower zone with a decreased diffusion length.

EXPERIMENTAL DATA.

Example 4.

As an example of fitting experimental data the analysis of S-parameter and Ps-fraction data measured at a Mo single crystal bombarded with 3 keV helium ions with a dose of $1.0 \times 10^{15} \text{ He}^+ \text{ cm}^{-2}$ will be presented. In a earlier publication³⁶ a Makhov defect profile was hand-adjusted to the data (see also chapter 4). Using the present program, we

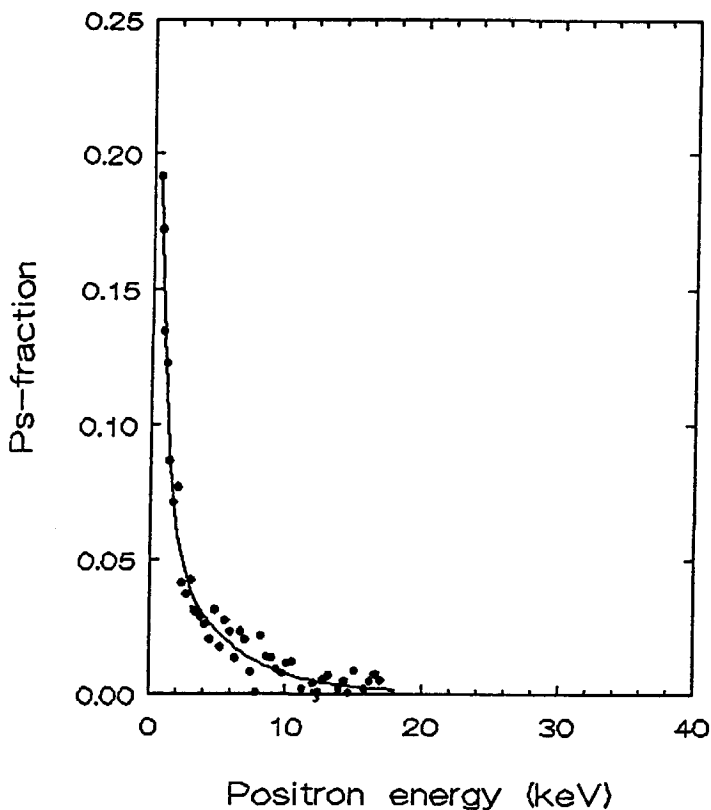


Fig. 2.13. Experimental (•) and fitted (—) values of the Ps- fraction *vs.* positron incident energy for a Mo(100) sample irradiated with 3 keV, $1.0 \times 10^{15} \text{ He}^+/\text{cm}^2$. The curve represents the results of fitting the measured Ps-fraction data and S-parameter data (see Fig. 2.14) using a gaussian defect profile, a block defect profile or a layer structure.

have fitted both a gaussian defect profile, a block profile and a layered profile to the data. The fitted parameters are collected in Table 2.6. The data and fits are shown in Figs. 2.13 and 2.14.

The variation of the effective diffusion length *vs.* depth for the gaussian, block and layered profiles are depicted in Fig. 2.15. Comparison of the results obtained with the different models shows that both the block profile and the layered profile yield a defect distribution extending to a depth of 14 nm. The gaussian profile is wider but the value

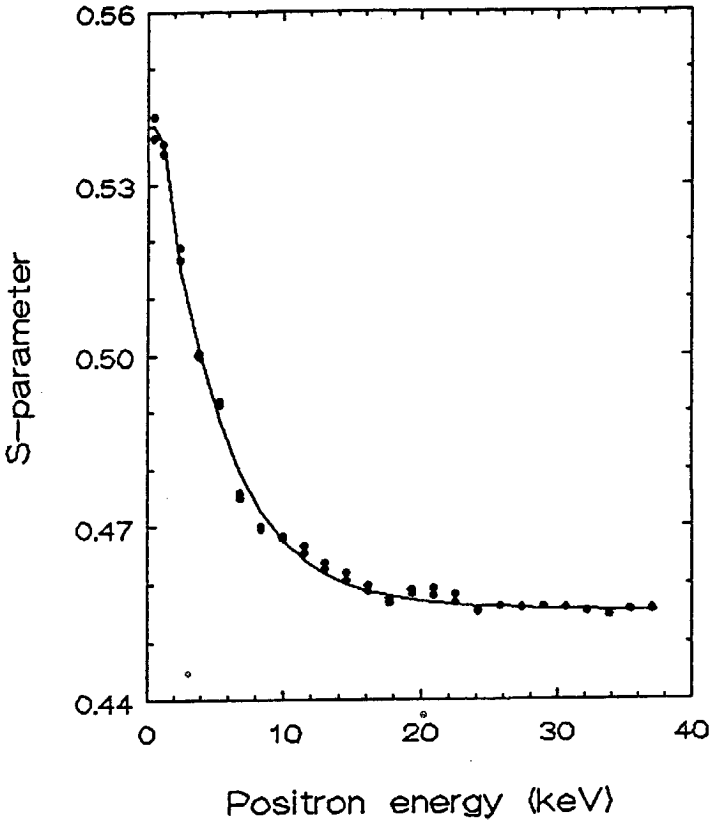


Fig. 2.14. Experimental (•) and fitted (—) values of the S-parameter data *vs.* positron incident energy for a Mo(100) sample irradiated with 3 keV, 1.0×10^{15} He⁺/cm². (See also Fig. 2.13).

for $L_{1/2}$ is comparable to the width of the two other profiles. All three models yield a value for the effective diffusion length of ~ 5 nm in the zone containing the defects.

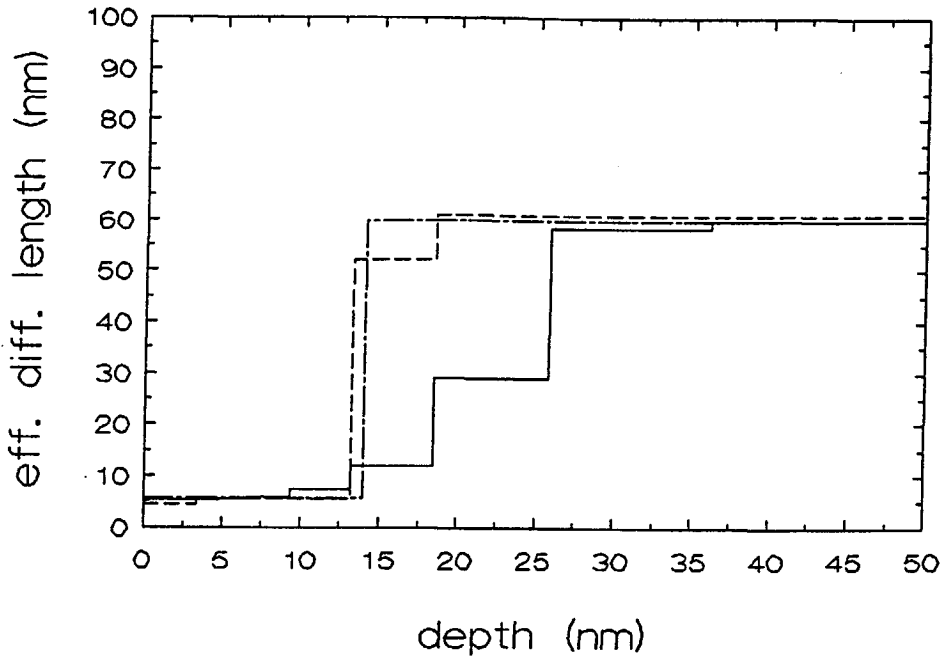


Fig. 2.15. Fitted values of the effective diffusion length *vs.* depth for the Mo(100) sample irradiated with 3 keV, 1.0×10^{15} He⁺/cm². Shown are the results obtained with a gaussian defect profile (solid line), a block defect profile (dashed line) and a layered structure (dot-dashed line).

Table 2.6. Values of fitted parameters of example 4 for the different profiles.

	gaussian profile (model #3)	block profile (model #4)		
S_b	0.4553 (0.0002)	0.4552 (0.0002)		
S_d	0.5061 (0.0007)	0.5093 (0.0007)		
S_s	0.5712 (0.0009)	0.5708 (0.0009)		
f_0	0.22	0.2407 (0.0007)		
		layer	z_l	$L_{+,eff}$
$L_{1/2}$	16.7 (1.6)	1	3.5	4.38 (0.06)
z_L	2.8 (1.1)	2	14.0	5.45 (0.04)
$L_{+,eff}$ (min)	5.22 (0.07)	3	—	60.0

layered profile (model #5)					
		layer	S_l	z_l	$L_{+,eff,l}$
S_s	0.5620	1	0.5450	3.5	5.6 (0.1)
f_0	0.2159 (0.0009)	2	0.5065	14.0	5.84 (0.05)
		3	0.4550	—	60.0 (1.0)

2.3.6 Discussion

The method developed for fast modelling of positron beam interactions with solids appears to perform well. The program VEPFIT based on this method has shown to be capable of fitting a wide variety of positron beam data.

However, in using the program one should be aware of the limitations of the program due to certain assumptions made in the model. These assumptions concern i) a simplified approach of the positron transport in solids, and ii) the branching of positrons into different states at the surface.

It is generally agreed upon that the single-velocity diffusion approach is a good approximation for the description of the transport of thermal positrons when they are slowed down at distances of at least a few mean free path lengths below the surface. This condition is fulfilled by positrons implanted with initial energies of a few keV¹⁶. When positrons slow down in the vicinity of the surface (or in more general in the vicinity of interfaces) diffusion theory no longer strictly applies because i) a considerable fraction of the positrons is not fully thermalized while interacting with the surface or interface, and ii) diffusion theory, even for thermalized positrons, does not apply when distances are of the order of the mean free path length. The latter problem can be circumvented by introducing a modified boundary condition as discussed in section (2.2.4). This approach is well known in neutron transport calculations. In order to check its validity for positrons, transport calculations have been performed with the ANISN-E code³⁷ for a single positron group with different values of the positron mean free path, the diffusion length and the surface reflection coefficient. In most cases the calculated positron flux at the surface boundary agreed within 10% with the one obtained from diffusion calculations (eq. (2.16)). Only for small diffusion lengths (high defect concentrations) the results deviated more strongly.

Effects due to epithermal positrons can in certain cases be accounted for by the treatment suggested by Britton (see section 2.3.3). A study of the positron transport problem, e.g. by Monte Carlo simulations or by multi-group diffusion theory might still be needed in order to correctly describe the effect of epithermal positrons in positron beam

experiments.

The VEPFIT program offers the possibility to include multi-group diffusion theory. The method presented to solve the single-group diffusion problem can be extended to more groups by solving the coupled matrix equations

$$\mathbf{A}^{(k)} \vec{c}^{(k)} = \vec{b}^{(k)} \quad k = 1, \dots, M \quad (2.52)$$

where the superscript k denotes the different energy groups. Group M represents the positrons with thermal energies. Solving the equation starts with $k = 1$ where \vec{b}^1 carries the information on the positron implantation profile for group 1 positrons. For the other groups \vec{b}^k contains the source term corresponding with the positrons that are (energy) down-scattered from group $k - 1$ to k . In future an updated version of VEPFIT will be extended with this option.

The branching of positrons at the surface into positronium (ortho and para), surface trapped positrons, and re-emitted free positrons is not fully taken into account in VEPFIT. An average value S_s and S_{epi} for thermal positrons and epithermal positrons respectively, has been assigned to all positrons that are surface transmitted. Other (experimental) methods will be required to separate the different contributions to S_s .

2.3.7 Conclusion

A novel and fast method has been developed and tested to model the interaction of positron beams with solids and to fit positron beam experimental data. It has been shown that the options incorporated in the computer program VEPFIT can be adequately applied to a variety of depth profiling problems.

References chapter 2

1. A.P. Mills jr., in *Positron Solid State Physics*, Proc. of the 83rd Int. School of Physics 'Enrico Fermi', eds. W. Brandt and A. Dupasquier, (North Holland, Amsterdam, 1983), p.432.
2. R.M. Nieminen and J. Oliva, *Phys. Rev. B* **22**, 2226, (1980).
3. B. Nielsen, K.G. Lynn and Y.C. Chen, *Phys. Rev. Lett.* **57**, 1784, (1986).
4. E.M. Gullikson and A.P. Mills jr., *Phys. Rev. Lett.* **57**, 376, (1986).
5. R. Howell, I.J. Rosenberg and M.J. Fluss, *Phys. Rev. B* **34**, 3069, (1986).
6. A.P. Mills jr., *Phys. Rev. Lett.* **46**, 717, (1981).
7. C.H. Hodges and M.J. Stott, *Phys. Rev. B* **7**, 731, (1973).
8. K.G. Lynn, P.J. Schultz and I.K. McKenzie, *Solid State Comm.* **38**, 473, (1981).
9. P.J. Schultz and K.G. Lynn, *Phys. Rev. B* **26**, 2390, (1982).
10. R.J. Wilson, *Phys. Rev. B* **27**, 6074, (1983).
11. D. Neilson, R.M Nieminen and J. Szymanski, *Phys. Rev. B* **33**, 1567, (1986).
12. D.T. Britton, P.A. Huttunen, J. Makinen, E. Soininen and A. Vehanen, *Phys. Rev. Lett.* **62**, 2413, (1989).
13. T. McMullen and M.J. Stott, *Phys. Rev. B* **34**, 8985, (1986).
14. P.J. Schultz, K.G. Lynn and B. Nielsen, *Phys. Rev. B* **32**, 1369, (1985).
15. B. Bergersen, E. Pajanne, P. Kubica, M.J. Stott and C.H Hodges, *Solid State Comm.* **15**, 1377, (1972).
16. H. Huomo, A. Vehanen, M.B. Bentzon and P. Hautojärvi, *Phys. Rev. B* **25**, 8252, (1987).
17. D.W. Gidley and W.E. Frieze, submitted for publication.

18. C.D. Beling, R.I. Simpson, M. Charlton, F.M. Jacobsen and T.C. Griffith, *Appl. Phys. A* **42**, 411, (1987).
19. D.T. Britton, P.C. Rice-Evans and J.H. Evans, *Phil. Mag. Lett.* **57**, 165, (1988).
20. Y. Kong and K.G. Lynn, to be published.
21. A.P. Mills and R.J. Wilson, *Phys. Rev. A* **26**, 490, (1982).
22. S. Valkealahti and R.M. Nieminen, *Appl. Phys. A* **35**, 51, (1984).
23. A. Vehanen, K. Saarinen, P. Hautojärvi and H. Huomo, *Phys. Rev. B* **35**, 4606, (1987).
24. J.J. Duderstadt and L.J. Hamilton, *Nuclear Reactor Physics*, (Wiley & Sons, New York, 1976).
25. P.J. Schultz and K.G. Lynn, *Rev. Mod. Phys.* **60**, 701, (1988).
26. A. Vehanen, in *Positron Annihilation*, Proc. of the 8th Int. Conf. on Positron Annihilation, eds. L. Dorikens-Vanpraet, M. Dorikens and D. Segers, (World Scientific, Singapore, 1989), p.39.
27. K.G. Lynn, in *Positron Solid State Physics*, Proc. of the 83rd Int. School of Physics 'Enrico Fermi', eds. W. Brandt and A. Dupasquier, (North Holland, Amsterdam, 1983), p.609.
28. K.G. Lynn, D.M. Chen, B. Nielsen and R. Pareja, *Phys. Rev. B* **34**, 1449, (1986).
29. M.D. Bentzon, H. Huomo, A. Vehanen, P. Hautojärvi, J. Lahtinen and M. Hautala, *J. Phys. F* **17**, 1477, (1987).
30. B. Nielsen, A. van Veen and K.G. Lynn, in *Positron Annihilation*, Proc. of the 7th Int. Conf. on Positron Annihilation, eds. P.C. Jain, R. M. Singru and K.P. Gopinathan, (World Scientific, Singapore, 1985), p.836.
31. P.J. Schultz, E. Tandberg, K.G. Lynn and B. Nielsen, *Phys. Rev. Lett.* **61**, 187, (1988).
32. J. de Vries and A. van Veen, to be published in *Comp. Phys. Comm.*
33. W.H. Press, B.P. Flannery S.A. Teukolsky and W.T. Vetterling, *Numerical Recipes*, (Cambridge Univ. Press, 1986).

34. P. Kirkegaard and M. Eldrup, Comp. Phys. Comm. **3**, 240, (1972).
35. P. Kirkegaard and M. Eldrup, Comp. Phys. Comm. **23**, 307, (1981).
36. H. Schut, A. van Veen, K.G. Lynn and B. Nielsen, to be published.
37. NEA, Nuclear Energy Agency Data Bank, Computer Code Library, ANISN-E, CCC 314, (1977).

Chapter 3

The variable energy positron beam facility (VEP)

3.1 Introduction

The variable energy positron beam (VEP) facility, subject of this chapter, has been built at the Interfaculty Reactor Institute of the Delft University of Technology. The VEP project was initiated in 1983 by the group Radiation Damage in Materials of the Reactor Physics Department. The facility was designed and constructed during the period 1984-1986. The positron source (^{22}Na) was installed in March 1987. After a period of testing the facility was officially inaugurated in April 1988.

The motivation to extend the existing techniques used for defect studies with a variable energy positron beam has been twofold. Firstly, the depth regions covered by the THDS (Thermal Helium Desorption Spectrometry) and the conventional PA (Positron Annihilation) techniques do not overlap. With THDS depths up to 100 nm are covered whereas conventional PA covers depths ranging from 10 to 100 microns. This implies that direct comparison of THDS and PA results is difficult. Secondly, both techniques are not capable of providing depth resolved information in a straightforward manner.

A variable energy positron beam offers the possibility to probe defects over a depth ranging from zero to several microns and hence forms a link between THDS and conventional PA. Since in positron beam ex-

periments the energy of the incoming positrons is a known parameter the obtained information can be related to depth. Furthermore, the partial overlap in depth of THDS and positron beam experiments provides a possibility to quantitatively calibrate the latter technique (e.g. the number and type of defects can be well characterized by THDS).

In designing a variable energy positron beam one is faced with questions concerning the choice of the primary positron source, the way of converting the primary fast positrons into slow positrons with well defined energy (moderation), the transport of moderated positrons from the source area to the target and the acceleration to the desired energy. It is without doubt that the final design depends on the requirements set by the type of measurement to be carried out. For example, positron beam surface studies require ultra high vacuum (UHV) conditions whereas bulk defect studies can be performed under non-UHV conditions. Angle resolved measurement of re-emitted or backscattered positrons is only possible in case of electrostatically guided or hybrid positron beam systems. On the other hand magnetically guided systems are favourable when positrons have to be transported over long distances as is the case for reactor based or LINAC based positron beams. The choice of moderation configuration further sets limitations on the type of primary source used. At present the most practical and efficient moderators are negative work function moderators operating in backscatter mode. Positron beams utilising a backscatter geometry require very small and hence intense sources in order to reduce shadowing effects introduced by the presence of the source. Up to now the only type of source meeting this requirement is a ^{58}Co needle source in which the radioactive material is electrodeposited onto a thin ($2\mu\text{m}$) Cu layer evaporated on a W needle¹. The use of the longer lived but larger ^{22}Na sources has become feasible with the development of thin film metallic transmission moderators.

Taking into account these considerations and bearing in mind the primary purpose of the Delft variable positron beam facility we have come to a beam design which is based on:

- the use of ^{22}Na as primary positron source, combined with
- transmission moderation of fast positrons, and

- magnetic positron transport.

The following section describes the design of the Delft variable energy positron beam. It is divided into eight subsections containing a general description, a description of the source storage and transfer area, the source and moderator high voltage area, a description of the beam line including the positron energy filter, the accelerator stage, the sample chamber, the photon detection system and finally the control and signal processing.

3.2 Design of the VEP

3.2.1 General design

In Fig. 3.1 the overall design of the VEP apparatus is shown schematically and in Fig. 3.2 a 3-dimensional view is depicted. In Fig. 3.1. the following interconnected parts are indicated:

- a source storage and transfer system (A),
- a source and moderator high voltage area (B),
- a bent section used for positron energy filtering and beam manipulation (C),
- an acceleration stage and beam section (D) and
- the sample chamber and photon detection area (E).

With the source introduction system a 25 mCi ^{22}Na source (Amersham, U.K.) can be positioned in the moderator vacuum chamber. The positrons emitted by the source are transmission moderated by a 8 μm thick tungsten polycrystalline moderation foil free of pinholes (Highways International). The moderated positrons that are re-emitted in forward direction are pre-accelerated to an energy of 115 eV and subsequently transported from the source area to the sample chamber by a 10 mT axial static magnetic field. This field is produced by 14 co-axial solenoids positioned according to a so-called Helmholtz configuration producing an axial magnetic field with a high degree of homogeneity.

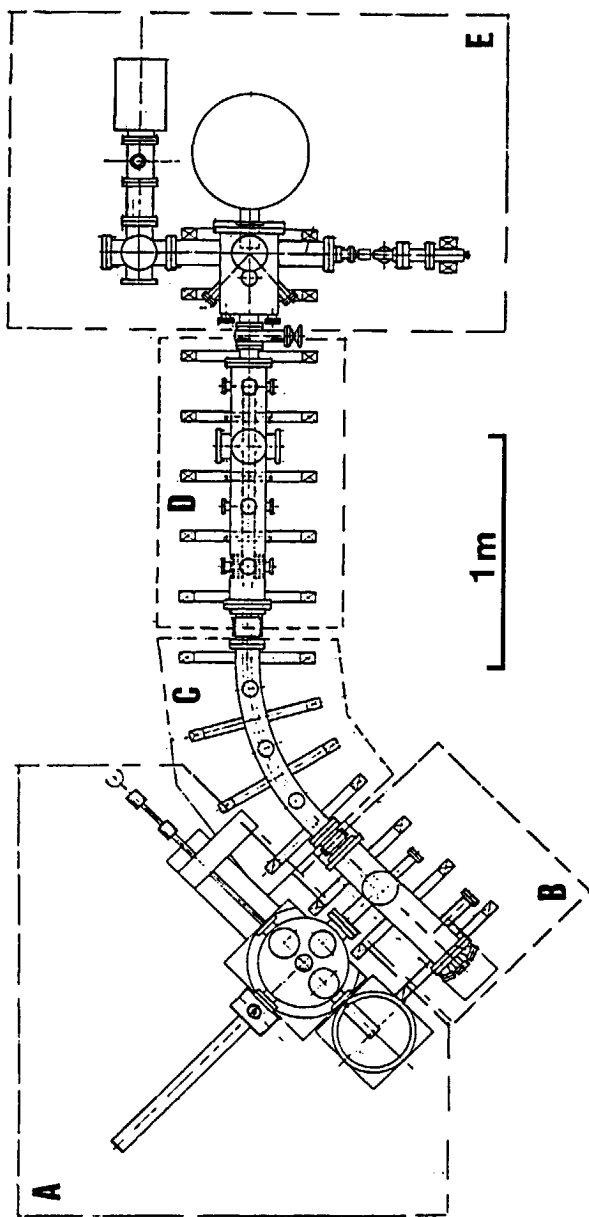


Fig. 3.1. Schematic drawing of the VEP apparatus. The following sections are indicated: a source storage and transfer section (A), the source and modulator high voltage area (B), a bent section used for positron energy filtering and beam manipulation (C), an accelerator and beam line section (D) and the sample chamber and photon detection area (E).

After moderation the positrons are injected into the bent section with a 1 m radius of curvature. This section is composed of an outer vacuum tube (100 mm inner diameter (ID)) and an inner electrically isolated tube (Inconel, 40 mm ID). The bent section has been incorporated for two reasons. Firstly, it acts as a positron energy filter, by which fast moving positrons can be excluded from the positron beam. Secondly, the curved section provides a possibility to prevent direct line-of-sight between the source area and the photon detector positioned at the end of the positron beam.

After passing the curved section the positrons enter the accelerator stage. In this section positrons are accelerated to their final energy. The maximum attainable positron energy is 30 keV. Acceleration of the positrons is achieved by applying high voltage (HV) (Heinzinger 40000-1) to the source and moderator, the curved inner beam tube and the first accelerator plate of the accelerator.

Upon acceleration the positrons are further guided to the sample chamber where they, after having passed a 10 mm diameter diaphragm, finally hit the sample.

The sample chamber, which can be closed off from the rest of the vacuum system by a Viton sealed 60 mm ID valve, is equipped with a mass and energy analyzed gas ion source used for defect creation in the sample and sputter cleaning of the sample surface. The sample itself can be heated to temperatures up to 1500 K by electron bombardment on the rear side of the sample.

With exception of the positron source storage vessel, all parts meet the requirements set for operation under UHV conditions. The vacuum vessels of the source introduction system, the main source and moderation chamber and the curved section have been constructed by the workshop of the Faculty of Applied Physics of the Delft University. The other compartments (beam line vessels and sample chamber) have been made by Vacuum Generators, East-Sussex, U.K.. Care was taken to use only non-magnetic construction materials in order to prevent distortions of the axial magnetic field.

In the whole system vacuum is maintained by several triode iongetter pumps with capacities varying from 25 to 200 l/s. Pumping the system from atmospheric pressure to 10^{-5} Pa is done with a turbomolecular pump in combination with a rotary roughing pump. A pressure of 10^{-6}

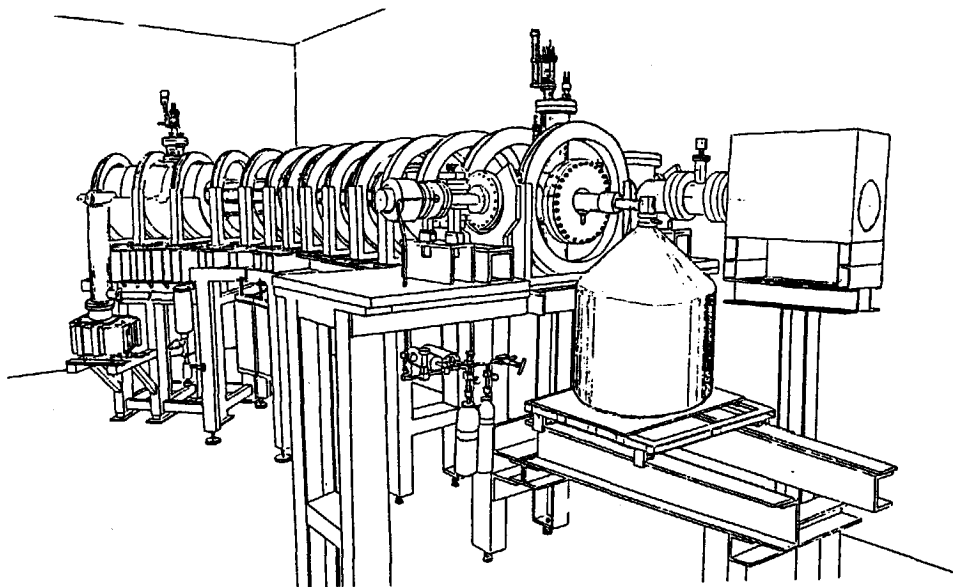


Fig. 3.2. A 3-dimensional view of the VEP apparatus
(drawing by K.J. Roos).

Pa is reached in the source chamber at the rear end of the system. After closing the valve connecting the sample chamber with the beam line the pressure in the sample chamber drops to 10^{-7} Pa. The sample chamber can be baked separately after every sample change operation.

3.2.2 Source storage and source introduction

Fig. 3.3 shows the schematics of the source storage and introduction system. It can be divided into 4 parts:

- a transport and storage vessel (SV),
- a source transfer vessel (TV),
- a transfer device (TD1) for the transfer of the source from the storage vessel to the transfer vessel, and
- a transfer device (TD2) for the transfer of the source from the transfer vessel to the main source chamber .

The storage vessel is used for transportation and long term storage of the positron source. The source is located at the center of the vessel and is shielded by a 11 cm thick lead wall. Part of the lead shielding can be pneumatically lifted in order to remove the source from the storage vessel to the transfer vessel. Removal of the source is done with a specially designed transfer device equipped with bayonet clamps clinging onto a ring supporting the positron source.

The transfer vessel basically consists of two crossed horizontal UHV tubes with inner dimensions of 38 mm. The tubes are placed in a lead container with a diameter of 38 cm and a height of 41 cm. After retracting the source with TD1 into the transfer vessel, transfer device TD2 (Vacuum Generators, LRP 600) is brought into position and the source plus supporting ring can be plugged into a source holder mounted on TD2. This manipulation can be followed by looking via mirrors through a viewing port positioned above the crossing point of the UHV tubes. The source can be transferred to its final position by driving TD2 in the direction of the source chamber. The transfer vessel is provided with an additional copper shielding plug which can be dropped pneumatically into the tube connecting the transfer vessel with the

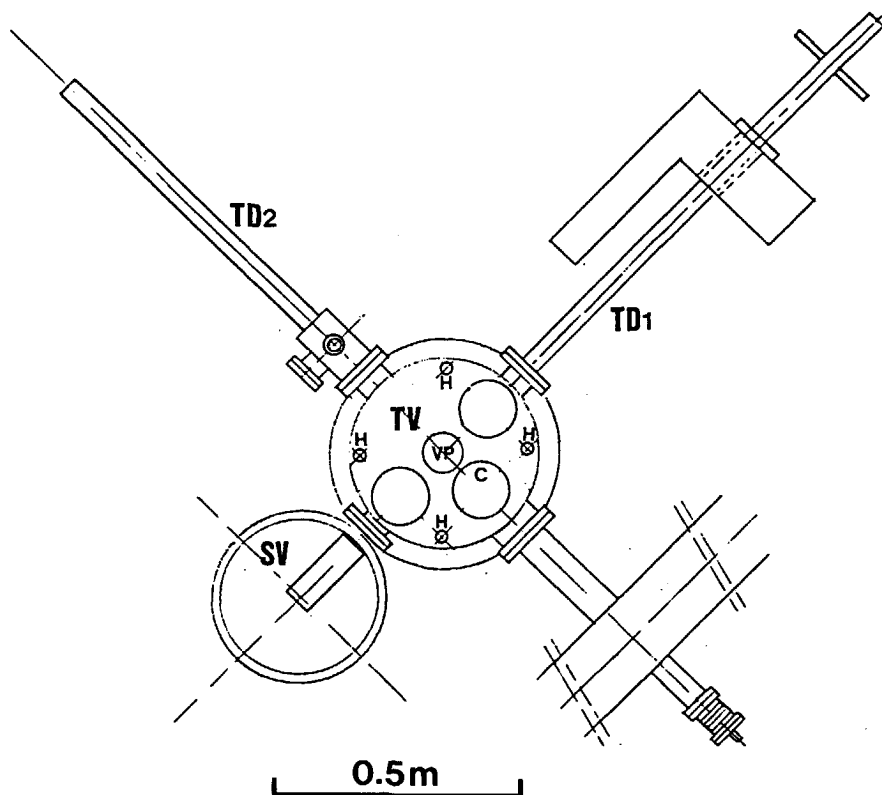


Fig. 3.3. Schematic drawing of the source storage and transfer system. The following components are indicated: a shielding vessel used for transport and long term storage of the positron source (SV), a shielded source transfer vessel (TV) and two transfer devices (TD1) and (TD2). The transfer vessel is provided with a viewing port (VP) and a port (C) through which a copper shielding plug can be lowered. The positions of the resistor heater elements are denoted by (H).

source chamber. Note that when the source is in position it remains connected to the transfer device. The source is electrically isolated from the transfer device by a ceramic insulator inserted between the source holder and a copper radiation shielding plug attached to the transfer device. After having placed the source in its final position the transfer device TD1 is disconnected from the vacuum system and the tubes are closed off with flanges. Pumping of the vessel is done with a 25 l/s ion getter pump (Perkin and Elmer) connected to one of the ports of TD2. Baking of the transfer vessel can be done with 4 resistor heater elements which are placed in the lead shielding.

3.2.3 Source and moderator area

In Figs. 3.4 and 3.5 horizontal and vertical cross-sections of the source and moderator chamber are shown. Fig. 3.4 shows the bare vacuum vessel and in Fig. 3.5 the interior is shown. The source chamber is basically a 150 mm ID, 600 mm long vacuum tube (A) provided with three horizontal and one vertical side tubes.

Through the side tube B (60 mm ID) connected to the transfer vessel the positron source enters the source chamber. Opposite to this tube a smaller (39 mm ID) tube (C) equipped with a HV feedthrough is located. The electrode of this feedthrough has been extended so that it makes contact with the source holder. A third horizontal side tube (D, 60 mm ID) is located at the rear end of the vessel and is connected via a metal sealed valve to a 200 l/s Riber triode ion getter pump. The rear end of the main tube is closed off with a (200 mm OD) UHV flange (E) furnished with several smaller (two 70 mm OD and three 34 mm OD) UHV flanges. The front end of the tube is connected to the bent section of the vacuum system via an adapter flange and a 100 mm ID bellows (F).

The position of the vertical side tube is shown in Fig. 3.5. It consists of a 100 mm ID UHV tube located above the position of the source. On top of this tube a ceramic insulator (G, 100 mm ID) is placed which electrically isolates a moderator manipulation system (H) from the main vessel. With the manipulator the tungsten moderator foil can be moved in front of the source (minimum source-moderator distance 1 mm) or to a position where the moderator foil can be irradiated

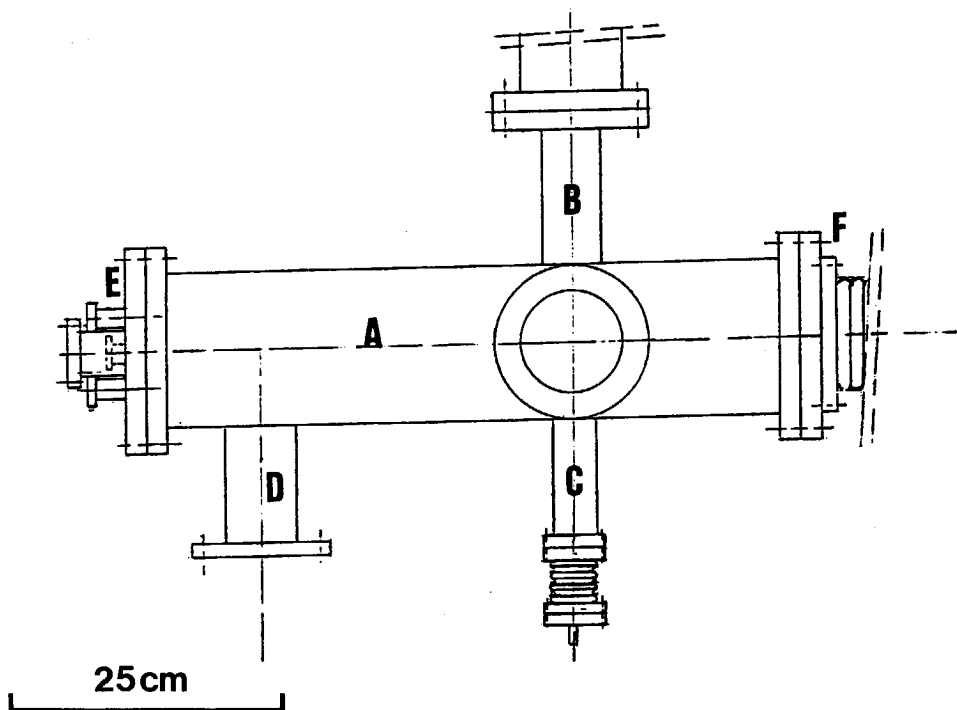


Fig. 3.4. A horizontal cross-section of the bare source and moderator chamber (A). Side tubes B, C and D are connected to the transfer vessel, a high voltage feedthrough and a 200 l/s Riber ion getter pump, respectively. At the rear end the chamber is closed off by a 200 mm OD flange (E). The front side is connected to the bent section through a bellows (F).

with electrons emerging from an electron gun (I) attached to the rear flange. Besides this vertical movement the foil can be tilted away from the source. This is done when the source is brought in to position or retracted from the source chamber.

A rod carrying a grid system (J) used for the extraction and pre-acceleration of moderated positrons is fixed to the manipulator base flange. The grid system is composed of three 98 % transmission Mo meshes (40 mm in diameter) spotwelded onto three electrically isolated supporting rings. It is possible to apply extraction voltages to the grids separately but in practice it turned out that applying a voltage of -115 V to the three grids gave the highest slow positron yield.

The manipulator is further equipped with two viewing ports used for optically monitoring the manipulation of the moderator foil and feedthroughs used for applying extraction voltages. A flange placed on top of the manipulator is provided with feedthroughs which are connected to a WRe3%–WRe25% thermocouple attached to the moderator foil.

Shielding of the positron source is achieved in two ways. Outside the vacuum a lead ring (K) with a thickness of 11 cm surrounds the source vessel. Inside the vacuum system two baked massive copper cylinders (L1 and L2) are placed on either side of the source. These cylinders rest on an annular Al_2O_3 insulator (M) and are electrically connected to the source (L1) or to the grid system (L2). The copper cylinder at the rear end is provided with a channel to allow electron irradiation of the moderator foil. Heating of the foil can be monitored optically through a channel in the copper cylinder lined up with a viewing port (N) attached to the rear flange. The small central channel can be used for lining-up the system. The copper cylinder in front of the source is provided with a central channel (40 mm diameter) and is connected to the isolated inner tube of the curved section.

A simple gas inlet system is connected to the rear flange of the source chamber. Gases, e.g. O_2 and H_2 used for treatment of the moderator foil can be introduced through a needle valve. The source chamber can be baked by means of a heater ribbon wrapped around the vacuum vessel.

In Fig. 3.6 the details of the positron source and the source holder are shown. It consists of a stainless steel frame connected via an insulat-

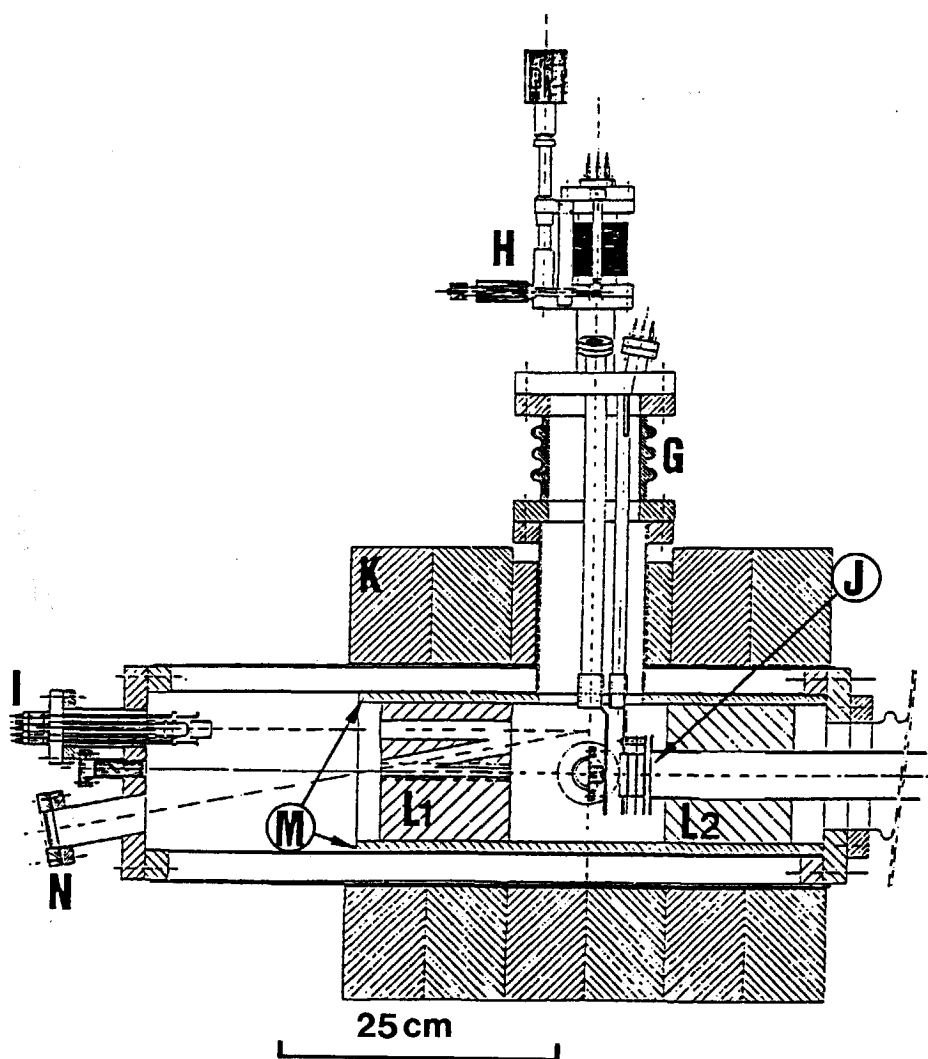


Fig. 3.5. Detailed schematic of the source and moderator section. The figure shows the source holder (central in the lead shielding (K)). Indicated are a 100 mm diameter ceramic insulator (G) on top of which the moderator manipulator (H) is placed. Attached to the rear flange are an electron gun (I) and a viewing port (N). L1 and L2 are two copper shielding cylinders surrounded by an Al₂O₃ insulator (M). The extraction grids are denoted by (J).

ing part and copper shielding plug to the top end of the source transfer device (TD2). The other end of the frame is shaped in such a way that it fits to the extended electrode of the high voltage feedthrough.

The ^{22}Na radioactive material (chemical form NaCl) is deposited on a platinum disk which is sealed by two $5\text{ }\mu\text{m}$ thick titanium foils. These foils are laser welded onto a Ti holder (Amersham, X-1055 capsule). The source is connected to a supporting disk equipped with bayonet clamps and can be plugged into the frame. According to the specifications given by the manufacturer the source initially emitted 2×10^8 positrons per second (2π geometry and including self absorption).

Fig. 3.7 shows the details of the moderator assembly. The moderator foil (6.5 mm diameter) is spotwelded onto a tungsten supporting ring which can be fixed to a disk shaped frame. This frame is attached to the rod connected to the moderator manipulator. In order to measure the temperature of the moderator foil during annealing a $\text{WRe3\%}-\text{WRe25\%}$ thermocouple is attached to the edge of the foil. The moderator foil covers the area of the positron source.

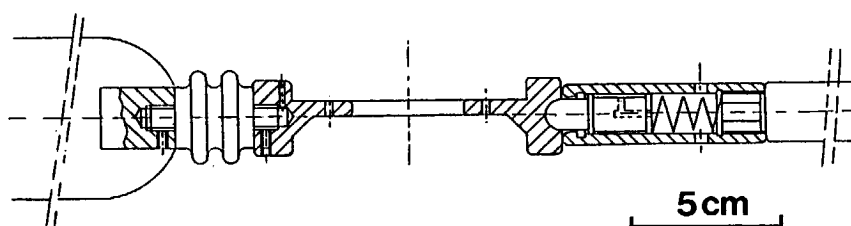


Fig. 3.6. Drawing of the source holder. The holder is connected to the transfer device via an insulator and a copper shielding plug. Also shown on the right is the extended electrode of the high voltage feedthrough. The positron source is plugged into the center of the frame.

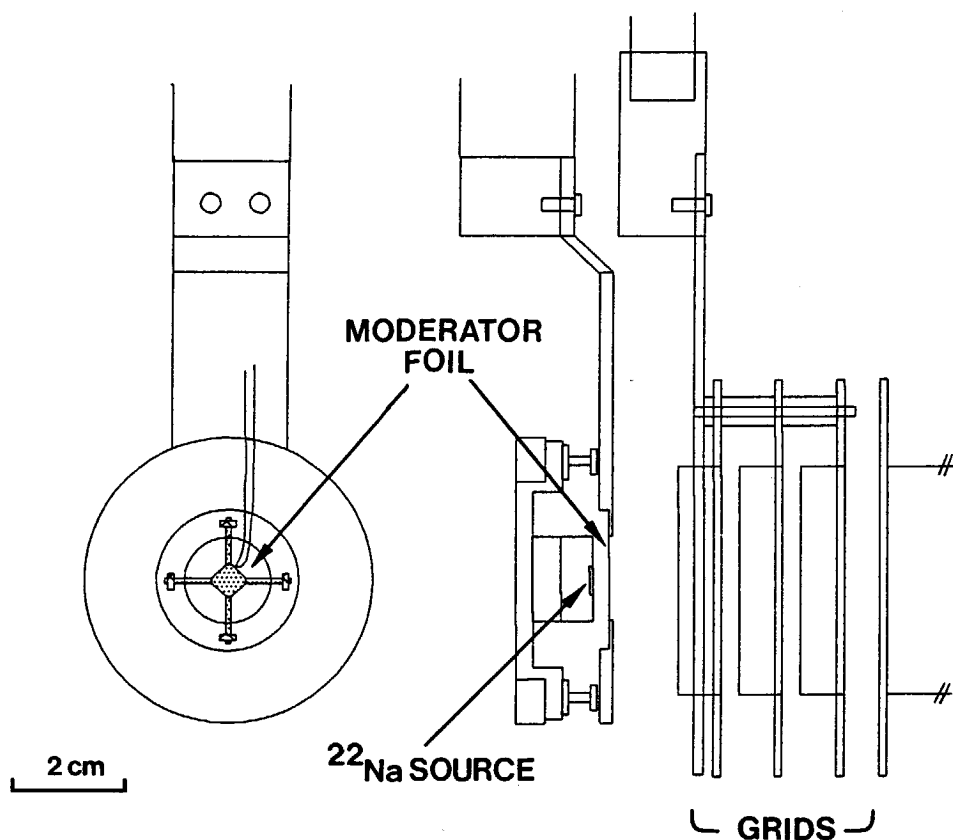


Fig. 3.7. Details of the source/moderator configuration. The left side of the figure shows the $8\text{ }\mu\text{m}$ thick poly-crystalline W foil spotwelded onto a tungsten supporting ring. Attached to the edge of the foil is a WRe3%–WRe25% thermocouple. On the right side the position of the moderator with regard to the position of the source and the extraction grids is shown.

3.2.4 Beam transport and energy filter

As already mentioned in the general description of the apparatus the moderated positrons are transported from the source area to the sample chamber by means of a 10 mT axial magnetic field. This field is produced by 14 co-axial solenoids placed at distances of half the coil diameter. The inner diameter of the aluminum coils is 52 cm and the width of the coils is 50 mm. The copper wire used (500 windings) has a rectangular cross section ($1.0 \times 2.5 \text{ mm}^2$) in order to prevent excessive heating.

In the curved section of the beam line (curvature radius 1 m, curvature angle 45°) the positrons gain a drift velocity which is to first order approximation equal to²

$$|\vec{v}_D| = 2 \frac{E}{RB} \quad (3.1)$$

where \vec{v}_D is the drift velocity (m/s), E is the positron transport energy (eV), R is the radius of curvature (m) and B is the magnetic field strength (T). The direction of \vec{v}_D is perpendicular to the plane of curvature.

In order to compensate for the energy dependent drift a pair of external coils is installed in the curved section. These coils are placed in such a way that an extra magnetic field, \vec{B}_c , is produced at the center of the beam line perpendicular to the plane of curvature (see Fig. 3.8). The Lorentz force $\vec{F}_L = e(\vec{v}_{//} \times \vec{B}_c)$ acting on the positron is always perpendicular to the main magnetic field, \vec{B} , and causes a drift velocity \vec{v}_c proportional to

$$\vec{v}_c = (\vec{v}_{//} \times \vec{B}_c) \times \vec{B} \quad (3.2)$$

with $\vec{v}_{//}$ the velocity of positrons parallel to \vec{B} . By varying the current through the correction coils the strength of the correcting magnetic field can be adjusted to allow transmission of pre-accelerated moderated positrons only.

Between the source chamber and the curved section an additional set of beam correction coils are positioned. The coils produce a magnetic field in the plane of curvature and enable the correction of the horizontal position of the positron beam.

The current through the main solenoids is supplied by five current stabilized power supplies (Delta Electronica, SM6020). The solenoids

are coupled in three sets of four adjacent solenoids. The current through the two last (down stream) solenoids can be adjusted separately. By increasing the current through these solenoids to 10 A the diameter of the positron beam can be decreased to ~ 10 mm. Increasing the current has the unwanted effect of heating the coils to a temperature well above 100°C measured at the outside of the coil. In order to prevent this excessive heating the last two coils are water cooled.

Inside the curved main vacuum tube an Inconel flight tube is positioned. It has an inner diameter of 40 mm and is electrically isolated from the main tube by 5 circularly shaped Al_2O_3 spacers. This tube links the high voltage source area with the accelerator stage. High voltage is supplied through one of the side ports of the main vacuum tube. This section of the beam line is pumped by two 25 l/s (Perkin and Elmer) ion getter pumps.

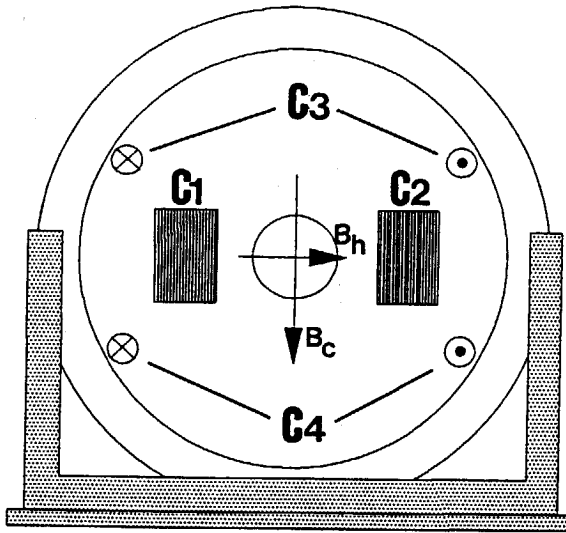


Fig. 3.8. Positions of the beam correction coils at the entrance of the bent section. C1 and C2 are coils producing a magnetic field, B_h , used for the correction of the horizontal position of the beam. The coils C3 and C4 used for compensation of the positron drift velocity are placed inside the main solenoids. The magnetic field produced by these coils is indicated by B_c .

3.2.5 Accelerator stage

In Fig. 3.9 a schematic drawing of the accelerator is shown. It is positioned in a vacuum chamber which is connected via a bellows to the curved section of the beam line.

The accelerator is composed of 11 stacked circular plates (vac-chromium alloy, diameter 80 mm) with a central hole of 40 mm in diameter. The edges of the holes are rounded off to obtain a uniform electric field between the plates. The plates are separated by Al_2O_3 insulating tubes. The distance between two adjacent parallel plates is 10 mm. The first plate is connected to the electrode of a high voltage feedthrough; the last three plates are connected to feedthroughs located at one of the ports of the vacuum chamber. The accelerator plates are internally connected by ten $\text{G}\Omega$ resistors. These resistors are made of Al_2O_3 strips on which a poorly conducting material is deposited. On top of the last plate a cylindrical shaped shield is spotwelded used for screening of the electric field produced by the electrode of the high voltage feedthrough. The stacked plates are mounted on a circular base-plate which can be attached to a flange connecting the vacuum chamber to the bellows.

3.2.6 Sample chamber

The design of the sample chamber and its interior is shown in Figs. 3.10 and 3.11, respectively. The sample chamber is composed of a 250 mm ID, 390 mm long vacuum vessel with two horizontally positioned side tubes of 150 mm ID and two vertically positioned side tubes of 100 mm ID. The sample chamber is connected to the beam line via Viton sealed valve.

One of the horizontal side tubes is connected to a section containing the vacuum pumps. These are a turbomolecular pump (Leybold, 150 l/s) in combination with a rotary rough pumping unit (Leybold, PT 150/4) and a 200 l/s Varian triode ion getter pump. Both vacuum pumps can be closed off from the system by valves. The pressure in the sample chamber is measured with a bare ionization gauge.

The other horizontal tube is connected to a gas ion source. This ion source is of an axial ionizer type with a magnetic field around the ionization chamber. It is a modified version of an ion gun designed by

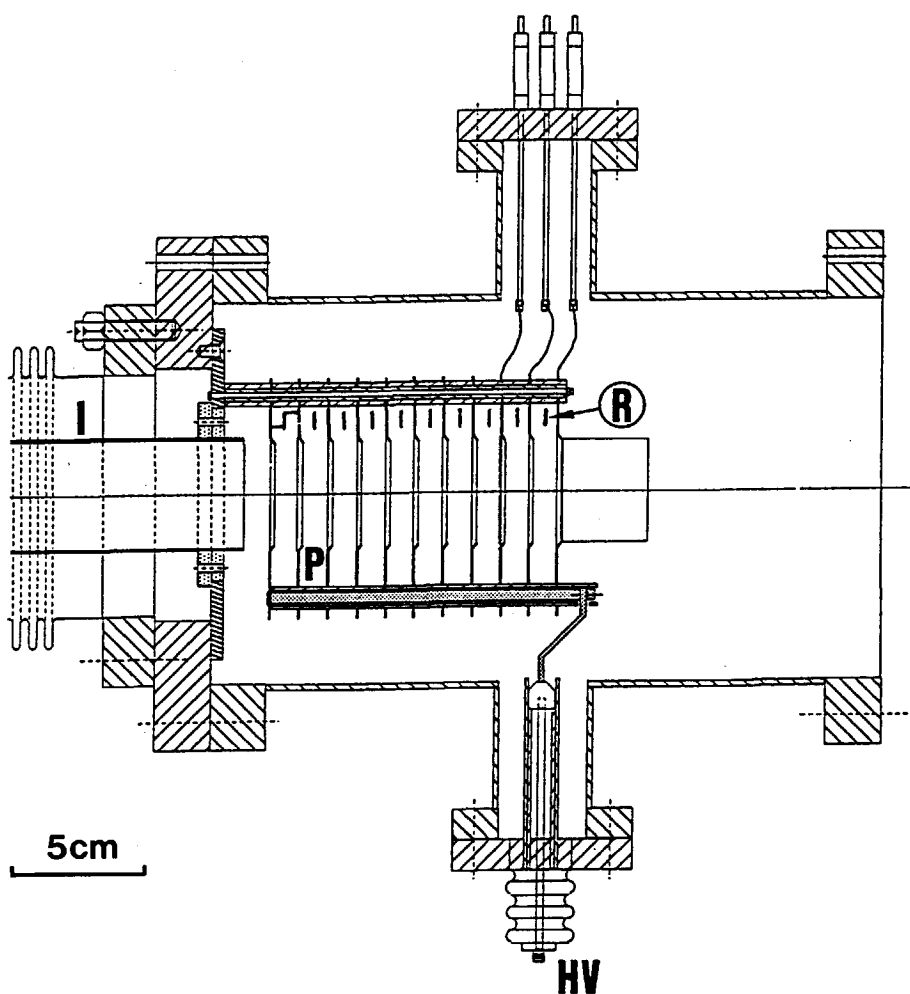


Fig. 3.9. Details of the accelerator. The figure shows 11 accelerator plates (P) internally connected by ten $G\Omega$ resistors (R). The first plate is connected to the electrode of a high voltage (HV) feedthrough. The positron beam enters the accelerator from the left through an electrically isolated Inconel tube (I).

Van Veen³. The gun is equipped with a Wien filter which acts as an ion mass filter, since all ions emerging from the ion source have the same kinetic energy. The ion source is used for defect creation below the sample surface or sputter cleaning of the surface. Gases, e.g. He, Ar, H₂ and O₂, enter the ion source via a simple gas inlet system (not shown in the drawing).

The rear end of the vessel is closed off with a flange (300 mm OD) provided with a cylindrically shaped well pointing inward the vessel. The bottom of the well is at a distance of 10 mm from the position of the sample. A thin tantalum heating shield can be attached to the vacuum side of the well in order to prevent heating of the photon detector mounted in the well.

The vertical tube pointing upward is used for installing the sample manipulator (see Fig. 3.11). Depending on the size of the samples up to a maximum of 5 samples can be attached to a sample holder which is connected to a linear motion device (VG LMT-100). In situ heating of a sample is possible by bombardment with keV electrons supplied by a (thoriated) W filament positioned behind the sample. The temperature of the sample is measured with W/Re or Chromel/Alumel thermocouples. A second sample manipulator equipped with a rotary motion device (VG RD-91) is available. This manipulator is used when samples have to be positioned in the ion beam. This manipulator, however, allows only one sample to be installed.

In case of studying relatively small samples (minimum allowed diameter 8 mm), a 80 mm long, 8 mm bore, copper beam limiter can be positioned in front of the samples. The outer diameter of the limiter is 22 mm. Without the use of the limiter positrons may pass the sample and annihilate at the detector well which is closer to the sensitive area of the detector than the sample. This results in a substantial contribution to the photon energy spectrum of unwanted annihilation photons. By lowering the limiter, part of the beam is intercepted at a distance further away from the detector. In addition, the high density of the limiter material ensures efficient shielding of the photons which are produced when the beam hits the limiter.

At the entrance of the sample chamber a grid is located. To this grid positive or negative voltages can be applied. At positive grid voltages (typically 50 V) positrons re-emitted by the sample are forced to return

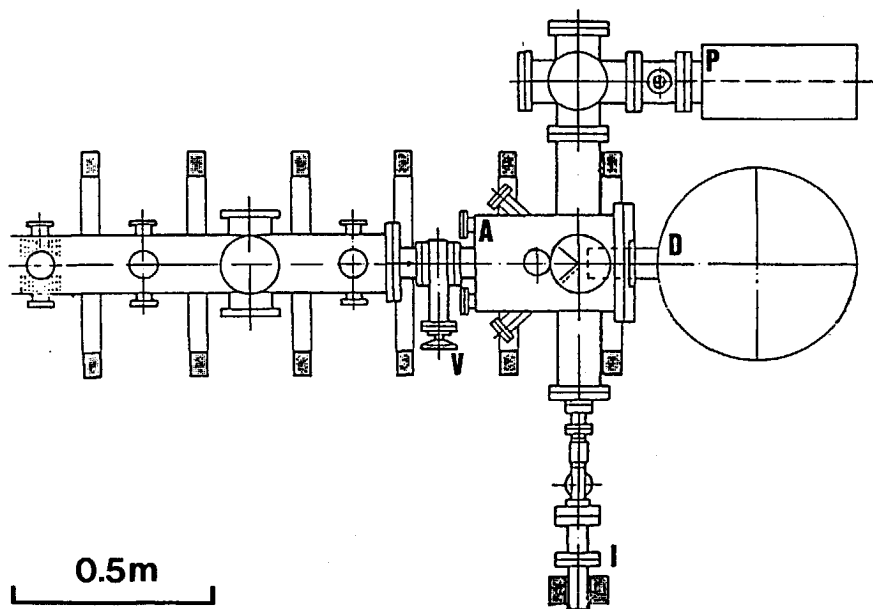


Fig. 3.10. Schematic drawing of the target and detector area. The sample chamber (A) is connected to the beam line through a Viton sealed valve (V). The ion source providing mass and energy analysed gas ions (1 - 5 keV) is indicated by (I). (P) is a 200 l/s Varian ion getter pump. The photon sensitive part of the Ge solid state detector (D) is mounted in the well of the 300 mm OD rear flange of the sample chamber.

to the sample. At a negative grid voltage the re-emitted positrons are removed from the sample and detector region. By measuring Ps-fraction curves under these two experimental conditions information can be obtained on the branching of positrons at surfaces (see also chapter 4).

3.2.7 Photon detection system

The photon detection system used for Doppler broadening and Ps-fraction measurements consists of an intrinsic Ge solid state detector (EG&G Ortec, GMX 20-195) with a measured resolution of 2.1 keV at 1.33 MeV and a relative efficiency of 25 %. Preamplifier pulses are fed into a main amplifier (EG&G Ortec, 672) connected to a 100 MHz ADC (Tracor Northern, TN 1242) and a ratemeter (EG&G Ortec, 449). The ADC output is accumulated in a CAMAC spectrum buffer station containing 4096 channels attached to a PDP 11/44 computer.

Doppler broadening measurements require long term stability of the spectrometer system. Stability is obtained with a two point digital stabilizer which corrects for changes in offset and gain of the spectrometer system. The offset is stabilized on the ^{57}Co 122 keV peak, while the gain is stabilized on the 511 keV peak. In Fig. 3.12 a block scheme of the spectrometer system is shown.

The photon sensitive part of the detector is mounted in the well of the rear flange of the sample chamber and is surrounded by an annular water cooled lead shield.

3.2.8 Control and signal processing

In Doppler broadening and Ps-fraction depth profiling experiments annihilation photon spectra are accumulated versus positron energy, which, in most cases, is the only parameter to be changed. The time it takes to accumulate a Doppler spectrum with sufficient statistics (10^6 counts in the 511 keV photo peak) varies between several minutes to half an hour, depending on the beam intensity. Hence, a full S-parameter curve versus energy may involve several hours of measurement and therefore automation of the experiments is desirable. To this end a computer program originally developed for conventional PA mea-

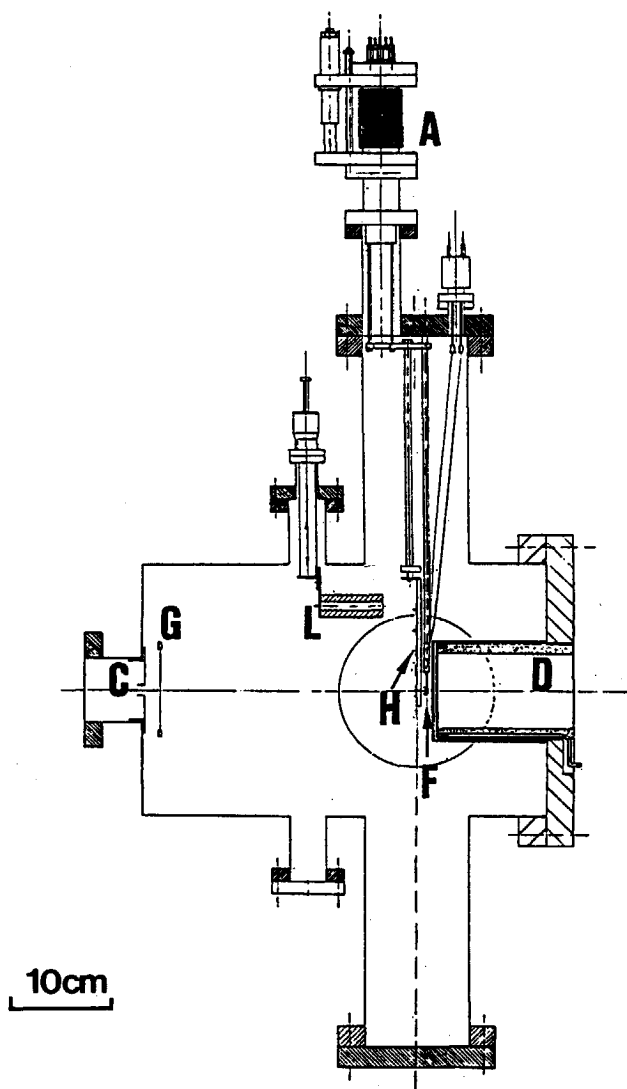


Fig. 3.11. Details of the interior of the sample chamber. Shown are the sample holder (H) connected to a linear motion transfer device (A). The samples can be heated with electrons emitted by a filament (F) placed between the sample holder and the detector well (D). The positron beam enters the sample chamber via a collimator (C) and a single grid (G). A beam limiter (L) can be lowered for studying small samples.

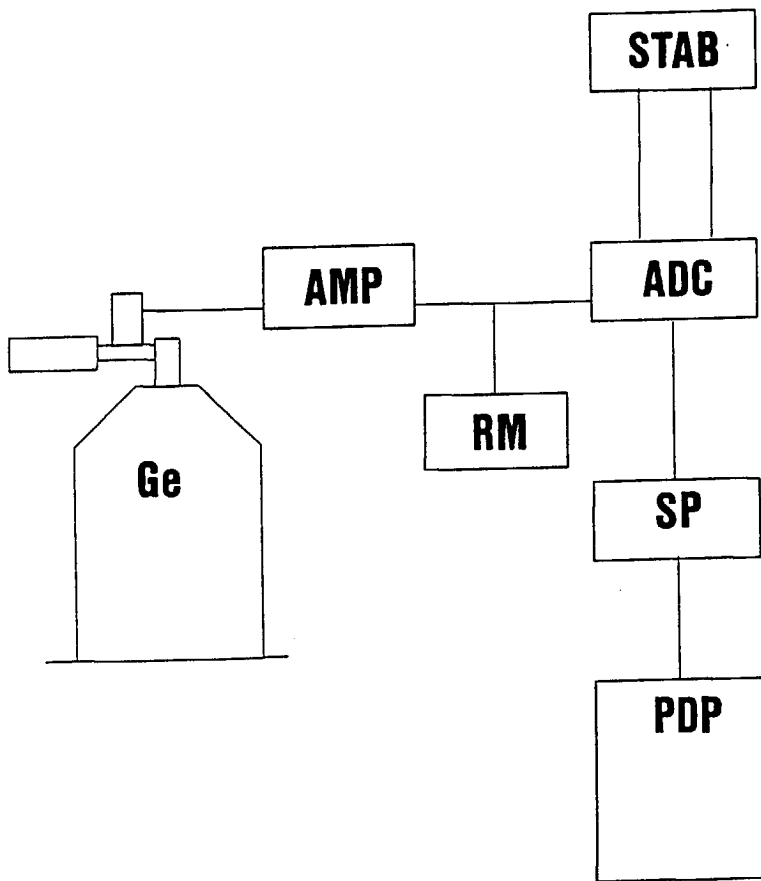


Fig. 3.12. Block scheme of the photon detection system. Ge = Ge solid state detector, AMP = main amplifier, RM = rate meter, STAB = two-point digital stabilizer, ADC = analog to digital convertor, SP = CAMAC spectrum buffer and PDP = PDP 11/44 computer.

surements has been modified for usage in positron beam experiments. The program runs on a PDP 11/44 computer which is connected to the experimental setup via a CAMAC interfacing system. The program controls the accumulation and manipulation of the spectra and the setting of the positron acceleration voltage.

One of the main features of the program is the on-line determination of the S-parameter and the Ps-fraction. After the accumulation of the first spectrum the position (channel number) of the 122 keV peak and the 511 keV peak are determined by searching for the channel with the highest contents in selected spectrum regions. These positions are taken as references for the position of a number of integrating intervals. In case of S-parameter measurements windows are set covering a central region (7 channels) and a total region (100 channels) centered around the position of the 511 keV peak. In addition, two windows used for the determination of the averaged background contribution are set on either side of the 511 keV peak. In case of Ps-fraction measurements the 122 keV peak is also used to define the total spectrum region. This region extends from the position of 122 keV peak (added with an extra 30 channels) to the position of the 511 keV peak. The peak region covers an interval of 100 channels centered around the 511 keV peak.

After the parameters have been calculated the spectrum is stored on disk and the spectrum buffer is cleared. Between the moment of clearing the buffer and starting the accumulation of a next spectrum the next positron energy is set. Control of the acceleration voltage is done via a 16-bits Digital to Analog Convertor (ADC) CAMAC module connected to the high voltage power supply.

3.3 Beam performance

3.3.1 Slow positron yield

A commonly quoted figure of merit for positron moderators is the conversion efficiency, ϵ , defined as the ratio of the number of moderated positrons extracted in the beam to the total positron activity of the primary positron source. Note that this is a definition of the overall moderation efficiency including effects due to positron selfabsorption in the source material, absorption in the source windows and geometri-

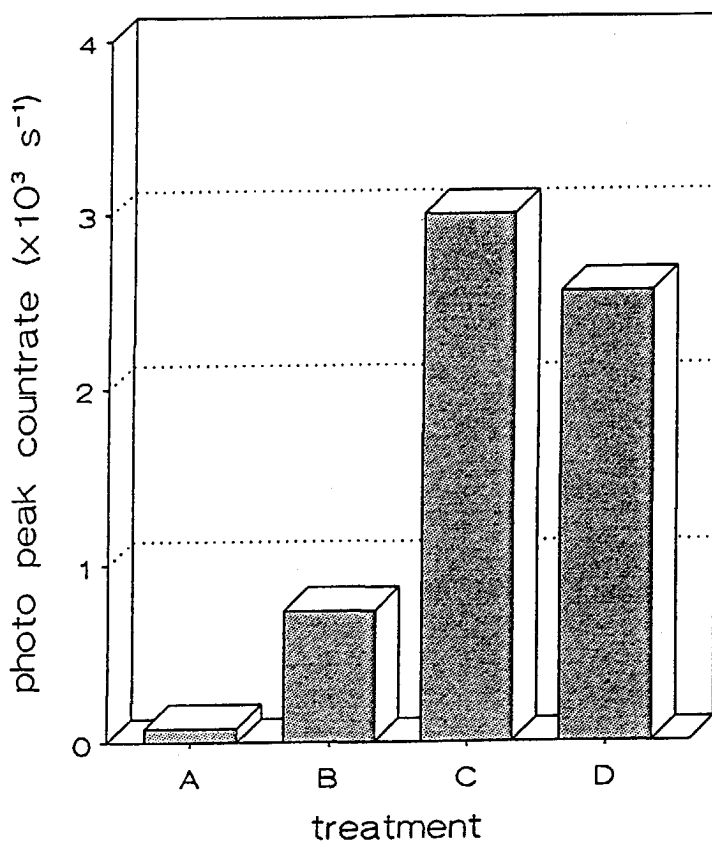


Fig. 3.13. The count rate measured in the 511 keV photo peak after different treatments of the moderator foil: A = foil as received; B = after annealing for 10 minutes at high temperatures (1500–2000 K); C = after heating in a 2×10^{-4} Pa oxygen atmosphere; D = after waiting for a period of 24 hours.

cal aspects. Values of ϵ for poly-crystalline or single crystal transmission moderators (W or Ni) vary between 5×10^{-4} and 1×10^{-4} , which is an order of magnitude worse than those of moderators operating in backscatter geometry (see ref. 4 and references therein).

To obtain acceptable moderator efficiencies W-moderator foils are submitted to the following treatments:

- annealing at high temperatures (~ 2000 °C) in order to remove positron trapping centers from the lattice,
- exposure to oxygen at elevated temperatures for the removal of carbon impurities,
- repeated annealing at moderate temperatures in order to remove water vapour and other weakly adsorbed gases from the moderator surface.

The effect of these treatments on the $8\mu\text{m}$ thick poly-crystalline W moderator used in the VEP is depicted in Fig. 3.13. It shows the count rate in the 511 keV photo peak measured with the Ge detector positioned at the end of the beam line after different treatments of the moderator foil. Installing the foil without any further treatment yielded a count rate of 80 cps. Annealing of the foil during 10 minutes resulted in an increase of the count rate to 740 cps.

During the annealing the temperature of the foil was measured with a WRe3%–WRe25% thermocouple attached to the edge of the foil. However, the temperature indicated by the thermocouple was found to be much too low compared to the temperature derived from the color (bright white) of the foil. This inconsistency was probably caused by improper fastening of the thermocouple.

The next step involved exposure of the moderator to 2×10^{-4} Pa oxygen while heated. This resulted in a further increase in count rate to 3×10^3 cps. Repeating the last step did not significantly increase the count rate. A measurement of the count rate after waiting for 24 hours revealed a reduction in count rate of 15%, probably due to contamination of the moderator surface by adsorbed gases. No further reduction was observed after waiting for longer periods of time.

Based on a measured total count rate of 1.6×10^4 cps, an overall source strength of 25 mCi (90% positron decay events) and an estimated

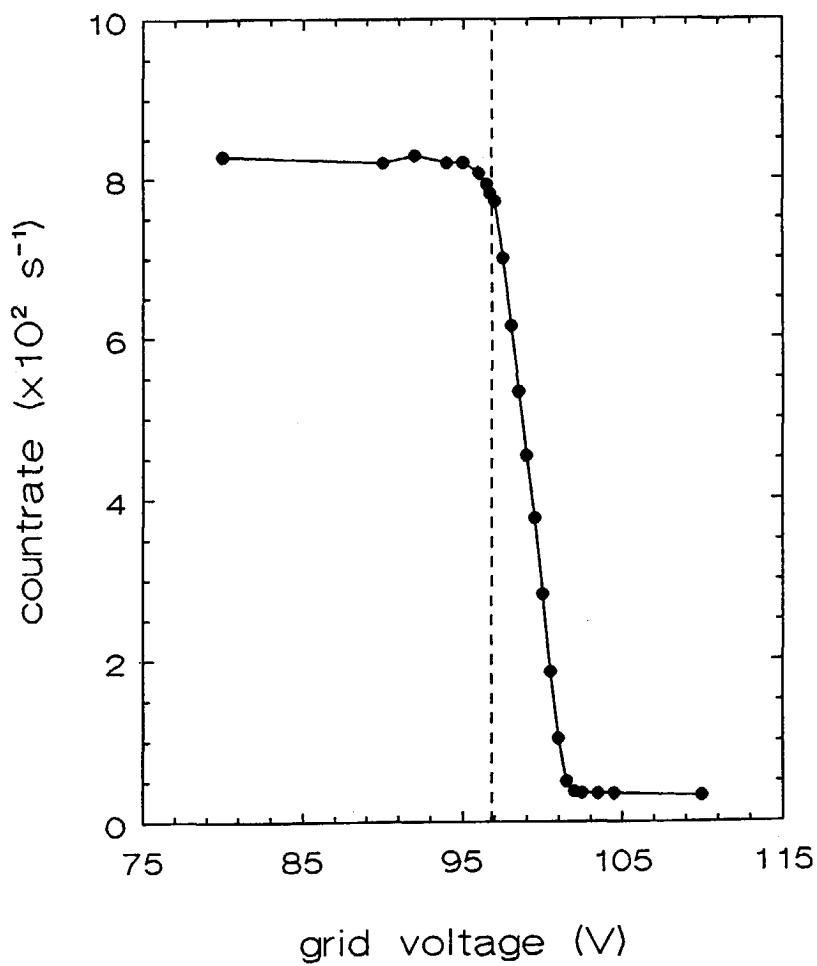


Fig. 3.14. Count rate vs. grid voltage. The dashed line indicates the positron initial energy (96.8 eV).

absolute detector efficiency of 5% (including the geometry of the setup) the efficiency of the moderation process is calculated to be 2×10^{-4} which is characteristic for transmission moderated beams.

3.3.2 Energy resolution

Another parameter describing the quality of positron beams is the beam energy resolution. In order to have an indication of the energy resolution of the VEP a single grid retarding field measurement has been performed. Positrons are accelerated to an energy of 96.8 eV and magnetically transported to the sample chamber where they, after passing a grid, annihilate at the detector well. By increasing the grid voltage to values just above the acceleration voltage positrons approaching the grid are reflected towards the accelerator and do not contribute to the annihilation spectrum.

Fig. 3.14 shows the count rate *vs.* grid voltage. A drop in the count rate occurs at a grid voltage of about 97 V. The dashed line in this figure indicates the positron initial energy. The derivative of the count rate is shown in Fig. 3.15, where the horizontal axis represents the difference between the grid voltage and the acceleration voltage, $V_g - V_{acc}$. This figure shows a continuous energy distribution ranging from ~ 0 to 5 eV. The 3 eV maximum positron energy corresponds well with the value obtained by Schultz⁵ in a similar experiment on a $15 \mu\text{m}$ thick poly-crystalline W foil and is consistent with the value of the positron work function of W(100) and W(110) single crystal surfaces (-3.0 ± 0.1 eV).^{6,7}

Note that in case of a magnetically guided positron beam a retarding field measurement yields the longitudinal energy distribution of the beam. The total energy distribution of positrons emitted by the moderator is much narrower than that shown in Fig. 3.15. Positrons emitted at large angles from the moderator surface cause an apparent low energy tail in the measured energy distribution due to the conversion of the transverse momentum component into a gyration motion around the axial magnetic field.

The total width of the measured energy distribution is ~ 4.3 eV. This is a factor of two larger than the width quoted by Schultz⁵ (for comparison, in Fig. 3.15 the scaled low energy part of the energy dis-

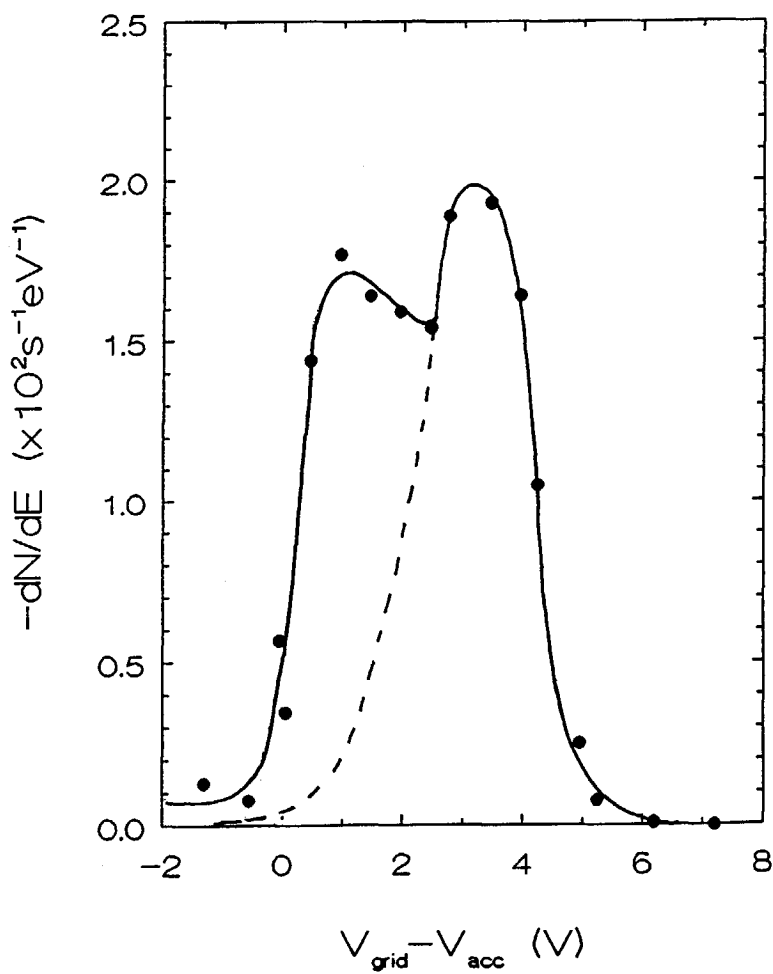


Fig. 3.15. Longitudinal energy distribution of positrons emitted by the moderator. The dashed line represents the low-energy part of the energy distribution given by Schultz⁵.

tribution measured by this author is shown by the dashed line). The shoulder in the low energy part of the distribution can be ascribed to positrons which have experienced elastic or inelastic scattering from electrons or phonons at the moderator surface. In addition, the microscopic roughness of the moderator surface changes the angle of positron emission and thus the axial component of the momentum. In a study of the energy distribution of positrons re-emitted from thin (100-500 nm) W(100) single crystal foils similar (although less pronounced) contributions have been observed which were attributed to the presence of an oxygen overlayer responsible for the scattering processes⁶.

3.3.3 Beam oscillations

One problem associated with the performance of positron beams is the motion and the broadening of the beam as a function of the beam energy. These are unwanted effects especially in cases of small samples being studied. These problems may be circumvented by placing one or more collimators in the beam line but this has the disadvantage of reducing the intensity of the beam.

Fig. 3.16 shows an example of oscillations in the count rate measured at the detector well as a function of the positron incident energy. Again, before hitting the well positrons entering the sample chamber pass a 10 mm diameter collimator. Initially it was thought that these oscillations were caused by improper alignment of the beam. However, attempting to reduce the oscillations by placing extra correction coils at different positions along the beam line had as only effect that the overall count rate decreased.

This observation strongly suggested that the oscillations were due to broadening of the beam. The most likely place for this to happen is in the accelerator where the positrons move in a combination of static magnetic and electric fields. Solutions of the equation of motion for charged particles moving in combined electric and magnetic fields can be obtained in a straightforward manner (see for example ref. 2). One of the main features of the motion of e.g. positrons in non-parallel electric and the magnetic fields is the so-called $E \times B$ drift accompanied by a gyration motion.

In the following, a simple semi-quantitative description of this mo-

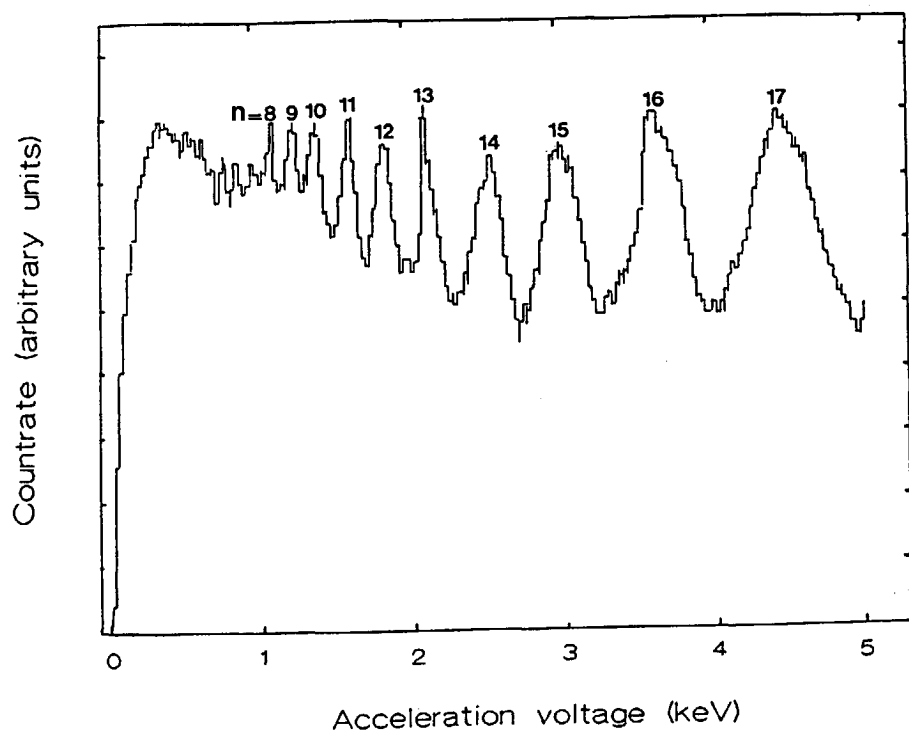


Fig. 3.16. The annihilation photon count rate *vs.* the positron acceleration voltage V_{acc} . The positrons annihilate at the detector well after having passed a 10 mm diameter collimator. The oscillations are due to a distortion in the electric field in the accelerator. The numbers, n , indicating the maxima in the count rate are derived from the condition $V_{acc} n^2 = \text{constant}$.

tion will be presented in order to explain the oscillations observed in the count rate.

Fig. 3.17 shows a cross-section of the beam entering the accelerator section. Four positron positions (p_1 to p_4) and the perpendicular component of the electric field are indicated. Note that the electric field is assumed to be cylindrically symmetric about the center of the beam line. The electric field causes the positrons to be accelerated in a direction perpendicular to the direction of motion of the positrons entering the accelerator. The magnetic field, however, prevents this and as a result the positrons start to gyrate about the magnetic field lines as indicated in the figure. The gyration (or precession) radius depends on the strength of the magnetic field and the perpendicular component of the electric field.

After having passed the accelerator the positrons have gained a kinetic energy eV_{acc} which corresponds to a classical velocity, v_{e+}

$$v_{e+} = \sqrt{\frac{2eV_{acc}}{m}} \quad (3.3)$$

with m being the positron mass and e the elementary charge. The precession frequency, ω_b , of the positrons travelling in the magnetic field is given by

$$\omega_b = \frac{eB}{m} \quad (3.4)$$

where B is the magnetic field strength. The time, t_n , it takes to make n revolutions is

$$t_n = \frac{2\pi n}{\omega_b} \quad (3.5)$$

and during this time the center of motion has covered a distance L_n given by

$$L_n = v_{e+} t_n. \quad (3.6)$$

Combining the above mentioned equations gives a relation between the acceleration voltage and the number of revolutions completed

$$\ln V_{acc} = 2 \left[\ln \left(L_n B \sqrt{\frac{e}{8\pi^2 m}} \right) - \ln n \right] \quad (3.7)$$

In Fig. 3.18 the acceleration voltages corresponding to the maxima in count rate (see Fig. 3.16) are plotted *vs.* n . The values of n are derived

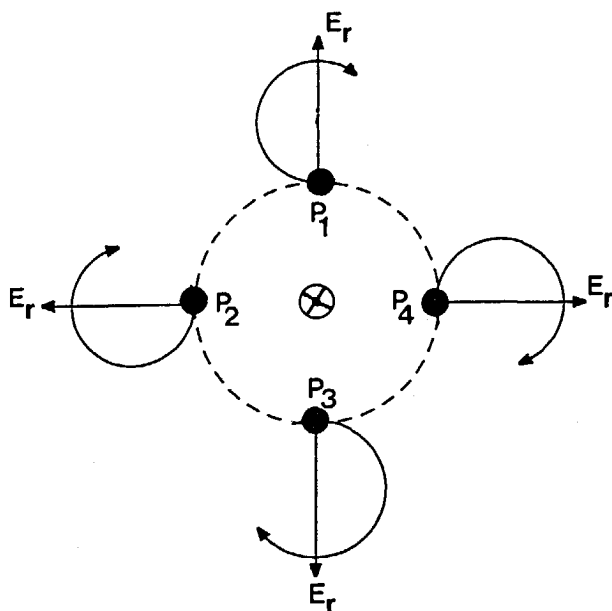


Fig. 3.17. The motion of a positron in a combination of electric and magnetic fields. The figure shows four positions ($p_1 \dots p_4$) of positrons entering the accelerator. The radial components, E_r , of the electric field, which is assumed to be cylindrically symmetric about the center of the beam, is also indicated. The direction of the initial motion of the positrons and the magnetic field are perpendicular to the plane of drawing. The gyration motion of the positrons is represented by the curved arrows.

from the condition that $V_{acc} n^2$ should be constant. The line in this figure is calculated using eq.(3.7) with $L_n B = 1.15 \times 10^{-2}$ T.m. With a value for $B = 10^{-2}$ T we find $L_n = 1.15$ m. This value corresponds fairly well with the distance between the collimator located at the entrance of the sample chamber and the accelerator.

Checking of the accelerator revealed that one of the internal resistors was not properly connected to the accelerator plate. This caused a strongly divergent electric field between the two adjacent plates responsible for the pick up of extra transverse momentum by the positrons. After having reconnected the resistor a measurement of the count rate *vs.* beam energy showed that the oscillations of the beam were no longer present.

We conclude this chapter by stating that a variable energy positron beam facility has been designed and constructed suitable for studying surface and near surface phenomena of solids under UHV conditions. The overall performance of the apparatus is such that it can compete with other positron beam systems. A fast-to-slow positron conversion efficiency has been achieved which is typical for transmission moderated beams. The energy of the beam can be varied from 100 eV to 30 keV. This enables the study of solids over a depth ranging from the surface to several microns.

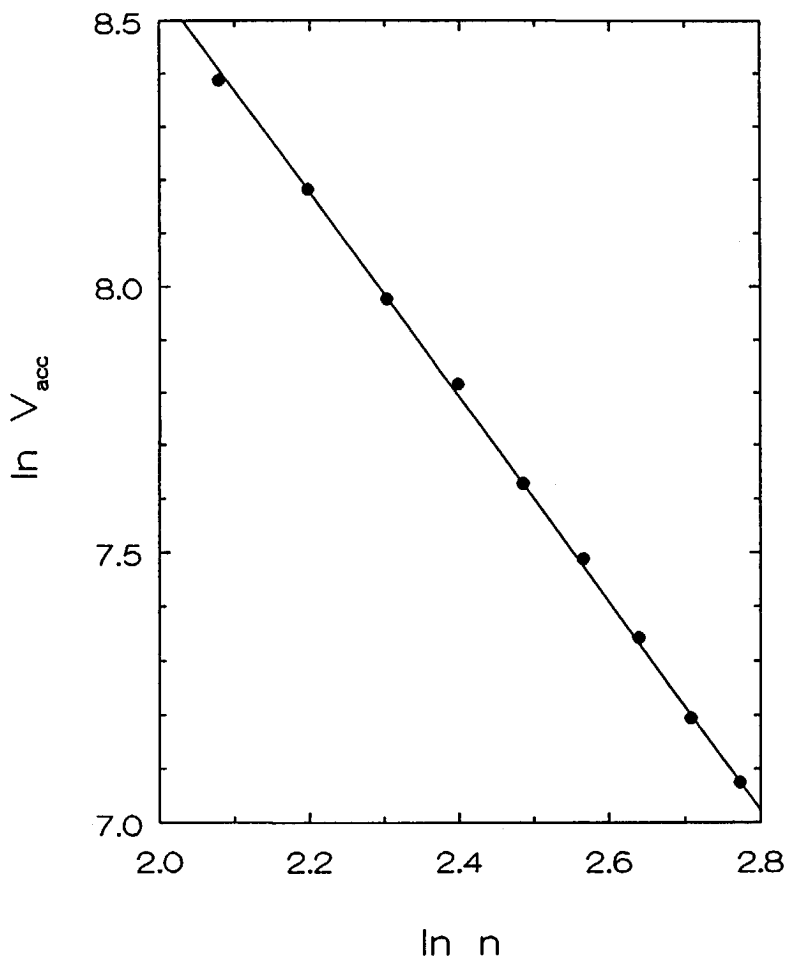


Fig. 3.18. The logarithm of the acceleration voltage at the maxima in count rate *vs.* the logarithm of n (see Fig. 3.16). The line is calculated using eq. (3.7) with $BL_n = 1.15$ Tm. (B is the strength of the axial magnetic field and L_n is the distance covered by the center of motion after n revolutions).

References chapter 3

1. J. Lahtinen, A. Vehanen, H. Huomo, J. Mäkinen, P. Huttunen, K. Rytsöla, M. Bentzon and P. Hautojärvi, Nucl. Instr. Meth. B **17**, 73, (1986).
2. J.D. Jackson, *Classical Electrodynamics*, (Wiley and Sons, New York, 1975).
3. A. van Veen, A. Warnaar and L.M. Caspers, Vacuum **30**, 109, (1980).
4. P.J. Schultz and K.G. Lynn, Rev. Mod. Phys. **60**, 701, (1988).
5. P.J. Schultz, Nucl. Instr. Meth. B **30**, 94, (1988).
6. D.M. Chen, K.G. Lynn, R. Pareja and B. Nielsen, Phys. Rev. B **31**, 4123, (1985).
7. P.J. Schultz, K.G. Lynn, W.E. Frieze and A. Vehanen, Phys. Rev. B **27**, 6626, (1983).

Chapter 4

Positron surface branching

4.1 Introduction

Recently, several variable energy positron beam experiments have been reported^{1,2,3,4} which aimed at measuring defect profiles created by keV ion bombardment of metal and semiconductor surfaces.

A relatively fast measuring method⁵ involves a study of the re-emitted positronium (Ps) fraction as a function of the positron incident energy. Under the condition that all the re-emitted positrons are forced to return to the surface of incidence, e.g. by applying an electric field, the measured positronium fraction is proportional to the fraction of implanted and subsequently thermalized positrons that diffuse back to the surface. With the proper proportionality constant and by comparing with model calculations an estimate of the defect depth profile can be obtained. Further improvement of the defect profile analysis can be obtained by measuring also the Doppler broadening parameter, $S(E)$, as a function of the positron incident energy.

It has been shown⁶ that by combining the Ps-fraction and S-parameter measurements direct information is available on the fraction of positrons trapped at defects. In the above mentioned method it is assumed that the surface conditions remain unchanged during the experiments. Problems in the application of the method may arise when for some reason, e.g. due to thermal annealing or due to the irradiation itself, the surface conditions and therewith the positron surface branching ratios change. In these cases it is impossible to determine

whether a change in positronium fraction is caused by surface effects or by a change in the bulk defect concentration. In particular irradiation with chemically active ions, such as H^+ and N_2^+ might lead to coverage of the surface with these gases.

In this chapter it will be shown that an extension of the usual measurements to include the situation where re-emitted positrons are removed from the target and detector area, is sufficient to obtain information on the effect of changes in the surface condition on the positron surface branching ratio.

In the next section the theoretical background of the method is given. The experimental conditions are briefly described in section (4.3). The results obtained with the proposed method and an example of depth profiling using this method together with the discussion are presented in section (4.4) In section (4.5) the conclusions are drawn.

4.2 Theoretical background

The fate of a positron implanted and thermalized inside a metal can be described by one of the following processes⁷, with the fraction of positrons involved in the particular process given between parentheses:

1. annihilation in the bulk of the material (f_b),
2. trapping in a defect localized state followed by annihilation in that state (f_t),
3. trapping in a two-dimensional or localized positron surface state (f_{ss}),
4. positronium formation, direct or by a thermally activated process in which a surface-bound positron is desorbed as positronium (f_{Ps}), and
5. emission as a free positron (f_{e+}).

It is anticipated that the above mentioned processes also may occur for epithermal positrons. If epithermal positrons behave differently from thermal positrons this will be noticeable at low positron incident energies, as far as the surface branching ratios are concerned. In general

epithermal positrons affect the defect trapping rate and therewith the derived trapped fraction. Positron backscattering is not included in this picture because annihilation of backscattered positrons is not detected. Fig. 4.1 displays the different fractions. Manipulation of the re-emitted positrons is achieved by applying a positive or a negative (50 V) voltage to a grid facing the sample surface. At a positive grid voltage it is assumed that all re-emitted positrons return to the sample surface where they finally form positronium or end up in the surface state with fractions denoted by f_{Ps}^r and f_{ss}^r , respectively. At a negative grid voltage the re-emitted positrons escape from the sample and detector region and are therefore not detected, though a small fraction may annihilate when colliding with the grid. The positronium fractions measured *vs.* positron incident energy E at positive or negative grid voltage are denoted by $f^+(E)$ and $f^-(E)$, respectively. These fractions are derived from the shape of the annihilation photon spectrum following the method given in chapter 1 and are related to the other fractions (see) as follows:

$$f^+ = f_{Ps} + f_{Ps}^r \quad (4.1)$$

$$f^- = f_{Ps}/(1 - f_{e+}). \quad (4.2)$$

In order to determine the values of all other fractions and branching ratios two additional relations are needed. The first is given by the branching ratio, ϵ_r , of re-emitted positrons ending up as positronium when returning to the sample surface

$$\epsilon_r = f_{Ps}^r/f_{e+}. \quad (4.3)$$

As shown in the appendix ϵ_r can be calculated as follows

$$\epsilon_r = \left[1 + \frac{P_1}{P_0} \frac{R_1 - \Delta R}{\Delta R - R_0} \right]^{-1}. \quad (4.4)$$

This expression is similar to the one given by Lynn⁵ for determining the positronium fraction measured at a positive grid voltage. In eq. (4.4), P_1/P_0 , R_1 and R_0 are system parameters (see chapter 1). ΔR is defined as

$$\Delta R = \frac{\Delta T - \Delta P}{\Delta P} \quad (4.5)$$

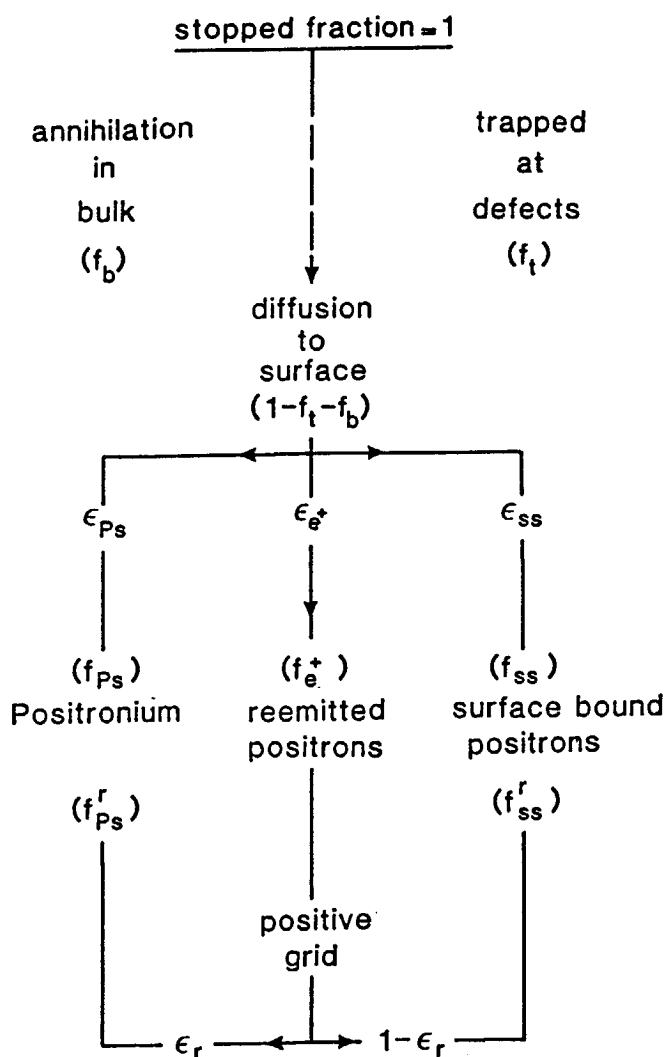


Fig. 4.1. Definition of the positron surface branching ratios and fractions of implanted positrons for the different processes.

with ΔT and ΔP given by $T^+ - T^-$ and $P^+ - P^-$, respectively. $T^{+,-}$ and $P^{+,-}$ define the number of counts accumulated in the "total" and the "peak" region of the annihilation photon spectrum measured at a positive or a negative grid voltage, respectively.

In order to derive a second extra relation we account for the fact that the surface branching ratios ϵ_{Ps} , ϵ_{e+} and ϵ_{ss} are independent of the positron incident energy so that the balance equation can be written as

$$1 = f_b + f_t + f_{e+} + \epsilon_d^{-1} f_{Ps} \quad (4.6)$$

where the branching ratio $\epsilon_d = \epsilon_{Ps}/(\epsilon_{Ps} + \epsilon_{ss})$.

For positron incident energies approaching zero and with the assumption of a perfectly absorbing surface (and consequently $f_b + f_t = 0$) it follows that

$$\epsilon_d = f_{Ps}(0)/(1 - f_{e+}(0)). \quad (4.7)$$

It can be shown that ϵ_d equals $f^-(0)$, the value of which can be obtained by extrapolating the measured $f^-(E)$ curve to zero energy. It must be noted that the extrapolation may cause uncertainties in the analysis. However, an a posteriori check is possible on the validity of the extrapolation via the requirement that the found branching ratios should be constant over the entire positron incident energy range.

With the four experimentally obtained values for f^+ , f^- , ϵ_r and ϵ_d the different fractions can be calculated as follows:

$$f_{Ps} = f^-(\epsilon_r - f^+)/(\epsilon_r - f^-) \quad (4.8)$$

$$f_{e+} = (f^+ - f^-)/(\epsilon_r - f^-) \quad (4.9)$$

$$f_{ss} = f_{Ps}(1 - \epsilon_d)/\epsilon_d \quad (4.10)$$

$$f_{ss}^r = f_{e+}(1 - \epsilon_r). \quad (4.11)$$

$$f_{Ps}^r = \epsilon_r f_{e+} \quad (4.12)$$

With these expressions we have a complete knowledge of the branching of positrons reappearing at the surface. Finally, by using the balance equation (4.6) the fraction of positrons annihilating in the bulk and those trapped in defects is given by

$$f_b + f_t = 1 - f_{e+} - \epsilon_d^{-1} f_{Ps}. \quad (4.13)$$

A method for determining f_t and f_b separately has been discussed elsewhere⁶. It appeared that in a measurement of the S-parameter, which can be thought of as a linear combination of the S-values weighed by the corresponding fractions, part of the Ps-fraction is weighed less, because the annihilation of ortho-Ps contributes only for a minor fraction to the 511 keV photon peak. Due to the selectivity of the S-parameter for two-photon annihilation events an extra relation between the above mentioned fractions is available,

$$f_t S_t^* = (\beta f^+ + f'_{ss} + f_t + f_b) S^* - \beta f^+ S_{Ps}^* - f'_{ss} \quad (4.14)$$

where β is the experimentally determined para-Ps/Ps ratio⁶. This ratio was found to be 0.35 ± 0.05 , which is larger than the theoretical value of 0.25. This difference can be ascribed to "pick off" conversions of ortho-Ps interacting with surrounding materials. f'_{ss} is defined as $f_{ss} + f_{ss}^r$ and $S^*(E) = (S(E) - S_b)/(S_{ss} - S_b)$ is a normalized S-parameter. The subscripts ss , b , t and Ps refer to S-values for the surface, bulk, defects and positronium, respectively.

By applying the balance equation and assuming $S_{Ps} = S_{ss}$, eq. (4.14) can be written as

$$f_t(S_t^* - 1) = (1 - (1 - \beta)f^+)(S^* - 1) + f_b \quad (4.15)$$

With the condition that the defect concentration probed by the positrons is high enough so that $f_t \gg f_b$, which occurs for defect concentrations $> 10^{-4}$, and for positron implantation depths comparable with the depth of the defects, f_t can be found directly by combining eqs. (4.13) and (4.15).

4.3 Experimental

The results of the experiments described in this chapter are obtained with the magnetically guided positron beam at the Brookhaven National Laboratory (USA). With this apparatus transmission moderated positrons could be electrostatically accelerated to a maximum energy of 80 keV. The positrons were supplied by a 100 mCi ^{22}Na source. The target chamber was equipped with a LEED (Low Energy Electron Diffraction) and an AES (Auger Electron Spectroscopy) system for *in*

situ characterization of the sample surface. An ion beam system (from IRI, Delft) was mounted to produce mass and energy analyzed gas ion beams for defect production in the sub-surface region of a high purity and electro-polished Mo(100) single-crystal. The maximum attainable ion energy was 4 keV. The angle of incidence of the ions hitting the sample surface was 15° off the surface normal in all cases. This prevented the occurrence of anomalous ion range distributions of e.g. He due to channeling effects. Facing the sample surface a grid was positioned by which the re-emitted positrons could be extracted from or forced to return to the sample surface. During the positron experiments the pressure in the target chamber was of the order of 10^{-8} Pa and during the ion implantation 10^{-4} Pa. For the detection of the annihilation photons a Ge solid state detector was placed outside the vacuum system close to the rear side of the sample. With this configuration a count rate of $\sim 10^4$ cps was achieved.

4.4 Results and discussion

In Table 4.1 the values of the surface branching ratios are given as measured in the case of i) a 2000 K annealed and ii) an ion irradiated Mo(100) sample. The energy of the H_2^+ , He^+ and N_2^+ ions used for defect creation was 3 keV for all irradiations with a total dose of $1.0 \times 10^{15} \text{ cm}^{-2}$. In four cases the positron measurements were carried out at room temperature (RT) while in the case of the nitrogen irradiation additional measurements were performed at a crystal temperature of 700 K.

The effect of ion irradiation on the branching ratios is assumed to be caused by changes in the surface condition of the sample, e.g. by the coverage of the surface with gas atoms. In case of the nitrogen irradiation surface coverage was observed with AES. Another explanation for the changes in the branching ratios might be the presence of surface defects created during the irradiation. In the cases studied the branching of positrons into free positrons, ϵ_{e+} , varies between 0.3 and 0.5, while the branching of re-emitted positrons into positronium, ϵ_r , varies between almost 0.25 and 1.0. The value of ϵ_d ranges from 0.25 to 0.8. Heating the sample to a temperature of 700 K resulted in an increase of

Table 4.1. Positron surface branching ratios for annealed and ion irradiated Mo(100).

condition:	ϵ_{Ps}	ϵ_{e+}	ϵ_{ss}	ϵ_r	ϵ_d
2000 K	0.56	0.32	0.12	0.97	0.82
He ⁺	0.32	0.47	0.21	0.74	0.60
N ₂ ⁺	0.18	0.29	0.53	0.42	0.25
N ₂ ⁺ , 700 K	0.36	0.48	0.15	0.98	0.69
H ₂ ⁺	0.17	0.39	0.44	0.26	0.27

(all irradiations: 3 keV, 1×10^{15} ions/cm²)

the branching of re-emitted positrons into positronium to almost 1.0, indicative of complete thermal desorption of positrons bound at the nitrogen covered surface.

Fig. 4.2 shows the positron surface branching ratios ϵ_r and ϵ_{e+} vs. positron incident energy after the N₂⁺, H₂⁺ or He⁺ irradiations and after annealing. The figure shows that the values of ϵ_d as extrapolated from the $f^-(E)$ curves, as well as the values of the system parameters are correct since i) ϵ_r and ϵ_{e+} are independent of the positron energy and ii) the value of ϵ_r does not exceed unity (except from statistical scattering in the data).

In case of the annealed sample the data for ϵ_{e+} show a slight increase at low positron energies. This might be due to contributions of epithermal positrons to the measured signals. The observed effect can be explained by assuming that epithermal positrons have a higher probability for escaping surface trapping and direct positronium formation. In deriving the formulas applied for establishing the surface branching ratios we have assumed that the surface branching ratios for epithermal positrons are identical to those of the thermalized positrons. In view of the minor effect observed in our measurements we expect this assumption to be valid for this case.

As mentioned in the introduction, one of the applications of the above method is defect profiling of ion irradiated materials. As an example we describe the analysis of the data measured at the Mo(100) surface irradiated with 3 keV He⁺ ions.

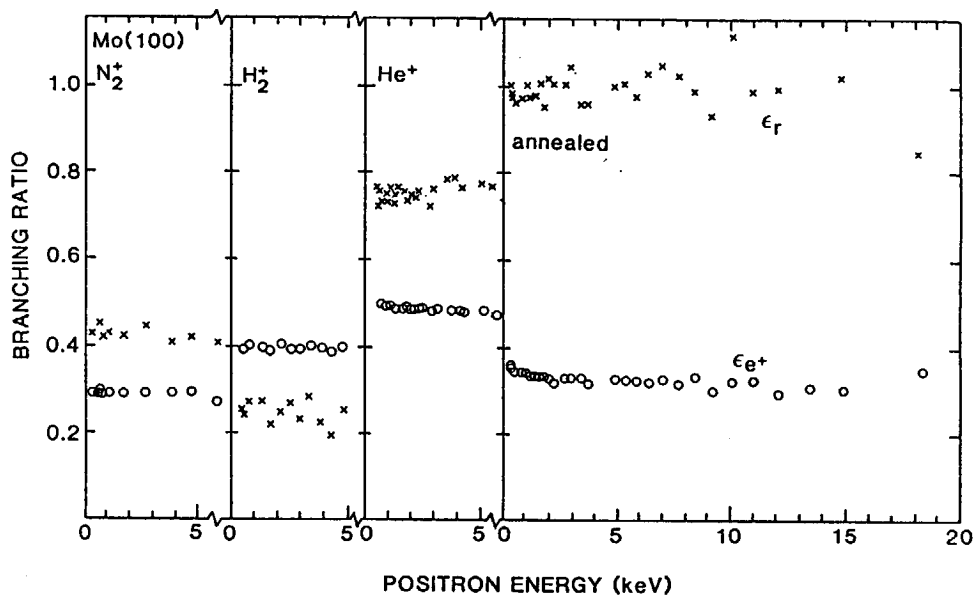


Fig. 4.2. The positron surface branching ratios ϵ_r (\times) and ϵ_{e^+} (\circ) as a function of the positron incident energy measured at a Mo(100) crystal for the N_2^+ , H_2^+ , or He^+ irradiated surface and an annealed surface. The irradiations were carried out with 3 keV ions to a dose level of $1.0 \times 10^{15} \text{ cm}^{-2}$.

1. Firstly, the fractions f_{Ps} , f_{e^+} and f_{ss} are derived from the measured f^+ , f^- , ϵ_r and ϵ_d by applying eqs. (4.8) through (4.10).
2. In the next step eq. (4.13) is applied to calculate the fraction of positrons annihilated in the bulk and in defects. This fraction *vs.* positron energy is depicted in Fig. 4.3A (full circles).
3. In order to separate the fraction of positrons annihilated in the defects use is made of the results of an additional measurement of the S-parameter as a function of the positron energy. These results are shown in Fig 4.3B. The fraction of positrons annihilated in the defects only, f_t , found by following the procedure outlined in the previous section, is shown in Fig. 4.3A (open circles). Here the assumption has been made that for low positron energies (below 2 keV) $f_t \gg f_b$.
4. The final step involves a comparison of calculated f_t curves with the experimentally obtained data. For this purpose the stationary positron diffusion equation, describing the diffusion and depth dependent trapping of positrons in materials containing defects, has been solved in an iterative way. The parameters which could be hand-adjusted are those describing the defect distribution and the normalized defect S-values.

Both the defect distribution and the positron implantation profile are represented by a Makhov distribution (see section 2.2.3)

$$P(z) = \frac{mz^{(m-1)}}{z_0^m} \exp[-(z/z_0)^m] \quad (4.16)$$

with $m = 2$ for the positrons and $m = 1.5$ for the defects. When eq. (4.16) describes the initial positron distribution, z_0 varies with the positron energy as

$$z_0 = A E^{1.6} \quad (4.17)$$

with A a material dependent constant. When eq. (4.16) represents the defect distribution, z_0 is related to the mean defect depth. The values of the positron diffusion length in Mo, the positron bulk annihilation rate and the defect trapping rate are chosen to be 75 nm, $8.3 \times 10^9 \text{ s}^{-1}$ and $2.6 \times 10^{14} \text{ s}^{-1}$, respectively.⁸

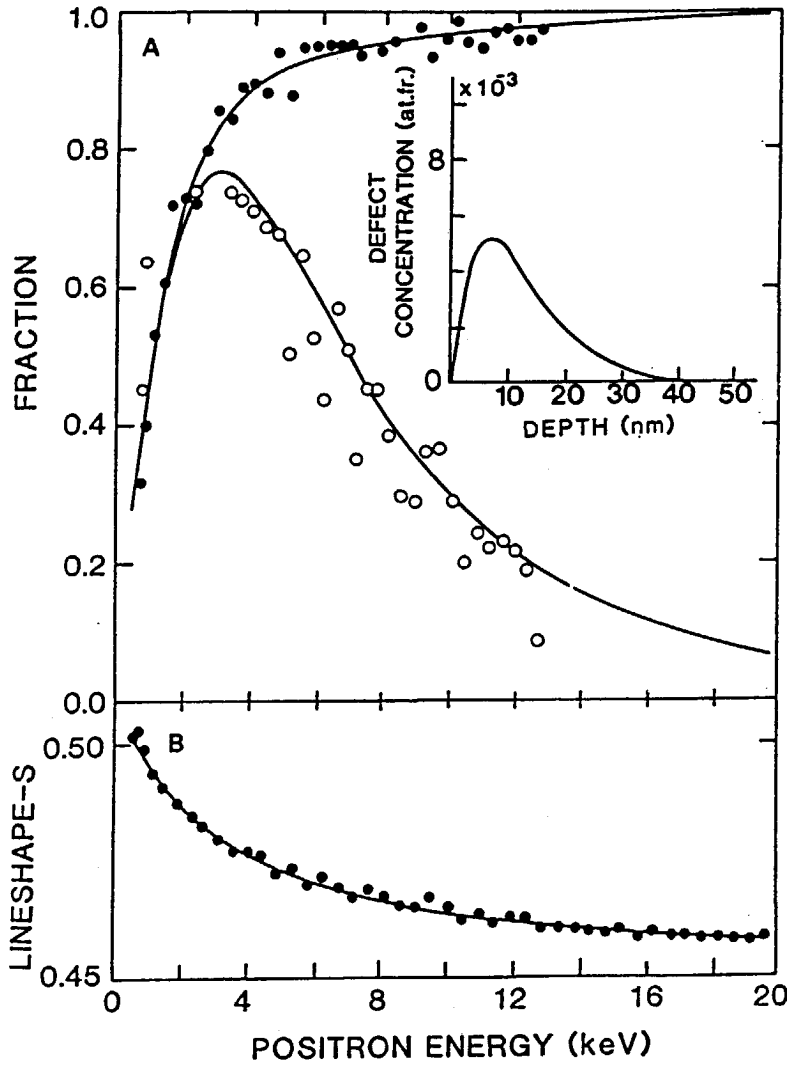


Fig. 4.3. The results of the defect profiling measurements for a 3 keV, $1.0 \times 10^{15} \text{ He}^+ \text{ cm}^{-2}$ irradiated Mo(100) sample. In A the measured (●) and calculated (full line) fractions of positrons annihilated in the bulk and in the defects are shown vs. positron energy. B) Shows the experimental (●) and calculated (full line) S-parameter as a function of the positron energy. From these two measurements the fraction of positrons trapped at the defects is derived ((○) in A). The inset shows the defect concentration as a function of the depth below the surface used for calculating the fraction of positrons trapped at the defects.

The values finally obtained for the areal defect concentration and the mean defect depth are $5 \times 10^{14} \text{ cm}^{-2}$ and 11 nm, respectively. The defect concentration *vs.* depth is depicted in the inset of Fig. 4.3. The value of the normalized S-parameter for the defects is calculated to be 0.28.

MARLOWE calculations of He ranges and deposited energy distributions for a comparable case (3 keV He in randomly orientated Nb) by Littmark⁹ yielded a He projected range of 12 nm and a vacancy distribution with mean depth of 12 nm. These values correspond fairly well with the results obtained in this study. Thermal Desorption Spectrometry (TDS) measurements on 3 keV He irradiated Mo(110) and Mo(210) surfaces^{10,11} yielded a RT vacancy production of 0.5 and 0.6 vacancies per incident ion, respectively. For a He dose of $1.0 \times 10^{15} \text{ He cm}^{-2}$ this corresponds to 5.0×10^{14} and 6.0×10^{14} vacancies cm^{-2} , in agreement with the areal defect concentration derived from the positron measurements.

4.5 Conclusion

It has been shown that positron surface branching ratios can be determined experimentally by positronium fraction measurements under two experimental conditions, i.e. by applying a positive or a negative grid voltage. Future work might be aimed at establishing quantitatively the dependence of the branching ratios on surface coverage, crystal orientation and temperature. Applications are:

1. defect studies:
separation of effects on the surface branching ratio due to changes in the surface conditions from those due to changes in the defect population and distribution, e.g. caused by thermal annealing or by ion irradiation.
2. surface studies:
monitoring of surface conditions, e.g. gas coverage or desorption and annealing of surface defects.

4.6 Appendix

In this appendix an expression is derived which relates the branching of re-emitted positrons into positronium to the "peak" and "total" count rates measured at positive and negative grid voltages.

The method is based on the analysis of Ps-fraction measurements described by Lynn⁵.

Let N be the total number of positron annihilation events per unit of time. To this number a contribution, N_e , is made by re-emitted positrons reappearing at the sample surface. Because of the low energy (typically a few eV) of these positrons they are assumed to form either positronium or to end up in the surface state. The fraction of re-emitted positrons forming positronium is denoted by ϵ_r . The remaining number of annihilation events, $N_0 = N - N_e$, consists of annihilations in the bulk, in defects and at the sample surface (direct formation of Ps and direct surface trapping). The fraction of this number due to the annihilation of Ps is denoted by f_0 .

With these definitions the number of annihilation events other than Ps annihilation, N_a^+ , at a positive grid voltage is given by

$$N_a^+ = N_0(1 - f_0) + N_e(1 - \epsilon_r). \quad (4.18)$$

Of the positrons annihilating in the Ps-state a fraction β is in the para-Ps state and a fraction $1 - \beta$ in the ortho-Ps state. The total number of annihilation events from these states is given by

$$N_p^+ = \beta(N_0 f_0 + N_e \epsilon_r) \quad (4.19)$$

and

$$N_o^+ = (1 - \beta)(N_0 f_0 + N_e \epsilon_r) \quad (4.20)$$

where the subscripts p and o denote para- and ortho-Ps.

The number of counts accumulated in the "total" energy region of the annihilation photon energy spectrum in case of a positive grid voltage is given by

$$T^+ = N_a^+ h_a + N_p^+ h_p + N_o^+ h_o \quad (4.21)$$

with h_a , h_p and h_o probability constants for detecting the particular photons in the "total" spectrum region.

A similar expression is derived for the counts accumulated in the "peak" region of the spectrum

$$P^+ = N_a^+ g_a + N_p^+ g_p + N_o^+ g_o \quad (4.22)$$

with the probability constants for detecting the photons in the "peak" region denoted by g_a , g_p and g_o . When applying a negative grid voltage it is assumed that all re-emitted positrons escape from the detector region and therefore do not contribute to the photon spectrum. This assumption results in setting $N_e = 0$ in eqs. (4.19) and (4.20). At a negative grid voltage the number of counts in the "total" and "peak" regions are denoted by T^- and P^- . By taking the differences $\Delta T = T^+ - T^-$ and $\Delta P = P^+ - P^-$ we get:

$$\Delta T = N_e[(1 - \epsilon_r)h_a + \epsilon_r(1 - \beta)h_o + \epsilon_r\beta h_p] \quad (4.23)$$

and

$$\Delta P = N_e[(1 - \epsilon_r)g_a + \epsilon_r(1 - \beta)g_o + \epsilon_r\beta g_p] \quad (4.24)$$

These two equations are similar to those relating the number of counts T^+ and P^+ to the Ps-fraction⁵, and therefore we may write

$$\epsilon_r = \left[1 + \frac{P_1}{P_0} \frac{R_1 - \Delta R}{\Delta R - R_0} \right]^{-1} \quad (4.25)$$

with ΔR defined as

$$\Delta R = \frac{\Delta T - \Delta P}{\Delta P}. \quad (4.26)$$

The parameters P_1/P_0 , R_1 and R_0 are system specific parameters, with values of 0.45, 6.6 and 2.6, respectively, for the Brookhaven system.

References chapter 4

1. G. Kögel and W. Triftshäuser, *Rad. Effects* **78**, 221, (1983).
2. A. Vehanen, J. Mäkinen, P. Hautojärvi, H. Huomo, J. Lahtinen, R.M. Nieminen and S. Valkealahti, *Phys. Rev. B*, **32**, 7561, (1985).
3. Y. Iwase, A. Uedono and S. Tanigawa, in *Positron Annihilation*, Proc. of the 7th Int. Conf. on Positron Annihilation, eds. P.C. Jain, R.M. Singru and K.P. Gopinathan, (World Scientific, Singapore, 1985), p.868.
4. A. Uedono, S. Tanigawa, J. Sugiura and M. Ogasawara in *Positron Annihilation*, Proc. of the 8th Int. Conf. on Positron Annihilation, eds. L. Dorikens-Vanpreat, M. Dorikens and D. Segers, (World Scientific, Singapore, 1989), p.690.
5. K.G. Lynn and D.O. Welch, *Phys. Rev. B* **22**, 99, (1980).
6. B. Nielsen, A. van Veen and K.G. Lynn, in *Positron Annihilation*, Proc. of the 7th Int. Conf. on Positron Annihilation, eds. P.C. Jain, R. M. Singru and K.P. Gopinathan, (World Scientific, Singapore, 1985), p.836.
7. A.P. Mills jr., in *Positron Solid State Physics*, Proc. of the 83rd Int. School of Physics 'Enrico Fermi', eds. W. Brandt and A. Dupasquier, (North Holland, Amsterdam, 1983), p.432.
8. P.J. Schultz and K.G. Lynn, *Rev. Mod. Phys.* **60**, 701, (1988).
9. U. Littmark, S. Maderlecher, R. Behrisch, B.M.U. Scherzer and M.T. Robinson, *Nucl. Instr. Meth.* **132**, 661, (1976).
10. M. Hou, A. van Veen, L.M. Caspers and M.R. Ypma, *Nucl. Instr. Meth.* **209**, 19, (1983).
11. A. van Veen, J.H. Evans, W.Th.M. Buters and L.M. Caspers, *Rad. Effects* **78**, 53, (1983).

Chapter 5

Positron beam studies of metallic layered structures and semiconductors

5.1 Introduction

The acceptance of positron beam analysis being a recently introduced analysis technique will depend strongly on its potential to solve problems in materials science. Exploration of the possible use of the technique has just started and is in a phase comparable to the state of another technique like Rutherford Backscattering Spectroscopy (RBS) 20 years ago. A considerable amount of systematical research has still to be done to create a data base which can be relied on for future practical use of the positron beam technique. From the exploratory studies done so far emerges the image of an analysis technique which can be applied to many areas.

In the positron beam analysis technique a positron is used as a probing particle. The positive charge of the positron makes the technique sensitive to open-volume defects, e.g. vacancies and vacancy clusters, and to internal electric fields. Due to the positron's low mass the positron beam technique is virtually non-destructive. Furthermore the technique allows the energy of the incident positrons, and therewith the implantation depth, to be varied, which gives the technique depth sensitivity. The sensitivity of the positron to the local electronic envi-

ronment is reflected by the characteristics of the annihilation process, for example by the energy of the annihilation radiation. This enables the technique to be used to distinguish between types of defects and to observe changes in defect concentrations. In order to establish these sensitivities in a qualitative sense experiments are needed on samples which have been well characterized by other techniques. In this chapter the results of a few of such studies performed with the VEP facility are reported.

Section (5.2) reports on a positron beam experiment performed on a metallic layered structure composed of a Ti layer sandwiched in between two Ni layers. This was one of the first studies carried out with the VEP facility. The reason to perform this study has been twofold. Firstly, layered Ti/Ni systems have been characterized by X-ray diffraction techniques and are therefore suitable to explore the possibilities of depth profiling measurements with variable energy positrons. Secondly, alternately stacked layers of Ni and Ti are known to be subject to diffusion induced amorphization yielding a Ti/Ni alloy when heated to elevated temperatures. We were interested whether this phenomenon could be detected with positron beam analysing techniques.

In section (5.3) the positron beam experiments performed on epitaxial layers of Si grown on a Si(100) substrate by molecular beam epitaxy (MBE) and solid-phase epitaxy (SPE) techniques are presented. The results of the experiments will be compared to the results of RBS minimum yield measurements.

In section (5.4) the results of positron beam experiments performed on Si irradiated with 30 keV He^+ ions are presented. This study forms part of a project in which porous layers in silicon created by light ion bombardment are studied with several techniques, such as SEM and THDS. Porous layers in Si may form the starting point for the formation of buried oxide layers which have their application in semiconductor technology. By utilizing positron beam techniques the evolution of the damage created during irradiation of Si with 30 keV He^+ ions with doses varying between 1.0×10^{16} and $5.0 \times 10^{17} \text{ He}^+ \text{ cm}^{-2}$ is followed.

In the final section (5.5) an evaluation of the results of the above mentioned positron beam experiments will be given.

5.2 Ni-Ti-Ni layered structure

ABSTRACT

The effect of interdiffusion of Ti and Ni in a multilayer structure of sputtered Ni/Ti/Ni on a Si substrate was studied by positron beam analysis. Interdiffusion was observed after annealing at 525 K and the depth position of the formed Ti/Ni alloyed layer could be determined. It was established that the nickel top layer was not involved in the interdiffusion process.

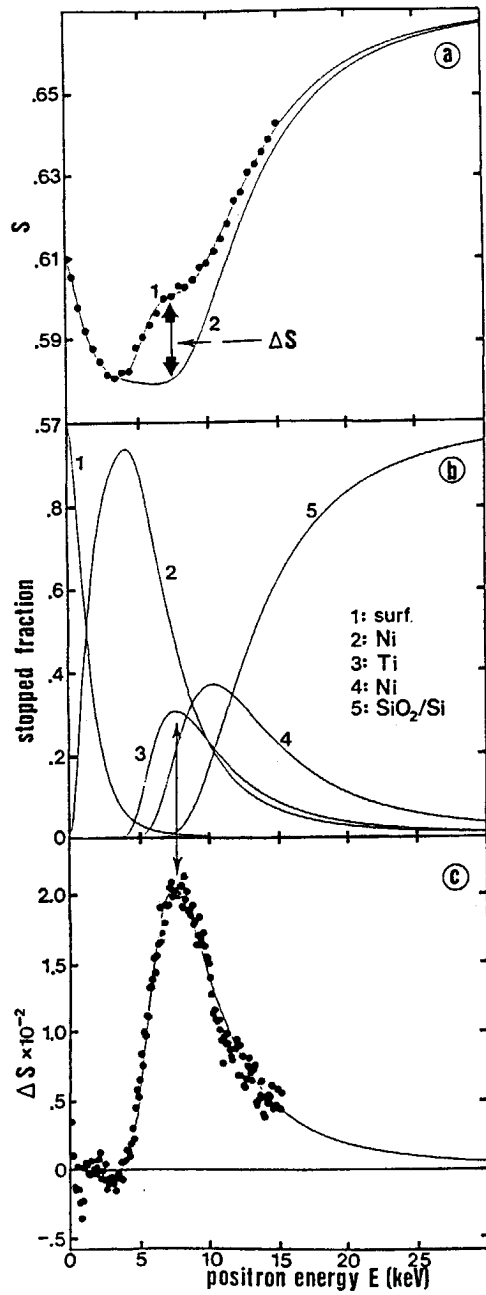
INTRODUCTION

One way of obtaining a binary amorphous alloy is by interdiffusion of alternately stacked layers of the constituent elements. Starting with a periodical multilayer structure the formation of the amorphous zone on annealing can be studied with X-ray diffraction techniques. For an assembly consisting of 10 nm thick Ni and Ti layers X-ray measurements indicated a planar growth of the amorphous layer maintaining sharp interfaces, whereas the first internal Ni/Ti interface remained inactive¹.

In this section we report on first results of a study on interdiffusion in a Ni/Ti/Ni multilayer system by using a variable energy positron beam.

EXPERIMENTAL

The results of the experiments described here are obtained with the Delft variable energy positron beam apparatus. With this system a magnetically guided positron beam with energies ranging from 100 eV to 30 keV can be produced. The positrons are supplied by a 25 mCi ²²Na source and are moderated in a 8 μ m thick poly-crystalline tungsten foil. After passing an accelerator stage the beam is guided to the sample which can be heated for annealing purposes by electron bombardment. Detection of the annihilation photons is achieved with a Ge detector placed outside the vacuum system close to the rear of the



sample. Spectra are acquired with a two-point stabilised multichannel analyser system. This setup yields positron beam intensity of $\sim 10^4$ e^+ /s.

The samples studied consist of a Ti layer sandwiched in between two Ni layers deposited on top of a SiO_2/Si substrate. The thickness of the metallic layers is 100 nm. The oxide layer (thickness 200 nm) acts as a diffusion barrier between the multilayer and the substrate. The layers are deposited by magnetron sputtering using Ar as sputter gas. X-ray diffraction analysis on 10 nm thick layers showed that the layers have a poly-crystalline structure.

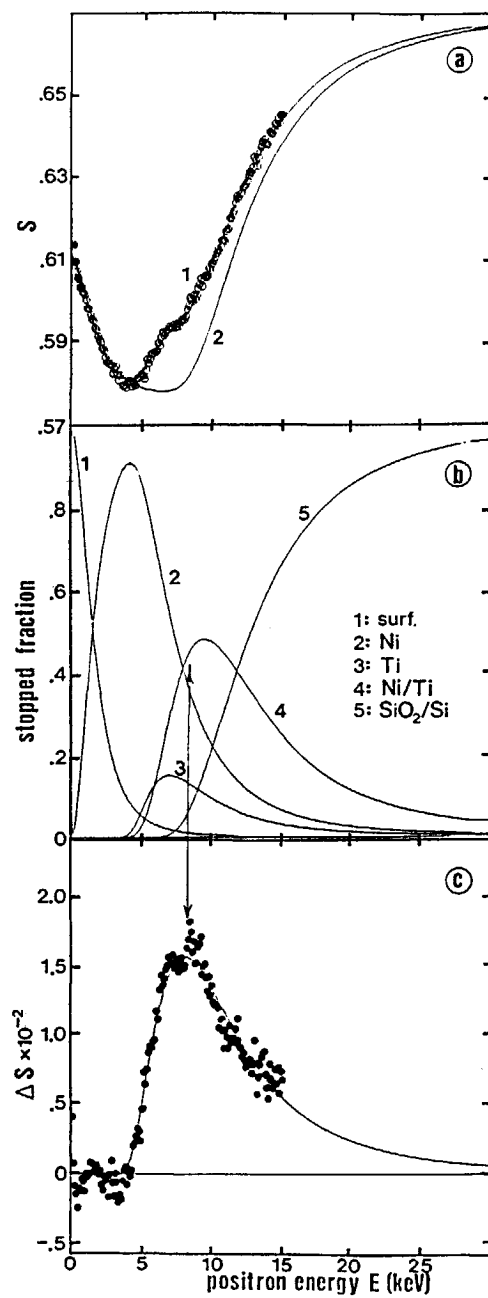
We have measured the Doppler broadening (represented by the S-parameter) of the 511 keV annihilation peak as a function of the positron incident energy. The data are analysed by calculating the contribution of each layer to the S-parameter in the absence of positron diffusion.

RESULTS AND DISCUSSION

Measured S-parameter values as a function of the positron incident energy for the as received sample are shown in Fig. 5.1a. (Note that for reasons of clearness not all data points are shown in this figure.) The following observations can be made: a steep decrease of the of

←

Fig. 5.1. Measured (\bullet) and calculated (full lines) S-parameter values (a), calculated fractions of positrons stopped in the different layers (b) and S-parameter difference (c) as a function of the positron incident energy for the as received Ni/Ti/Ni multilayer structure. Curve 2 in (a) is calculated with a single value of the S-parameter ($= .579$) for the three metallic layers. The difference, ΔS , between this curve and the measured data is shown in (c). Curve 1 in (a) is obtained when the S-parameter for the Ti layer is adjusted to $S_{Ti} = .651$. (b) shows the fraction of positrons back diffusing to the surface (1), the fraction stopped in the first Ni layer (2), in the Ti layer (3), in the second Ni layer (4) and in the substrate (5) *vs.* positron incident energy. The positions of the layer boundaries are given in Table 5.1.



the S-parameter from the surface value of $S_s = 0.610$ to a minimum value of $S = 0.579$ at a positron energy of 4 keV. The latter S-value is adopted as a characteristic value for positrons annihilating in the Ni layer. The steepness of the curve indicates a high positron trapping rate (and therewith a short diffusion length) in the first layer. This can be ascribed to the fine-grained poly-crystalline structure of the material causing strong positron trapping at the grain boundaries. Since all layers are deposited in the same way we assume a high positron trapping rate throughout the multilayer. For this reason we have analysed the experimentally obtained S-parameter curves neglecting positron diffusion in the deeper layers. Only in the first Ni layer a short effective diffusion length (≤ 10 nm) is taken into account.

By neglecting positron diffusion in the deeper layers the measured S-parameter curves can be thought of as a summation of the characteristic S-parameter value in each layer weighed by the fraction of positrons implanted in that layer. The positron implantation profile has been depth scaled to account for the different densities of the layers according to the method proposed by Vehanen². The values of the parameters describing the positron implantation profile are also taken from their work (see also chapter 2).

In Fig. 5.1 a calculated S-parameter curve is shown (curve 1). The values of the layer thickness, d , and the characteristic S-parameters of the different layers, as well as the S-parameter values for the surface and the substrate are summarized in Table 5.1. Fig. 5.1b shows the calculated fractions of positrons reappearing at the surface (curve 1)

←
 Fig. 5.2. Measured (•) and calculated (full lines) S-parameter values (a), calculated fractions of positrons stopped in the different layers (b) and S-parameter difference (c) as a function of the positron incident energy for the Ni/Ti/Ni multilayer structure after annealing (10 hours) at 525 K. Curve 2 in (a) is again calculated with a single value of the S-parameter ($= .577$) for the three metallic layers. The difference, ΔS , between this curve and the measured data is shown in (c). The fractions of positrons stopped in the different layers are shown in (b) with the positions of the layer boundaries as indicated in Table 5.1.

Table 5.1. Fitted S-parameter values, S , and layer thicknesses, d , for the Ni/Ti/Ni multilayer structure.

	surface	Ni	Ti	Ni	Ni/Ti	SiO ₂ /Si
<i>as received:</i>						
S	0.610	0.579	0.651	0.571	–	0.671
d (nm)	–	90	95	95	–	–
<i>after 525 K anneal:</i>						
S	0.610	0.577	0.651	–	0.586	0.669
d (nm)	–	90	40	–	150	–

and the fractions of positrons stopped and subsequently annihilated in the different layers and in the substrate (curves 2-5) as a function of the positron energy. Adopting a single value of the S-parameter (i.e. the value of the S-parameter characteristic for the first Ni layer) for the three deposited layers yields curve 2 in Fig. 5.1a. The difference, ΔS , between the experimentally obtained S-parameter data and curve 2 is shown in Fig. 5.1c. ΔS can be expressed by

$$\Delta S = \eta_{Ti}(S_{Ti} - S_{Ni}) + \eta_{Ni'}(S_{Ni'} - S_{Ni}) \quad (5.1)$$

where η_{Ti} and $\eta_{Ni'}$ are the fractions of positrons stopped in the Ti layer and the deeper Ni layer, respectively. S_{Ni} , S_{Ti} and $S_{Ni'}$ are the characteristic S-parameter values for the first Ni layer, the Ti layer and the second Ni layer, respectively.

Comparing Fig. 5.1b with Fig. 5.1c shows that ΔS is determined almost completely by the value of S_{Ti} . This value is found to be 12.6% higher than the value of S_{Ni} , consistent with S-parameter values measured at Ni and Ti single crystals³.

The next step in the experiment involved a 10 hour anneal of the sample at a temperature of 525 K. X-ray diffraction measurements performed on the 10 nm thick metallic layers indicate that after this treatment diffusion induced amorphization is nearly completed. An amorphous layer with an average Ti₃₆Ni₆₄ composition is formed.

The results of the S-parameter measurements after annealing of the sample are shown in Fig. 5.2a. The effect of the annealing step is clearly visible in the positron energy interval ranging from 5 to 9 keV. Only

minor changes are observed for positron energies outside this interval indicating that the first Ni layer and the substrate remain unaffected on annealing. Analysing the data using eq. (5.1) gave satisfactory results if a decrease of the thickness of the Ti layer from 95 to 40 nm was assumed, accompanied by an increase of the S-parameter in the depth region ranging from 135 to 285 nm. The value of the S-parameter obtained for the newly formed zone lies between the S-parameter values of Ni and Ti. The values of the fitted parameters after annealing are summarized in Table 5.1. Both observations are consistent with the expected formation of an amorphous zone. The fact that a zone with an S-parameter value comparable with that of Ti is still present indicates that the interdiffusion is not fully completed. In addition, the data show that the first Ni/Ti internal interface remained inactive during the annealing. This might be due to oxidation of Ti at the top of the Ti layer caused by oxygen diffusing along the grain boundaries in the first Ni layer to the interface. The existence of a Ni layer between the amorphous zone and the substrate could not be confirmed within the experimental error.

CONCLUSION

It is shown that positron beam experiments are capable of monitoring interdiffusion processes. In this particular case it turned out to be possible to observe interdiffusion in a Ni/Ti/Ni multilayer structure at a depth of 200 nm below the surface. In addition, it is shown that the positions of the interfaces could be determined with an estimated accuracy of 10%.

It is confirmed that the first Ni/Ti internal interface remains unaffected on annealing at 525 K, probably due to the presence of an oxide layer at the top of the Ti layer.

5.3 Defect profiling of silicon MBE and SPE layers

ABSTRACT

Epitaxial layers of silicon grown on a Si(100) substrate by molecular beam epitaxy (MBE) and solid-phase epitaxy (SPE) have been investigated by variable energy positron beam analysis methods. Results of Doppler broadening measurements revealed that the S-parameter of the SPE material is considerably higher than the value measured for the MBE layer, indicative of a higher concentration of open-volume defects in the former material. This was confirmed by measurements of the positronium fraction at elevated temperatures.

INTRODUCTION

One of the major problems in molecular beam epitaxy of MBE silicon is the relatively poor control of dopant incorporation. At typical growth temperatures (900 - 1000 K) the *p*- and *n*-type dopants commonly used (Ga and Sb) have a strong tendency to segregate at the surface of the epitaxial film. This phenomenon causes smearing of sharp dopant profiles such as δ -doped layers¹. A solution to avoid this effect is deposition of amorphous Si at low temperatures (below 600 K) and subsequent recrystallization at typically 875 K. This so-called solid-phase epitaxy (SPE) yields crystalline Si films with expected higher impurity and defect concentrations than MBE material. Experimental techniques commonly used to reveal the presence of defects and impurities in semiconductors are defect etching and Rutherford Backscattering Spectroscopy (RBS). However, defect etching requires thick (1 μm) films, while RBS minimum yield measurements are not sensitive for the present defect concentrations.

A more sensitive probe for the assessment of MBE and SPE material is the positron annihilation (PA) technique². Moreover, the advent of variable energy positron beams has created the opportunity of implanting positrons in a controlled way in the near surface region of a material

and thus studying the defects in that region^{3,4}. A general review on variable energy positron beams and their applications is given in ref. 5. Here we present the results of Doppler broadening and Ps-fraction measurements on Si epitaxial layers prepared by MBE and SPE.

EXPERIMENTAL

SPE involved deposition at room temperature of amorphous Si followed by an annealing treatment at 830 K causing solid-phase epitaxial re-growth of the layer. During MBE the substrate was kept at 1000 K causing crystalline growth of the deposited layer. The layers were grown in a commercial MBE system (VG 80S, 6")⁶, with a base pressure of 5×10^{-9} Pa. During electron beam evaporation of Si at a growth rate of 3 Å/s the background pressure increased to 5×10^{-7} Pa, mainly due to H₂. The deposited layers consisted of intrinsic Si, whereas the Si substrate was either 0.02 Ωcm, Sb-doped (SPE) or a 20 Ωcm, B-doped (MBE) 4" wafer.

The variable energy positron beam (VEP) apparatus used in this study provided a beam of monoenergetic positrons with energies tunable from 100 eV to 30 keV. Adopting a power law dependence⁷ on the positron incident energy, this energy range corresponds to a positron mean implantation depths ranging from ~ 0 to 5 μm in Si. The intensity of the beam was estimated to be $\sim 10^4$ e⁺/s; the beam diameter was 8 mm at the sample surface.

Annihilation events were monitored with a Ge solid state detector placed behind the sample outside the vacuum system. The Doppler broadening of the annihilation peak was characterized by the S-parameter, defined as the area of a central region of the peak divided by the total area of the peak⁸. For each positron incident energy 5×10^5 counts were accumulated in the 511 keV annihilation peak.

The S-parameter is sensitive to the electron momentum distribution at the site of the positron and can be used to characterize the nature of the positron trapping site. By measuring the S-parameter as a function of the positron energy information can be obtained on the depth distribution of the defects.

Another way to detect the presence of defects is by measurement of

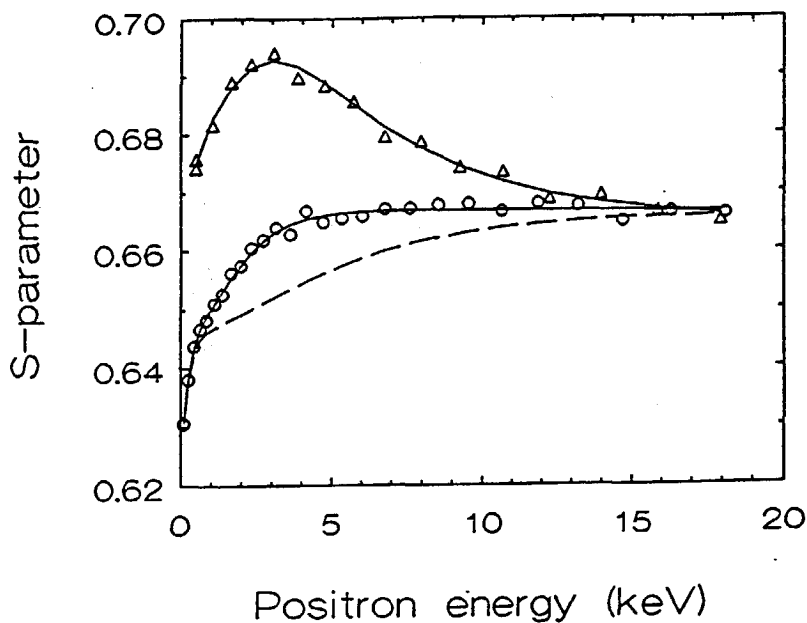


Fig. 5.3. The S-parameter *vs.* positron incident energy for the SPE (Δ) and MBE (\circ) grown Si epitaxial layers. The lines through the data are obtained with the fitting program VEPFIT. The dashed curve represents a model calculation of the S-parameter for defect-free and electric field-free Si.

the relative amount of positronium (Ps-fraction) formed at the sample surface, again as a function of the energy of the incoming positrons⁹.

For each positron energy, E , the fraction of positrons reappearing at the surface ($F_s(E)$), the fraction annihilating in the bulk ($F_b(E)$) and the fraction trapped at defects ($F_t(E)$) can be calculated from the balance between positron stopping, positron diffusion, bulk annihilation and trapping at defects by solving the time averaged, one dimensional steady state diffusion equation presented in chapter 2. For each positron energy the above mentioned fractions contribute to the measured value of $S(E)$,

$$S(E) = F_s(E)S_s + F_b(E)S_b + F_t(E)S_t \quad (5.2)$$

with S_s , S_b and S_t the S-parameters for positrons annihilating at the surface, in the bulk or at defects, respectively. The relative amount of Ps formed at the surface is proportional to F_s . The experimental data presented below are analysed with the modelling and fitting program called VEPFIT described in chapter 2.

RESULTS AND DISCUSSION

The S-parameter values measured as a function of the positron incident energy are shown in Fig. 5.3 for the SPE and MBE layers. Also shown is a calculated S-parameter curve representing defect-free and electric field-free Si. This curve is obtained with a value of 245 nm^4 for the positron diffusion length L_+ . The steep increase of the S-parameter at low positron energies (below 1 keV) reflects the effect of epithermal positron contributions. The data obtained for the SPE layer deviate the strongest from the calculated curve. For the MBE sample the deviations are less. The differences can be explained by assuming the presence of open-volume defects in the epitaxial layers. However, it must be noted that for the MBE sample the presence of an electric field directed towards the interface might explain the measured data as well⁴. Such a field can be the result of negative charges located at the interface due to the segregation of boron at that interface. In order to decide which model is applicable to the samples studied here, Ps-fraction measurements have been performed at a temperature of

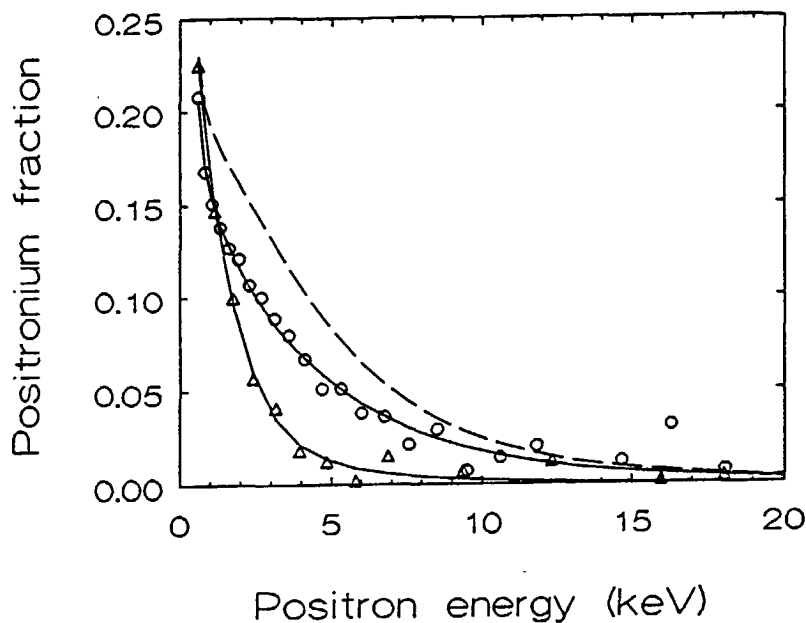


Fig. 5.4. The positronium fraction *vs.* positron incident energy for the SPE (Δ) and MBE (\circ) grown Si epitaxial layers. The measurements are performed at a sample temperature of 600 K. The lines through the data are obtained with the fitting program VEPFIT. The dashed curve represents a model calculation of the positronium fraction for defect-free and electric field-free Si.

600 K. At this temperature electric fields are strongly reduced because of thermally generated free carriers.

Together with the results of the Ps-fraction measurements depicted in Fig. 5.4 a calculated Ps-fraction curve for defect-free Si is shown, where we have taken into account a $T^{-0.5}$ temperature dependence of the positron diffusion coefficient¹⁰. At 600 K this corresponds to a reduced positron diffusion length of 206 nm. For both the MBE and SPE samples the measured Ps-fraction shows a stronger decrease with increasing positron energy compared with the defect-free material. In this case we can rule out the presence of electric fields, therefore we conclude that the effect is caused by trapping of positrons at defects in the epitaxial layers.

In order to make quantitative estimates of the observed trapping effects we have analysed the data using the program VEPFIT. In the model used the MBE and SPE layers were represented by overlayers with a fixed thickness of 150 nm and 200 nm, respectively. The value of the positron diffusion length in the substrate region was fixed to 245 nm. The measurements performed at 600 K were analysed with a value of 206 nm. In the overlayers and in the substrate the positron bulk annihilation rate, λ_b , was taken to be⁴ 4.5 ns^{-1} . The values of S_s , S_b and S_t as well as the effective diffusion length, $L_{+,eff}$, in the overlayers were obtained from least squares fits of the data.

In Figs. 5.3 and 5.4 the results of the fits are shown as solid lines. The fitted values of the parameters mentioned above are summarized in Table 5.2. The value of the epithermal positron scattering length¹¹, which accounts for the effect of epithermal contributions, was found to be 2 nm for both the S-parameter and the Ps-fraction measurements. This value was used for the calculation of the theoretical curves shown in the Figs. 5.3 and 5.4.

Though the difference between the measured S-parameter data of the MBE and SPE samples is obvious, the ratio S_t/S_b deduced from the fits was found to be ~ 1.05 for both samples. This value is characteristic for open-volume defects in Si. Comparable ratios have been reported for Si overlayers⁴ containing defects and Si irradiated with high energy ions³. Moreover, we observed a similar ratio for defects formed during the irradiation of Si with 30 keV helium ions (see next section of this chapter).

Table 5.2. Summary of fitted S-parameter values and effective diffusion lengths derived from S-parameter data (first 4 columns) and Ps-fraction data (last column) for the MBE and SPE samples.

sample	S_s	S_b	S_t	$L_{+,eff}^{a)}$ (nm)	$L_{+,eff}^{b)}$ (nm)
MBE	0.6456	0.6667	0.7075	120	125
SPE	0.6752	0.6643	0.6980	34	36

^{a)}measured at 300 K, fitted with $L_+ = 245$ nm.

^{b)}measured at 600 K, fitted with $L_+ = 206$ nm.

Assuming a uniform defect distribution in the overlayers, the positron trapping rate for defects, κ_t , is related to the effective positron diffusion length by

$$\kappa_t = \nu_t n_t = \lambda_b (L_+^2 / L_{+,eff}^2 - 1) \quad (5.3)$$

where ν_t is the specific positron trapping rate and n_t is the uniform defect density.

Adopting a specific positron trapping rate⁴ of $3 \times 10^{14} \text{ s}^{-1}$ we derived from the S-parameter data defect concentrations amounting to 7×10^{-4} and 5×10^{-5} atomic fraction (at. fr.) for the SPE and MBE layers, respectively. The defect concentrations derived from the Ps-fraction measurements were found to be 5×10^{-4} and 3×10^{-5} at. fr., respectively.

In Si mono-vacancies are mobile at room temperature, whereas di-vacancies, which are known to become mobile at 500 K¹², and small vacancy clusters would have been annealed out during processing of the layers (at 830 K for SPE and at 1000 K for MBE). We therefore conclude that the observed positron trapping is caused by small voids, dislocations or stacking faults.

The minimum yield, χ_{min} , derived from RBS measurements was found to be 3.1 %, a value comparable to what is usually obtained for defect-free crystalline Si. The minimum yield is defined as the ratio of the yield of backscattered probing particles when the sample is aligned along a channeling direction and the yield under random incidence.

Given the defect concentrations obtained from the positron beam measurements this is not a surprising result, as for displaced atoms the

sensitivity of the RBS technique is of the order of 10^{-3} at. fr., whereas for open-volume defects like vacancies and vacancy clusters this technique is almost insensitive. Of more interest is the fact that with the positron annihilation technique additional information can be obtained on the quality of epitaxial layers, particularly with respect to open-volume defects which remain unnoticed with standard RBS techniques.

CONCLUSIONS

In conclusion, the present study has shown that a variable energy positron beam is a sensitive tool for measuring differences in open-volume defect concentrations between MBE and SPE grown epitaxial films. Doppler broadening and Ps-fraction measurements indicated a ten times higher defect concentration in the SPE material than in the MBE material, not detectable by standard RBS minimum yield analysis.

In addition, the Doppler broadening technique yields a parameter, S_t/S_b , which bears information on the nature or size of the defects present. In the cases studied here the value of S_t/S_b roughly points to small voids or dislocations. In order to be able to give a more exact description of the nature of the defects further comparative studies must be performed to establish a catalog of S_t/S_b values for different type of defects.

5.4 Helium implanted silicon

INTRODUCTORY REMARKS

An important feature of positron beams is its sensitivity for vacancy type defects as has been demonstrated in the previous sections. In this section an example will be given of defect analysis for the case of helium implanted silicon. The analysis formed part of a study on bubble formation and swelling phenomena in noble gas ion irradiated silicon. Helium desorption measurements and TEM observations have revealed that helium-vacancy complexes are created which grow in size with increasing helium concentration¹.

An unusual phenomenon was observed when helium irradiated silicon was annealed to temperatures higher than 1250 K. It appeared that helium was detrapped from the formed bubbles resulting in emptied bubble volumes or voids². This finding has triggered further research on the possibility for formation of "buried" porous layers in silicon which could form the starting point for the formation of buried oxide layers by applying oxidation techniques to the pre-treated material.³.

Swelling measurements and SEM observations on cross-sections of helium irradiated silicon samples (Si(100)-wafers) have shown that beyond a critical helium dose ($2 \times 10^{17} \text{ He}^+ \text{ cm}^{-2}$ for 30 keV He) helium bubbles start to coalesce thereby forming large cavities. In a final stage blister domes develop on the surface, which, driven by the helium gas pressure, grow to macroscopic hemispheres.

The present positron beam study aimed at following the evolution of the damage created during helium irradiation of Si from low helium doses through the critical dose up to a high dose.

EXPERIMENTAL

The positron beam measurements were performed using the variable energy positron beam described in this thesis. The helium implantations were carried out with an ion accelerator capable of providing ion beams with energies tunable from 10 keV to 30 keV. The ions were generated in a Danfysik-duoplasmatron ion source. Mass selection of

the ion beam was achieved with a 90° double focussing magnet with a mass resolution, $M/\Delta M$, of 250. Along the beam line deflection plates were mounted for horizontal and vertical deviation of the beam. Furthermore, two pairs of deflection plates were installed used to sweep the beam in horizontal and vertical direction in order to obtain a uniform irradiation of the sample surface over an area of $10 \times 10 \text{ mm}^2$. With this setup a He^+ current density of $1 \mu\text{A cm}^{-2}$ could be reached.

The silicon samples used in this study were cut from a Si(100) *n*-type, wafer (P-doped) produced by Float Zone (FZ) melting. The resistivity of the silicon material was $0.9 \Omega\text{.cm}$.

Four samples were implanted with 30 keV He ions with total He doses of 1.0×10^{16} , 5.0×10^{16} , 1.0×10^{17} and $5.0 \times 10^{17} \text{ He cm}^{-2}$, respectively. The temperature increase of the samples during the implantation was less than 10°C . After the implantations the samples were mounted in the sample chamber of the variable energy positron beam. The Doppler broadening of the 511 keV annihilation line was monitored as a function of the positron incident energy up to a maximum of 20 keV. 5×10^5 counts were accumulated in the 511 keV annihilation peak for each incident energy.

Swelling of the sample surface after He implantation has been monitored with a so called Alpha Step instrument. These measurements have been carried out on an additional set of Si samples implanted with 30 keV He^+ ions with He doses varying from 1.0×10^{16} to $9.0 \times 10^{17} \text{ He cm}^{-2}$. In order to improve the contrast in height of the irradiated and unirradiated surface area a Mo mask with rectangularly shaped slits ($0.17 \times 5.0 \text{ mm}^2$) was placed in front of the sample surface. With this method a swelling of the irradiated area could be observed down to 2.5 nm.

RESULTS

Figs. 5.5a and 5.5b show Scanning Electron Microscopy (SEM) pictures taken from a cleaved Si(100) sample irradiated with 30 keV He^+ ions with a total He dose of $9.0 \times 10^{17} \text{ He cm}^{-2}$. Fig. 5.5a shows that at this dose level the subsurface cavities have grown to considerable sizes. Fig. 5.5b shows that blister domes have been formed which are

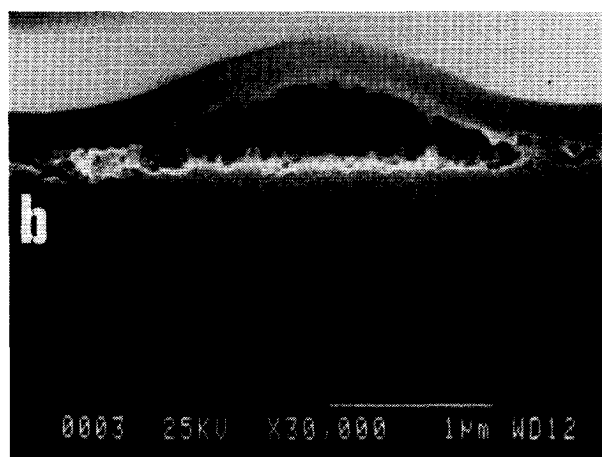
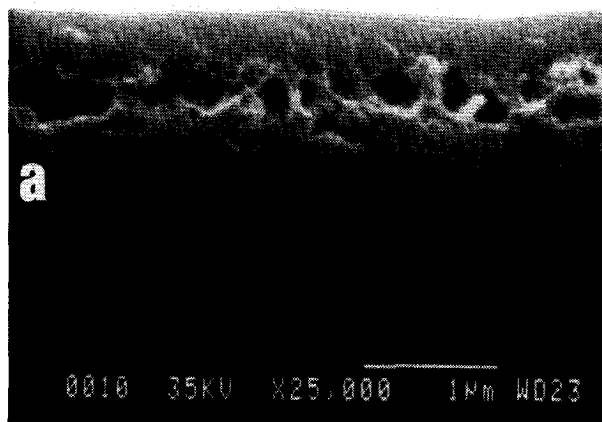


Fig. 5.5. SEM pictures taken from a cleavage surface of a Si sample irradiated with 30 keV, $9.0 \times 10^{17} \text{ He}^+ \text{ cm}^{-2}$. a) subsurface cavities: b) blister dome.

apparently the result of a local decohesion of the top layer followed by plastic deformation of the blister cap under the action of lateral stresses in the top layer driven by the pressure of the He gas accumulated in the blister volumes.

In Fig. 5.6 the S-parameter data measured as a function of the positron energy are shown for the four He irradiated samples. Also shown are the S-parameter data measured for a virginal Si sample. It is observed that with increasing He dose the effect of the irradiation on the S-parameter becomes more pronounced due to the trapping of positrons at the defects created during the irradiation. The maxima in the measured S-parameter data have a tendency to shift to lower positron incident energy with increasing He dose. However, for the highest He dose the maximum shifts to higher positron energies.

The results of the swelling measurements are shown in Fig. 5.7 where the swelling of the irradiated surface area is plotted *vs.* the implanted He dose. The solid lines represent the expected swelling when the indicated number of vacancy volumes per implanted He ion is adopted. Note that the swelling per He ion increases strongly for a He dose higher than 2.0×10^{17} He cm⁻².

DISCUSSION

The Doppler broadening measurements have been analysed using the modelling and fitting program VEPFIT presented in chapter 2. It was found that the measured data could be fitted adequately when model #4 was applied (fitting of a layered structure with S-parameters adapted for positrons annihilating at defects and in the bulk material). For the three lowest He doses the assumption of one layer containing the defects and a second layer representing the bulk material was sufficient to obtain a good fit. Introducing more layers yielded S-parameters for the different layers comparable with the S-parameter obtained for the case of one layer. Moreover, the positions of the boundaries separating the extra layers were found to have a large statistical spread. Only in case of the highest He dose the introduction of a second layer was necessary in order to obtain a good fit. In addition the diffusion length in the depth region beyond the second layer was observed to

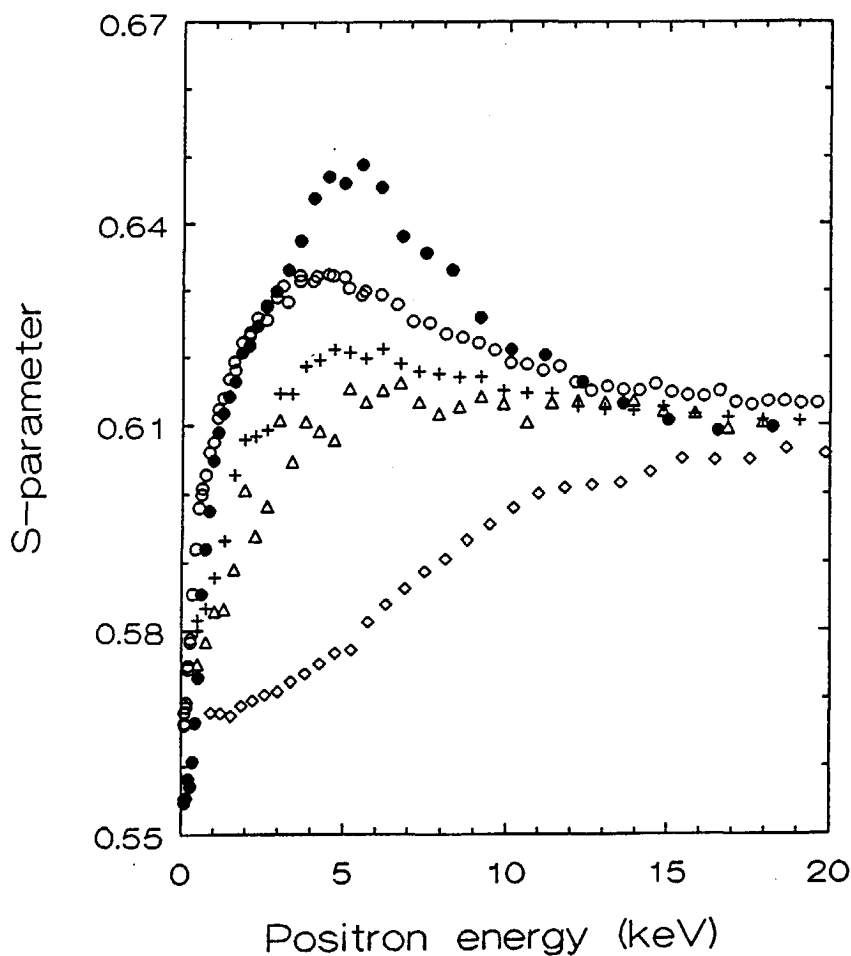


Fig. 5.6. Experimental S-parameter values *vs.* positron incident energy for: (Δ) $1.0 \times 10^{16} \text{ He}^+ \text{ cm}^{-2}$; (+) $5.0 \times 10^{16} \text{ He}^+ \text{ cm}^{-2}$, (\circ) $1.0 \times 10^{17} \text{ He}^+ \text{ cm}^{-2}$, (\bullet) $5.0 \times 10^{17} \text{ He}^+ \text{ cm}^{-2}$ and (\diamond) a virginal Si sample.

decrease from 223 to 122 nm. The position of the boundary separating this region from the second layer could not be determined with high accuracy. The relevant fitted parameters (S_b , S_l , the position of the boundaries z_l , the effective diffusion length in the layers $L_{+,eff}$ and the positron defect trapping rate, κ_l derived from the latter) are summarized in Table 5.3. For the positron implantation profile the derivative of a gaussian is used with the parameters describing the shape of the profile given in chapter 2. The values of the positron diffusion coefficient, D_+ and the bulk annihilation rate, λ_b , were taken $2.8 \text{ cm}^2\text{s}^{-1}$ and $4.5 \times 10^9 \text{ s}^{-1}$, respectively^{4,5}. In the Figs. 5.8a-d the experimentally obtained data with the corresponding fits are shown separately. Note that the depths of the boundaries derived from the positron beam measurements are not influenced by the swelling of the material. This is due to the fact that the stopping of the positrons depends on the areal density of the material, i.e. the product of the density and depth over which the positrons are implanted.

In order to interpret the positron beam results the depth distribution of 30 keV He ions and the distribution of displaced Si atoms have been calculated. Fig. 5.9 shows the results of TRIM calculations for 30 keV, $5 \times 10^{17} \text{ He cm}^{-2}$ incident on Si. It is seen that the distribution of He extends up to a depth of 400 nm with a maximum concentration at a depth of $\sim 300 \text{ nm}$.

The calculated distribution of displaced Si atoms (Frenkel pairs) per He atom at a temperature of 0 K (no recombination processes) is shown in Fig. 5.10 for a He implantation energy of 30 keV. Based on a threshold displacement energy of 25 eV the average number of Frenkel pairs created per incident He ion amounts to about 60. At room temperature both the vacancies and the self-interstitials are very mobile and therefore a high recombination rate is expected. From the swelling measurements it appears that for the low dose irradiations at room temperature about 0.7 vacancies per He ion survive. Adopting an average volume of $2 \times 10^{-2} \text{ nm}^3$ per mono-vacancy in Si results in a He density in the vacancies and vacancy clusters of about $7 \times 10^{22} \text{ He cm}^{-3}$, corresponding with a helium pressure of the order of 1 GPa. By comparing the He distribution and the distribution of the displaced Si atoms it can be expected that the degree of helium filling of the vacancies and vacancy clusters varies with depth. The filling will have

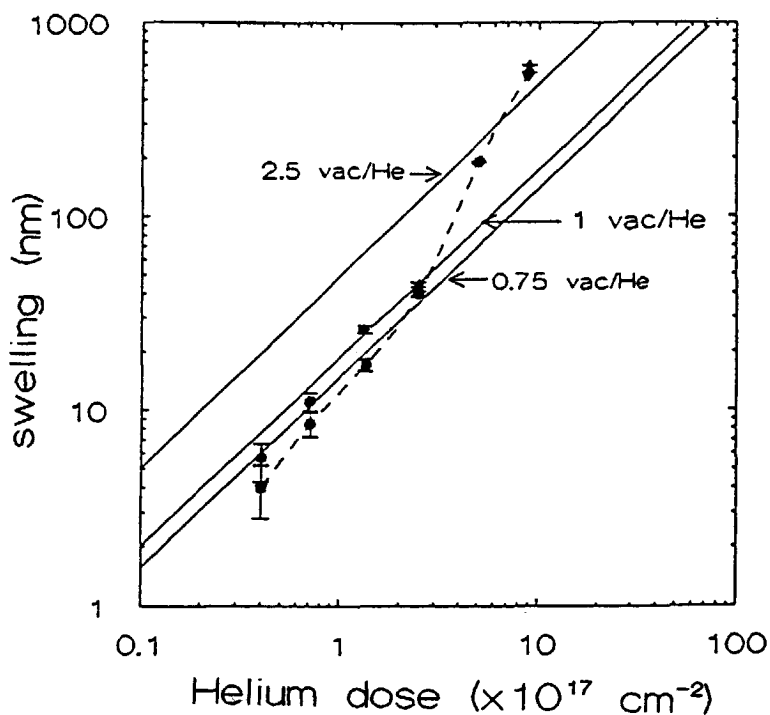


Fig. 5.7. Swelling of the Si sample surface as a function of the implanted He dose. The solid lines represent the expected swelling when the indicated number of vacancy volumes produced per He^+ ion is adopted.

its maximum value at a depth corresponding to the depth at which the He concentration reaches its maximum.

From the observed swelling of 10 nm at a He dose of $1 \times 10^{16} \text{ cm}^{-2}$ we derive a depth averaged defect concentration of 3×10^{-2} defects per Si atom if mono-vacancies are assumed. This number must be compared with the defect concentration derived from the positron measurements. For the low dose irradiated sample the positron trapping rate in defects was found to be $2 \times 10^{10} \text{ s}^{-1}$ (with a specific positron defect trapping rate⁶ of the order of 10^{14} s^{-1}) which yields a uniform defect density of 2×10^{-4} defects per Si atom. This value is two orders of magnitude lower than the one derived from the swelling measurements. The same can be stated for the higher dose implantations.

A second remarkable feature is the fact that for the three lowest He implantation doses the measured S-parameter curves can be described by assuming a single layer containing defects with an S-parameter for the trapped positrons of 0.634. Besides this it is found that the width of the layer (285 - 320 nm) is comparable with the range over which the implanted helium and the remaining defects (di-vacancies and He-vacancy complexes) are distributed. The latter result forms an indication that the damage caused by the He implantation is probed.

Only for the highest He dose there is strong evidence for the formation of a second layer at a depth between 150 and 300 nm with a much higher characteristic S-parameter and a strongly reduced diffusion length. The latter effect can be related to the formation of a porous layer containing large cavities with clean inner surfaces and a reduced He pressure. The high value of the S-parameter in this layer reflects the annihilation of positrons bound at the inner surfaces or the formation of free positronium in the cavity. It is observed by Schultz et al.⁶ that the S-parameter associated with positrons diffusing to the vacuum/Si interface increases when the surface is cleaned.

What remains is the difference between the defect concentration derived from the swelling and positron beam measurements. A possible explanation for this discrepancy is a reduced trapping rate for positrons into defects containing highly pressurized He gas. Under this assumption the observed positron trapping is ascribed to defects containing helium gas under low pressure. In addition this would account for the ratio $S_t/S_b \sim 1.04$ found for the three lowest He doses, which is typical

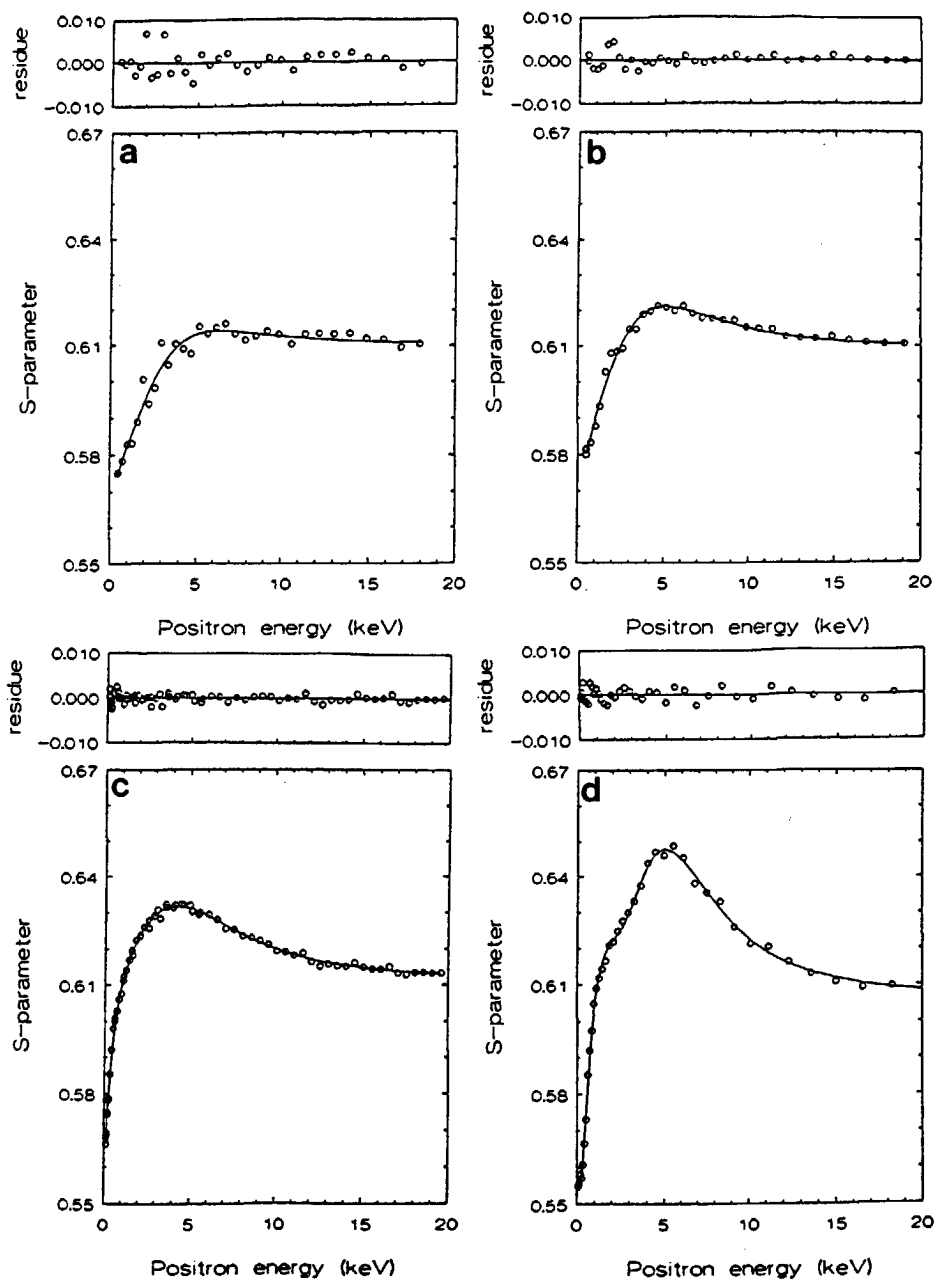


Fig. 5.8. Experimental and fitted S-parameter values vs. positron incident energy for: (a) $1.0 \times 10^{16} \text{ He}^+ \text{ cm}^{-2}$, (b) $5.0 \times 10^{16} \text{ He}^+ \text{ cm}^{-2}$, (c) $1.0 \times 10^{17} \text{ He}^+ \text{ cm}^{-2}$ and (d) $5.0 \times 10^{17} \text{ He}^+ \text{ cm}^{-2}$.

Table 5.3. Fitted values of S-bulk, S_b , S-defect, S_t , layer boundary position, z_l , effective diffusion length, $L_{+,eff}$, and trapping rate, κ_l , for helium implanted silicon.

dose (He.cm ⁻²)	S_b	S_t	z_l (nm)	$L_{+,eff}$ (nm)	κ_l (s ⁻¹)
1.0×10^{16}	0.610	0.634	280	98	2.0×10^{10}
5.0×10^{16}	0.609	0.634	285	66	5.0×10^{10}
1.0×10^{17}	0.611	0.636	322	37	1.6×10^{11}
5.0×10^{17} 1 st layer	0.606	0.625	156	10	2.0×10^{14}
2 nd layer	0.606	0.669	283	~ 0	$\sim 10^{16}$

for positrons trapped at small open-volume defects in Si.

Another aspect of interest to the positron studies described here is the influence of the He density in the vacancy clusters on the annihilation properties of the trapped positrons. For He bubbles in metals⁷ it has been found that with increasing He density the positron lifetime decreases to a value close to the lifetime of positrons in the virginal metal. It might be expected that for Si, where a positron trapped in a mono-vacancy has a partly delocalized character (i.e. a considerable overlap of the positron wave function with the valence electrons of the bulk material), a vacancy or a vacancy cluster highly filled with helium may lead to an even more delocalized character. This results in an S-parameter for trapped positrons approaching the S-parameter of positrons annihilating in the bulk of Si. In this case it is difficult to distinguish between positrons annihilating in a trapped state and those annihilating in a delocalized or free state. In order to verify the above assumptions further studies have to be carried out.

CONCLUDING REMARKS

We have reported on a positron beam study which aimed at following the evolution of the damage created in Si caused by the irradiation with 30 keV He ions with doses varying from 1.0×10^{16} to 5.0×10^{17} He cm⁻². The formation of a zone containing large cavities at a depth between 150 nm and 300 nm after irradiation to a dose level of 5.0×10^{17} He

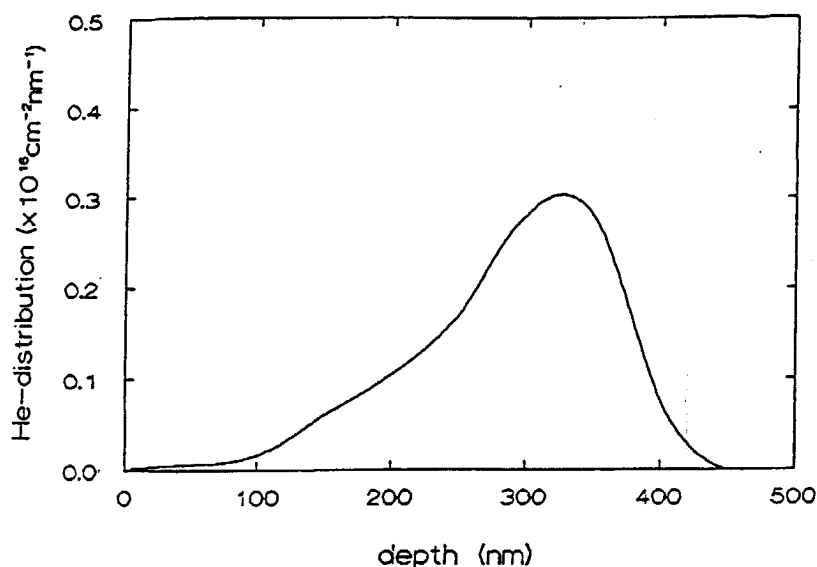


Fig. 5.9. The He concentration *vs.* depth in Si calculated with TRIM for 30 keV, $5.0 \times 10^{17} \text{ He}^+ \text{ cm}^{-2}$.

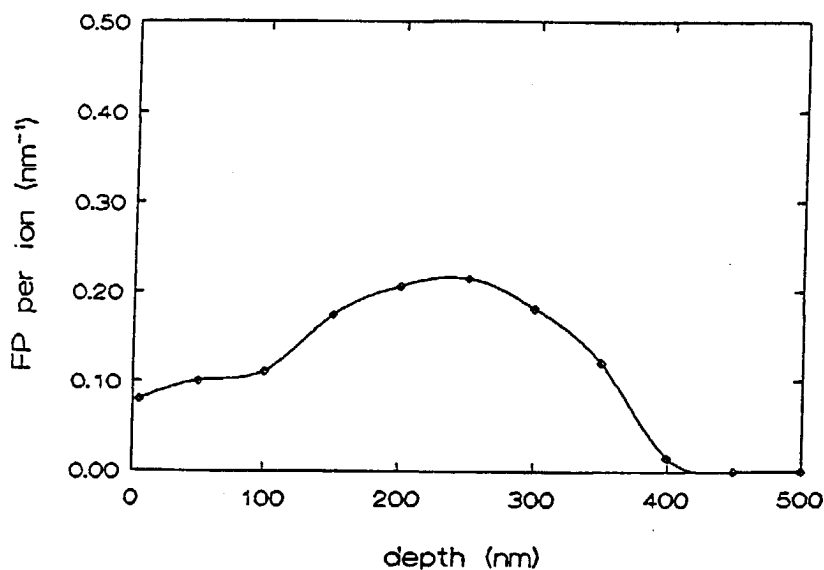


Fig. 5.10. The distribution of Frenkel pairs (FP) in Si calculated with TRIM for 30 keV He^+ ions incident on Si (random orientation) at 0 K. The total number of Frenkel pairs created per He ion (depth integrated) is about 60.

cm^{-2} has been established in accordance with results of swelling measurements and SEM observations. The depth region in which the presence of defects (presumably di-vacancies and small He-vacancy clusters) was detected corresponds fairly well with the calculated spatial distribution of displaced Si atoms and 30 keV implanted He ions. No direct relation is found between the defect density obtained from the positron beam measurements and the defect density derived from swelling measurements. This discrepancy has been attributed to a reduced trapping rate for positrons in defects containing highly pressurized He.

5.5 Evaluation

In this section an evaluation will be given on the ability of the Delft Variable Energy Positron beam facility as a tool of interest in the field of materials research. Examples of positron beam studies performed on different materials such as metals, semiconductors and layered structures have been presented in chapter 4 and in this chapter.

In chapter 4 it has been shown that measurements of the fraction of positrons reappearing at the surface of incidence under different experimental conditions, yield information on the branching of positrons at surfaces. This information is not only of importance for an accurate determination of defect distributions in the near surface region of solids, but is also valuable for the characterization of the surface itself. The fact that the branching of positrons into the various positron states depends strongly on the condition of the surface offers the possibility to use positron beams as a sensitive surface probe for measuring the positron surface potential. With respect to the development of moderators with high moderation efficiencies the results of this technique can be very helpful.

In the previous sections of this chapter examples of positron beam depth profiling studies have been presented. It has been shown that by monitoring the variation of the S-parameter as a function of the positron energy the position of the interfaces in a multilayer system could be determined up to a depth of several 100 nm with an accuracy of 10%. In addition it turned out to be possible to detect changes in composition of the constituent materials at this depth. A requirement

for a successful application of this technique is that the structure is composed of materials with different values of the S-parameter.

For the case described here it was established that the diffusion of positrons was strongly reduced due to a high concentration of positron trapping sites. Though this facilitates the interpretation of the measured data it inhibits the study of the properties of the interface. The study of interfaces is possible whenever implanted positrons are allowed to diffuse towards the interface. In this case changes in the properties of the interface can be detected by monitoring variations of the S-parameter of positrons annihilating at the interface.

The experiments performed on the epitaxial Si layers grown on a Si(100) substrate illustrate the sensitivity of the positron annihilation technique to open-volume defects in Si. In particular it has been shown that defect density levels can be detected which remain unnoticed by standard RBS techniques. The nature of the defects probed could not be determined fully, though the value of the S-parameter associated with the defects points to small voids or dislocations.

In the last example it has been shown that the positron beam technique can be used to study the evolution of damage caused by implantation of energetic ions. The formation of large cavities in Si irradiated with 30 keV He-ions could be detected by monitoring the behaviour of the S-parameter as a function of the implanted He dose. By measuring the S-parameter as a function of the positron incident energy the depth at which the cavities were formed could be established.

Although still preliminary, the studies described above demonstrate that the positron beam analysis technique forms a promising tool for the investigation of a variety of problems in materials science. With this non-destructive technique it is possible to probe defect structures up to a depth of several microns with a depth resolution of $\sim 10\%$. The sensitivity of the technique allows the study of defect concentration levels down to 10^{-5} atomic fraction. A particularly promising area for investigation with variable energy positrons is that of damage introduced in semiconductors and oxide-semiconductor systems during ion-beam modification or epitaxial layer growth. In addition the technique is found to be sensitive to the presence of electric fields in these materials. It is known that electric field strengths down to 10^5 V.m^{-1} can be detected.

There are a variety of other research areas involving variable energy positron beams which have only just been initiated. Examples of these are the recently developed positron lifetime techniques utilizing pulsed positron beams and positron micro-beams which have applications to imaging studies of near surface and interfacial defects.

References section 5.2

1. M.A. Hollanders and B.J. Thyse, *J. Less Common Metals*, **140**, 33, (1988).
2. A. Vehanen, K. Saarinen, P. Hautojärvi and H. Huomo, *Phys. Rev. B* **35**, 4606, (1987).
3. I.K. McKenzie, in *Positron Solid State Physics*, Proc. of the 83rd Int. School of Physics 'Enrico Fermi', eds. W. Brandt and A. Dupasquier, (North Holland, Amsterdam, 1983).

References section 5.3

1. A.A. van Gorkum, K. Nakagawa and Y. Shiraki, *J. Cryst. Growth* **95**, 480, (1989).
2. R.N. West, in *Positrons in Solids*, ed. P. Hautojärvi, (Springer, Berlin, 1979) p. 89.
3. J. Keionen, M. Hautala, E. Rauhala, M. Erola, J. Lahtinen, H. Huomo, A. Vehanen and P. Hautojärvi, *Phys. Rev. B*, **36**, 1344, (1987).
4. P.J. Schultz, E. Tandberg, K.G. Lynn, B. Nielsen, T.E. Jackman, M.W. Denhoff and G.C. Aers, *Phys. Rev. Lett.* **61**, 187, (1988).
5. P.J. Schultz and K.G. Lynn, *Rev. Mod. Phys.* **60**, 701, (1989).
6. A.A. van Gorkum, G.F.A. van der Walle, R.A. van den Heuvel, D.J. Gravesteyn and C.W. Frederiksz, *Thin Solid Films*, in press.
7. A.P. Mills and R.J. Wilson, *Phys. Rev. A* **26**, 490, (1982).
8. K.G. Lynn and D.O. Welch, *Phys. Rev. B* **22**, 99, (1980).
9. H. Huomo, A. Vehanen, M.D. Bentzon and P. Hautojärvi, *Phys. Rev. B* **35**, 4606, (1987).
10. D.T. Britton, P.C. Rice-Evans and J.H. Evans, *Phil. Mag. Lett.* **57**, 165, (1988).
11. J.C. Bourgoin and M. Lannoo, eds. *Point defects in semiconductors II*, (Springer, Berlin, 1983).

References section 5.4

1. A. van Veen, P.C. de Jong, K.R. Bijkerk, H.A. Filius and J.H. Evans, in *Fundamentals of Beam-Solid Interactions and Transient Thermal Processing*, eds. M.J. Aziz, L.E. Rehn and B. Stritzker, Proc. Mat. Res. Soc. **100**, (MRS, Pittsburg, Pennsylvania, 1988), p.231.
2. A. van Veen, C.C. Griffioen and J.H. Evans, in *Silicon on Insulator and Buried Metals in Semiconductors*, eds. J.C. Sturm, C.K. Chen, L. Pfeiffer and P.L.F. Hemment, Proc. Mat. Res. Soc. **107**, (MRS, Pittsburg, Pennsylvania, 1988), p.449.
3. A.H. van Ommen, in *Silicon on Insulator and Buried Metals in Semiconductors*, eds. J.C. Sturm, C.K. Chen, L. Pfeiffer and P.L.F. Hemment, Proc. Mat. Res. Soc. **107**, (MRS, Pittsburg, Pennsylvania, 1988), p.43.
4. B. Nielsen, K.G. Lynn and A. Vehanen, Phys. Rev. B **32**, 2296, (1985).
5. S. Dannefaer, G.W. Dean, D.P. Kerr and B.G. Hogg, Phys. Rev. B **14**, 2709, (1976).
6. P.J. Schultz, E. Tandberg, K.G. Lynn, B. Nielsen, T.E. Jackman, M.W. Denhoff and G.C. Aers, Phys. Rev. Lett. **61**, 187, (1988).
7. R.M. Nieminen, in *Positron Annihilation*, Proc. of the 8th Int. Conf. on Positron Annihilation, eds. L. Dorikens-Vanpraet, M. Dorikens and D. Segers, (World Scientific, Singapore, 1989), p.60.
8. B. Nielsen, K.G. Lynn, D.O. Welch, T.C. Leung and G.W. Rubloff, Phys. Rev. B **40**, 1434, (1989).

Summary

A new development in the field of materials research with positrons is that of variable energy positron beams. The motivation for the development of positron beams lies in the successful application of conventional positron annihilation techniques to defect studies in solid materials. One of the main advantages of the positron beam technique is obviously its potential to probe the spatial distribution of lattice disorder, especially in the near surface region of a solid, which is not possible with the conventional positron annihilation technique. Although the positron beam technique is rather new, current research indicates that it may develop into an effective tool for studying not only defects but also surfaces and internal interfaces. Moreover, due to the positron's positive charge, the technique is sensitive to electric charges which enables the study of electric fields and charged defect states in semiconductors.

The work described in this thesis relates to the development of a variable energy positron beam facility designed for application in materials science. In addition several studies have been carried out in order to explore the capabilities of the positron beam technique.

After an introductory chapter 1, chapter 2 describes the theory of positron implantation, diffusion and trapping in materials. A computer program called VEPFIT is presented for the analysis and modelling of positron beam experimental data. With the help of simulated data it is shown that the program can be used for the analysis of a wide variety of depth profiling problems.

In chapter 3 the design of the Delft positron beam facility is presented. Mono-energetic positrons are produced by the moderation of fast positrons from a ^{22}Na source in an annealed poly-crystalline tungsten foil with an efficiency of 2×10^{-4} . Transport of moderated positrons is achieved by an axial magnetic field produced by coils in a Helmholtz configuration. The energy spread of the beam is about 4 eV. The energy of the beam can be varied from 100 eV to 30 keV. The overall performance of the setup allows the study of the near surface region of solids in an UHV environment.

In chapter 4 the branching of positrons into the different states at the surface is studied. With the aid of a for this purpose developed experimental method it was found that the condition of the surface has a strong effect on the branching of positrons. By carefully accounting for the branching of positrons and by combining Doppler broadening and Ps-fraction methods the defect distribution in Mo implanted with 3 keV He-ions could be assessed.

Finally, in chapter 5 the results of positron beam experiments performed with the Delft variable energy positron beam are presented. A Doppler broadening study has been carried out on a Ni/Ti/Ni multilayer structure. The positions of the internal interfaces could be determined and the formation, after annealing at 525 K, of an alloyed Ni-Ti zone was observed. Furthermore, it was confirmed that the Ni/Ti interface closest to the surface remained unaffected on annealing, probably due to an oxide layer on top of the Ti layer.

Measurements on MBE and SPE silicon layers grown on a Si substrate show that the positron beam technique can yield valuable information about the quality of epitaxial semiconductor layers. The concentration of open-volume defects in the SPE layer was found to be 10 times higher than in the MBE layer. These defects remained unnoticed by RBS techniques.

A positron beam experiment aimed at following the evolution of damage created in Si during 30 keV helium implantation confirmed the formation of large cavities at high He dose levels. By using the modelling and fitting program VEPFIT it was possible to establish the depth at which these cavities develop.

Samenvatting

Een nieuwe ontwikkeling op het vlak van het materiaalonderzoek met positronen is die waarbij gebruik wordt gemaakt van positronenbundels met variabele energie. De reden voor de ontwikkeling van positronenbundels komt voort uit de succesvolle toepassing van de konventionele positronannihilatietechniek in het schadeonderzoek in materialen. Een van de voordelen van de positronenbundeltechniek is de mogelijkheid om de diepteverdeling van roosterverstoringen af te tasten, voornamelijk in een laag dicht onder het oppervlak, hetgeen met de konventionele positronannihilatietechniek niet mogelijk is. Hoewel de positronenbundeltechniek betrekkelijk jong is, heeft recent onderzoek aangetoond dat deze techniek zich kan ontwikkelen tot een effectieve meetmethode voor het onderzoek naar defekten, oppervlakken en inwendige grensvlakken. Bovendien draagt de positieve lading van het positron er toe bij dat de techniek gevoelig is voor elektrische ladingen hetgeen onderzoek naar elektrische velden en elektrisch geladen defekten in halfgeleidermaterialen mogelijk maakt.

Het in dit proefschrift beschreven werk heeft betrekking op de ontwikkeling van een positronenbundelfaciliteit ontworpen voor toepassing in het materiaalonderzoek. Tevens zijn een aantal studies uitgevoerd om de toepasbaarheid van de positronenbundeltechniek te exploreren.

Na een inleidend hoofdstuk, wordt in hoofdstuk 2 de theorie betreffende de implantatie, de diffusie en de vangst van positronen in materialen behandeld. Een komputer programma genaamd VEPFIT wordt beschreven dat gebruikt wordt voor de analyse en het modelleren van experimenteel verkregen positronenbundelresultaten. Aan de hand van kunstmatig gegenereerde resultaten is aangetoond dat met behulp van dit programma een verscheidenheid aan diepteprofielmetingen kan worden geanalyseerd.

In hoofdstuk 3 wordt het ontwerp van de positronenbundelfaciliteit gepresenteerd. Mono-energetische positronen worden verkregen door snelle positronen, uitgezonden door een ^{22}Na bron, te modereren in een poly-kristallijn wolfrام folie. Het rendement van het moderatie proces is 2×10^{-4} . Het transport van de gemodereerde positronen geschiedt door middel van een axiaal magnetisch veld dat wordt opgewekt door

spoelen in de Helmholtz configuratie. De spreiding in bundelenergie bedraagt ongeveer 4 eV. De energie van de positronenbundel kan worden gevarieerd tussen 100 eV en 30 keV. De werking van de opstelling als geheel is zodanig dat het mogelijk is oppervlaktelagen te bestuderen onder UHV condities.

In hoofdstuk 4 wordt de opsplitsing van positronen in verschillende toestanden aan het oppervlak beschouwd. Met behulp van een hiertoe ontwikkelde meetmethode is vastgesteld dat de konditie van het oppervlak van invloed is op de opsplitsing van positronen. Gebruik makend van zowel de dopplerverbreidings- als de Ps-fractiemethode en rekening houdend met de opsplitsing van positronen kon de verdeling van defekten in Mo na beschieting met 30 keV He-ionen worden vastgesteld.

Tenslotte worden in hoofdstuk 5 de experimenten besproken die zijn uitgevoerd met de delftse variabele energie positronenbundel. Een Ni/Ti/Ni meerlaags systeem is bestudeerd met behulp van de dopplerverbreidingsmethode. De posities van de grensvlakken konden worden bepaald en de vorming, na verhitting tot 525 K, van een laag bestaande uit een Ni-Ti legering is waargenomen. Bovendien is bevestigd dat het grensvlak dat zich het dichtst bij het oppervlak bevindt geen verandering heeft ondergaan tijdens de verhitting, waarschijnlijk als gevolg van de aanwezigheid van een oxidelaag aan het oppervlak van de Ti-laag.

De metingen uitgevoerd aan MBE en SPE siliciumlagen aangebracht op een Si-substraat tonen aan dat met behulp van de positronenbundeltechniek informatie verkregen kan worden over de kwaliteit van epitaxiaal gegroeide halfgeleiderlagen. De concentratie van defekten met een open structuur in de SPE-laag bleek tienmaal hoger te zijn dan die in de MBE-laag. Deze defekten konden niet worden waargenomen met RBS technieken.

Een positronenbundelexperiment gericht op het volgen van de evolutie van de schade veroorzaakt tijdens de beschieting van Si met 30 keV He-ionen, bevestigde de vorming van grote holten bij beschieting met een hoge dosis He. Gebruik makend van het modellerings- en fitprogramma VEPFIT kon de diepte waarop zich de holten vormen, worden vastgesteld.

Nawoord

Op deze plaats wil ik allen bedanken die hebben bijgedragen aan het totstandkomen van dit proefschrift. Allereerst wil ik mijn promotor Prof. Dr. Ir. H. van Dam danken voor de mogelijkheid die hij mij geboden heeft om het promotieonderzoek uit te voeren.

Dr. A. van Veen ben ik zeer erkentelijk voor de intensieve dagelijkse begeleiding en de stimulerende discussies..

Tevens ben ik dank verschuldigd aan mijn kollega's die zich met enthousiasme hebben ingezet bij het onderzoek en die mij terzijde hebben gestaan met adviezen op velerlei gebied.

Jan de Roode en Dick de Haas dank ik voor het ontwerpen en bijebrengen van de electronische apparatuur en het professioneel repareren daarvan wanneer het natuurgeweld weer eens toesloeg. Bob Heijenga en Kees Westerduin hebben getracht mij enige kennis op het gebied van de vacuümtechniek bij te brengen. Maurits IJpma bedank ik voor zijn hulp bij het programmeren en het uitvoeren van de berekeningen. De assistentie van Karl Roos bij het ontwerpen, bouwen en het in bedrijf houden van de opstelling is door mij zeer gewaardeerd.

Johan de Vries heeft een grote bijdrage geleverd aan de ontwikkeling van het modellerings- en fitprogramma. Rudi Hakvoort dank ik voor het opsporen van de onvolkomenheden in de tekst en voor de typografische adviezen. De discussies met Hans Filius heb ik altijd als zeer prettig ervaren.

Mijn dank gaat verder uit naar de medewerkers van de werkplaatsen van het IRI en de faculteit der Technische Natuurkunde die bij het ontwerp en de bouw van de apparatuur betrokken zijn geweest.

Voorts wil ik alle - niet met name genoemde - leden van de afdeling Reactor Fysica bedanken voor de prettige werkomgeving.

Tot slot wil ik jou, Carin, bedanken voor de steun die je voor mij geweest bent bij het schrijven van dit proefschrift. Jouw relativeringsvermogen bleek sterker dan alle leeuwen en beren op mijn weg.

Henk

Curriculum vitae

De schrijver van dit proefschrift werd geboren op 29 juni 1958 te Apeldoorn. Na een aantal instellingen voor het middelbaar onderwijs te hebben bezocht werd in 1977 het VWO-diploma behaald aan de Koninklijke Scholen Gemeenschap te Apeldoorn. In datzelfde jaar werd begonnen met de studie natuurkunde aan de Rijksuniversiteit Utrecht. In 1985 werd het doctoraaldiploma experimentele natuurkunde met bijvakken wiskunde en technische natuurkunde behaald. In maart 1985 werd aangevangen met het in dit proefschrift beschreven onderzoek. Gedurende de periode van 1 maart tot 1 augustus 1985 is onderzoek verricht bij de positronen groep van het Brookhaven National Laboratory in de VS.